Czech Technical University in Prague
Faculty of Electrical Engineering

Doctoral Thesis

September 2020 **Martin Kněnický**

Czech Technical University in Prague
Faculty of Electrical Engineering
Department of Electrical Power Engineering

IMPACT OF HIGH-FREQUENCY VOLTAGE DISTORTION ON MEDIUM VOLTAGE CABLE SYSTEMS

Doctoral Thesis

Ing. Martin Kněnický

Prague, September 2020

Ph.D. Program: Electrical Engineering and Information Technology (P2612)
Branch of Study: Electric Power Engineering (3907V001)

Supervisor: doc. Ing. Radek Procházka, Ph.D.

I declare hereby that this presented thesis is my own work and has not been submitted in any form for another degree or diploma at any university or other institution of tertiary education. The presented doctoral thesis is based on my original research carried out at the Faculty of Electrical Engineering, Czech Technical University in Prague. All information derived from the published or unpublished works of own or others has been acknowledged in the text and has been given in the list of references or in the list of author's publications.

Prague, 30th September 2020 Martin Kněnický

In Czech:

Tímto prohlašuji, že tato dizertační práce je mojí vlastní prací a nebyla předložena v této ani žádné jiné formě za účelem získání titulu nebo diplomu na žádné univerzitě nebo instituci terciárního vzdělávání. Předložená dizertační práce vychází z mého vlastního výzkumu prováděného na Fakultě elektrotechnické Českého vysokého učení technického v Praze. Veškeré informace získané z cizích a vlastních publikovaných i nepublikovaných pramenů jsou v textu odkazovány na tyto prameny a jsou uvedeny v seznamu použité literatury nebo v seznamu autorových publikací.

V Praze, 30. září 2020 Martin Kněnický

ACKNOWLEDGMENT

I would like to express my gratitude to my supervisor and mentor Radek Prochazka for his guidance during the entire studies, many valuable advice, inspiring impulses, and factual suggestions. I am also glad that here I can thank my colleagues from the High Voltage Laboratory Jan Hlavacek and Ondrej Sefl for many fruitful discussions, language correction of these texts, and their help with complicated measurements. Thanks also go to other staff of the Department of Electrical Power Engineering for ensuring a supportive and flexible environment for my research. I am also deeply grateful to my wife Marie and the whole family for their support, encouragement, and patience during my whole studies. Last but not least, I am much obliged to everyone who supported me throughout this venture of my doctoral research.

The research has been partially supported by the Grant Agency of the Czech Technical University in Prague with projects No. SGS16/153/OHK3/2T/13, SGS18/133/OHK3/2T/13, SGS20/124/OHK3/2T/13.

Thanks to all of you!

In Czech:

PODĚKOVÁNÍ

Tímto bych rád vyjádřil své poděkování mému školiteli a mentorovi Radkovi Procházkovi za jeho vedení během celého studia, mnoho cenných rad, inspirujících podnětů a věcných připomínek. Také bych zde rád poděkoval kolegům z Laboratoře vysokých napětí Janu Hlaváčkovi a Ondřeji Šeflovi za mnoho podnětných diskuzí, jazykovou korekci této práce a za jejich pomoc během realizace komplikovaných měření. Děkuji také všem ostatním z kolektivu Katedry elektroenergetiky za vytvoření podporujícího prostředí pro realizaci mého výzkumu. Obrovské poděkování patří také mé manželce Marii a celé rodině za jejich neutuchající podporu, stálé povzbuzování a velkou trpělivost během mého celého studia. Nakonec, ale neméně, bych rád poděkoval i všem ostatním, kteří mi během mých výzkumů jakkoli pomohli.

Tento doktorský výzkum byl částečně podpořen projekty Studentské grantové soutěže ČVUT v Praze: SGS16/153/OHK3/2T/13, SGS18/133/OHK3/2T/13,SGS20/124/OHK3/2T/13.

Děkuji Vám všem!

ABSTRACT

The thesis addresses the impacts of high-frequency voltage distortions in power systems on the insulation of medium voltage cable systems. Originating from the switching processes of the ever-expanding power electronic devices, high-frequency components in the range of several kilohertz are superimposed on power frequency sinusoidal voltage and may cause a new type of continuous overvoltage in present power systems. The main aim of this thesis is to evaluate the extent of the influence of such real voltage distortions on complex medium voltage cable systems. Currently published researches on this topic have been focused mostly on the investigations of material samples and not on complex insulation systems. This thesis thus strives to present a complex investigation of the discussed issue.

At first, an extensive summary of the occurrence of high-frequency voltage distortion in power systems is stated. The detailed overview of degradation and aging processes in polymeric insulation materials under high-frequency and combined voltage stresses follows. The first part of the investigation is focused on determining the real shape of high-frequency voltage distortion, which may occur in actual power systems. Since large photovoltaic power plants are typical installations of large power electronic devices, the numerical simulation of one such installation has been created. Further, a specialized test site, which was constructed for long-term accelerated aging of medium voltage insulation systems, is described. The realized test circuit was able to generate continuous combined power frequency and high-frequency voltage stresses with concurrent elevated thermal stress. Finally, the experiment, which was designed to determine the effect of high-frequency distortion phenomenon, is presented. For the experimental purposes, samples of actual cable systems were prepared from a commercial medium voltage cable with cross-linked polyethylene (XLPE) insulation. Different cable samples were assembled by pairs of the same cable terminations of two different types. One group of cable samples was subjected to accelerated aging tests with high-frequency voltage distortion. Another group of cable samples was exposed to the same aging tests, but without high-frequency components. Diagnostic and monitoring measurements (partial discharges, dissipation factor, breakdown voltage tests, X-Ray scanning) were carried out during and after the aging tests to evaluate the condition of insulations. Subsequently, the individual results were compared and discussed in terms of the effect of high frequency-voltage distortion on the aging rate of medium voltage cable systems.

Keywords:

Accelerated aging; cable insulation; cable termination; combined stress; harmonic distortion; high-frequency harmonics; high-frequency impulses; insulation measurement; insulation testing; medium voltage; nonstandard voltage stress; photovoltaic system; power grid; power system; resonance impulses; supraharmonics.

In Czech:

ABSTRAKT

Dizertační práce se zabývá dopady vysokofrekvenčních zkreslení v elektrických sítích na izolaci vysokonapěťových kabelových souborů. Harmonická zkreslení v řádech několika kilohertz pochází ze spínacích procesů stále se častěji vyskytujících zařízení s výkonovou elektronikou. Tato zkreslení jsou superponována na síťové sinusové napětí, čímž mohou vytvářet nový typ trvalého přepětí v distribučních sítích. Hlavním cílem této práce je zhodnotit rozsah vlivu takovýchto napěťových zkreslení na reálné a poměrně složité izolační systémy vysokonapěťových kabelových souborů. Dosud publikované výzkumy byly převážně zaměřeny na zkoumání samotných izolačních materiálů a nikoli na komplexní izolační systémy. Tato práce poskytuje ucelený pohled na danou problematiku.

Na úvod je v práci popsán princip vzniku a rozsah výskytu vysokofrekvenčních zkreslení v energetických systémech. Následuje podrobný přehled a popis degradačních procesů a stárnutí polymerních materiálů při vysokofrekvenčním a kombinovaném napěťovém namáhání. První část vlastního výzkumu je zaměřena na zjištění skutečného tvaru vysokofrekvenčního zkreslení, které se může objevit v reálných distribučních sítích. Za tímto účelem byla vytvořena numerická simulace instalace velké fotovoltaické elektrárny v distribuční síti, která je typickým příkladem použití výkonové elektroniky větších výkonů. Dále je popsáno speciální testovací pracoviště, které bylo vybudováno za účelem realizace dlouhodobého stárnutí vysokonapěťových izolačních systémů. Testovací obvod umožňuje generovat kontinuální napěťové namáhání s možnou superpozicí vysokofrekvenčních komponent a současně zvýšené tepelné namáhání. Na závěr je prezentována experimentální část výzkumu, která zjišťuje dopady vysokofrekvenčního zkreslení napětí na izolační systémy. Pro tyto potřeby byly z komerčně dostupného vysokonapěťového kabelu s izolací ze zesítěného polyetylenu (XLPE) připraveny vzorky reálných kabelových souborů. Každý vzorek kabelu měl namontované dvě kabelové koncovky stejného typu, přičemž bylo vybíráno ze dvou různých typů koncovek. Jedna skupina vzorků byla poté vystavena zrychlenému stárnutí za přítomnosti vysokofrekvenčního zkreslení. Druhá skupina vzorků byla podrobena stejnému stárnutí, avšak jen při sinusovém napěťovém namáhání. Všechny vzorky kabelových souborů byly před a během procesu zrychleného stárnutí měřeny a diagnostikovány za účelem zhodnocení stavu izolace (měření částečných výbojů, měření ztrátového činitele, měření průrazného napětí, rentgenové skenování). Poté byly výsledky jednotlivých měření mezi sebou porovnány a diskutovány s cílem vyjádřit míru vlivu vysokofrekvenčního zkreslení napětí na rychlost stárnutí vysokonapěťových kabelových souborů.

Klíčová slova:

Distribuce elektrické energie; fotovoltaická elektrárna; kabelová koncovka; kombinované namáhání; měření izolačních materiálů; nestandardní napěťové namáhání; rezonanční impulzy; supraharmonické; testování izolace; vysoké napětí; vysokofrekvenční zkreslení; vysokonapěťový kabel; vyšší harmonické; zrychlené stárnutí.

CONTENT

LIST OF ABBREVIATIONS

ANOVA	Analysis of Variance
ASD	Adjustable Speed Driver
CT	Current Transformer
EPR	Ethylene-Propylene Rubber
FACTS	Flexible AC Transmission System
GTO	Gate Turn-off Thyristor
HVDC	High Voltage DC Transmission
IGBT	Insulated Gate Bipolar Transistor
IGCT	Integrated Gate Commutated Thyristor
LDPE	Low-Density Polyethylene
MEP	Main Effect Plot
MOSFET	Metal Oxide Semiconductor Field Effect Transistor
PCC	Point of Common Coupling
PD	Partial Discharge
PDEV	Partial Discharge Extinction Voltage
PDIV	Partial Discharge Inception Voltage
PE	Polyethylene
PET	Polyethylene Terephthalate
PP	Polypropylene
PV	Photovoltaic
PWM	Pulse Width Modulation
SiC	Silicon Carbide
SPC	Standardized Pareto Chart
STATCOM	Static Synchronous Compensator
THD	Total Harmonic Distortion
VSC	Voltage Source Converter
VT	Voltage Transformer
XLPE	Cross-Linked Polyethylene
ZnO	Zinc Oxide

1. INTRODUCTION

Undisputedly, the entry of power electronics into power grid systems has caused a revolution. The first power electronic devices for medium and high voltage power applications were mercury-arc rectifiers, which were mainly used to convert energy from ac distribution networks to dc traction systems. It was a revolutionary step from mechanical rotary converters to cheaper solid-state electronic devices that happened nearly 100 years ago. Another milestone in power systems was the replacement of original arc-electronic devices with semiconductor electronic devices in the 1970s. Since then, these power electronic devices have been significantly developed and greatly expanded in many power applications. In present electrical systems, various power conversions (ac-dc, dc-ac, ac-ac, and dc-dc) are performed by semiconductor switching devices such as diodes, thyristors, and power transistors. Various semiconductor-based power installations have flooded power grids; examples include inverters in photovoltaic and wind power plants, controlled power flow converters, flexible ac transmission systems (FACTS), adjustable speed drivers (ASD), traction power rectifiers, converters in high voltage dc transmissions (HVDC), static synchronous compensators (STATCOM), etc. Unfortunately, the use of power electronics in ac systems has the fundamental consequence of distorting the originally sinusoidal current and voltage waveforms.

Current and voltage distortions, which are caused by switching of power electronics, are monitored and covered by power quality management to a limited extent. Many filters are usually installed to reduce the distortions to the prescribed limits that are given by many technical standards for power quality of power distribution systems as well as for power electronics equipment itself. The reasons for the use of filters are the adverse effects of superimposed higher harmonics on many technical and economic aspects of power generation and distribution, including higher power losses during power transmissions, higher reactive power flows, higher costs of new equipment, etc. The main technical standards in this area, such as EN 50160 [1], IEC 61000 series (especially IEC TR 61000-3-6 [2]), or IEEE Std. 519 [3], solve harmonic distortions up to a maximum of 50^{th} harmonic order (i.e., frequency of 2.5 kHz in 50 Hz power systems or 3 kHz in 60 Hz power systems), which is sufficient to cover almost all related problems. However, one serious problem remains for much higher frequency distortion as well. Superimposed voltage distortions in power systems cause continuous repetitive overvoltages, which may increasingly stress insulation systems.

Since many harmonic distortions are active in higher frequency spectrums (over 50^{th} harmonic order), they are not part of quality management analysis and therefore are not usually filtered. Combinations of large capacitive components, such as medium voltage cables

or large capacitors, typical inductive components, such as windings of power transformers or large motors, and power electronics represent the problematic parts of power distribution systems. Emitted impulses from switching of power electronics and impedance resonances of the power system may cause significant high-frequency voltage resonances, which may have a significant impact on medium voltage insulation systems. Currently, the occurrence of unexpected failures has already been observed in medium voltage cable terminations, transformer windings, and windings of large motors and generators.

The first harmful effects of low-frequency harmonic distortion were noticed as early as 1950 by S. B. Warder et al. in [4]. A 33-kV cable with oil-impregnated paper insulation connected the ac grid and the mercury-arc rectifiers that supplied the London underground transport system. An unexpectedly high failure rate was observed in the cable system. The authors found a clear correlation between cable failures and harmonic distortion and eliminated other possible causes such as occasional high overvoltage transients. Since then, harmonic voltage distortions have raised a growing interest in accelerated aging studies of insulation systems (some of them are mentioned in the thesis below).

Contemporary cables are made from high-quality polymeric insulation material like ethylene-propylene rubber (EPR) or cross-linked polyethylene (XLPE) that are usually very resistant to many adverse environmental and operating conditions. The electric field distribution in medium voltage cables is uniform as well. However, each cable system includes cable terminations and sometimes joints. These components have complex structures comprised of many different materials that typically create non-uniform electric field distributions. This fact and practical experience show that cable terminations are usually the riskiest parts of medium voltage cable systems, as was also confirmed by K. Uchida et al. in [5].

Many contemporary research groups are concerning more and more with this issue as more power electronic devices are being installed in power systems. Although the impacts of standard harmonics on insulation systems were recognized a long time ago, the effects of high-frequency voltage distortions, which reach higher dV/dt ratios and significant amplitudes, are not fully understood yet.

1.1. Objectives of Doctoral Thesis

The main aim of this thesis is to evaluate the extent and severity of the influence of realistic high-frequency voltage distortions on complex medium voltage cable systems. This phenomenon has only been investigated on samples of pure insulation materials yet, however, studies on samples of whole real complex insulation systems are still lacking. The goals set by this doctoral thesis aim to prove the effect of this phenomenon and therefore to confirm the assumptions presented in the review of published research mentioned in following chapter 2.

The main objective of this work can be divided into the following partial goals:

- To determine shape of voltage waveforms in power systems which contains power electronic components. This would be done by numerical simulations of part of electric network connected to a large photovoltaic power plant.
- To design and realize a specialized test site for accelerated electrical and thermal aging of medium voltage insulation systems. The proposed test site would also include automatic acquisition of fundamental diagnostic data.
- To perform comprehensive experimental aging tests on sets of cable samples equipped with terminations. The parameters of the aging tests would be based on the results obtained by the realized numerical simulations.
- To monitor and evaluate the condition of the tested samples during and after the aging process by suitable diagnostic methods. The gathered results would create the basis for the subsequent assessment of the effect of high-frequency oscillations on the aging rate of the respective insulation systems.

Fulfillment of these goals should provide the answer whether the high-frequency voltage distortions play a significant role in the aging processes of high voltage insulation systems.

1.2. Structure of Doctoral Thesis

The thesis consists of eight chapters, including "Introduction".

The second chapter, "Cable Systems and High-Frequency Voltage Distortions in Power Grids," describes the current state of the investigated issue and provides a theoretical background for the following works. The chapter begins with a description of structures of medium voltage cables and cable terminations. Further, the occurrence of high-frequency distortions in power systems is discussed. Then follows an overview of degradation mechanisms of cable insulation systems under high-frequency voltage distortions. At the end of the chapter, an overview of existing studies on the aging of polymeric insulations under nonsinusoidal voltage waveform is mentioned. The summaries presented in this chapter form the hypotheses, which are examined in the experimental part of the work.

The third chapter, "Verification of High-Frequency Voltage Distortion in Power Grid using Numerical Model," contains the description and results of the numerical simulation that is focused on a real part of the power grid with a large photovoltaic power plant. The structure of the model was designed with respect to the high-frequency behavior of all simulated components. The simulation has been assembled in Matlab Simulink software.

The fourth chapter, "Testing System for Combined Stresses of Medium Voltage Insulations," deals with the design and construction of a specialized test circuit, which enables accelerated multi-stress aging of medium voltage insulation systems. Parameters and structure of individual devices are discussed. The whole test system was built in the High Voltage Laboratory of the Faculty of Electrical Engineering, Czech Technical University in Prague.

The fifth chapter, "Experimental Procedures for Accelerated Aging Tests of Medium Voltage Cable Systems," is focused on the description of the experimental test setup. The determination of voltage amplitude, magnitude of superimposed voltage distortion, and size of the current load, which causes thermal stress, is explained here.

The sixth chapter, "Results of Accelerated Aging Tests of Medium Voltage Cable Systems," discusses the results from individual diagnostic and monitoring measurements that were carried out on cable system samples during and after the aging test. Procedures of used diagnostic methods are described and explained as well. These methods include measurements of dissipation factor, partial discharge measurements, final breakdown voltage tests, and X-ray scanning of cable terminations after breakdowns.

The seventh chapter, "Discussion," describes the results of experiments and discusses the outputs of partial investigations.

The eighth chapter, "Conclusion," summarizes the research results and relates them to the objectives that have been set out in the Introduction.

2. HIGH-FREQUENCY VOLTAGE DISTORTIONS AND CABLE SYSTEMS IN POWER GRIDS

2.1. High-Frequency Voltage Distortions in Power Grids

The fundamentals of controls of modern power motors are adjustable speed drives (ASD) with voltage source converters (VSCs). Another major use of VSCs is in power flow management of electrical systems and in distributed power resources (e.g., wind power plants, photovoltaic power plants). VSCs are usually based on the use of controlled semiconductors (GTO, MOSFET, IGCT, IGBT, etc. controlled by pulse width modulation - PWM). Principles of many of these power electronic components and systems are described by Bin Wu in [6].

The use of power electronics may cause numerous distortions in electrical networks. Distortions (mainly harmonics) up to 40^{th} or 50^{th} order of the fundamental harmonic are usually well filtered according to many technical standards, such as EN 50160 [1], IEC 61000-3 series (especially IEC TR 61000-3-6 [2]), or IEEE Std. 519-2014 [3]. However, the situation for higher harmonics is quite different. A review by S. K. Rönnberg et al. in [7] describes and summarizes the presence of non-negligible distortions in electrical power systems in the frequency range of 2 kHz – 150 kHz. The overview provides an extensive description of the issue but does not distinguish between low and high voltage levels.

Some studies [7]-[9] introduce new concepts of distortions in power grids – internal, primary, and secondary harmonic emissions. Each device has its internal emissions. This emission is generated in the device itself. If a device is connected to an electrical network, the internal emission of the device and passive parameters of the power system produces primary harmonic emission. The primary harmonic emission is usually not the same as the emission measured by standardized tests. The reason is its dependence on time (operating mode) and location, which determines the passive parameters of the network. Secondary harmonic emission is distortion generated by sources outside of the devices (by other devices connected to the power system). The resulting distortion is given by the interaction of primary emission, secondary emission, and non-linear phenomena in the power grid (non-linear loads, grid impedances changes with terminal voltage, transient processes, etc.). Any predictions of shape,

value, and frequency content of final distortions at different positions of varyingly complex power distribution systems are very complicated, if not impossible.

High-frequency components above 2 kHz in distribution power grids have many names in various literature. They are usually collectively called as high-frequency distortions, high-frequency oscillations, high-frequency resonances, or newly supraharmonics. Examples of such voltage distortions in electrical power systems are given in the following subchapters.

2.1.1. Systems with Controlled Large Power Motors

An example of a circuit with a motor controlled by ASD is shown in Fig. 1. On one side, the ac voltage is rectified by power diodes. On the other side, the ac voltage with different variable parameters is generated by switching of dc voltage using a semiconductor inverter. A significant voltage distortion was detected in the low voltage distribution systems with motors controlled by ASDs. Some practical measurements are shown in Fig. 2. The first record shows the three-phase voltage at the point of common coupling (PCC) in a steel bar cutting application. The other record shows the voltage at the PCC of an oil platform. Both measurements show significant distortions with fast voltage changes and even with multiple

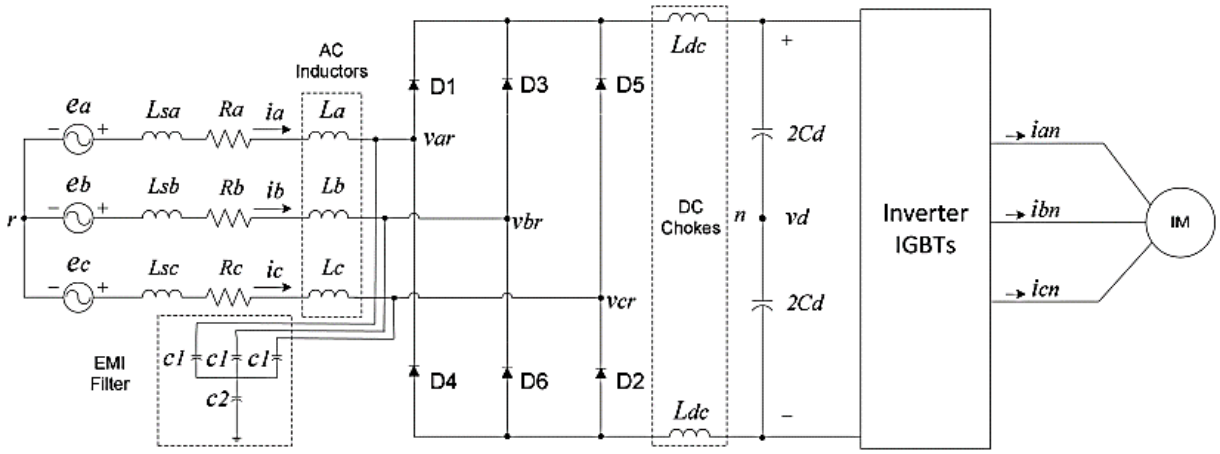

Fig. 1 Example of typical circuit schematic diagram of an ac ASD with the EMI filter, ac input inductors, and dc chokes (Reproduced from [10])

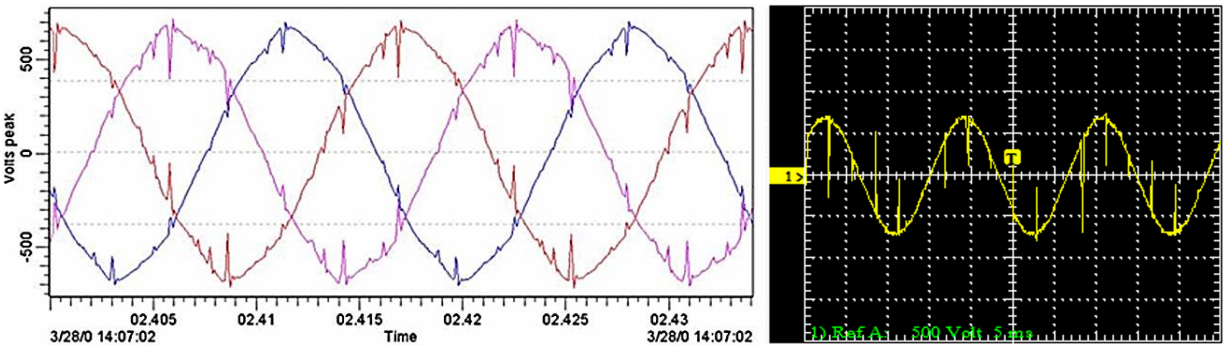

Fig. 2 ***On the left:*** *The three-phase voltage at the PCC in the steel bar cutting application using the ASD;* ***On the right:*** *Voltage at the PCC in the oil platform using the ASD shows significant notching and multiple zero crossings (Reproduced from [10])*

zero crossings. Problems and simulations of voltage distortions in low voltage distribution systems with ASDs and motors were described by K. Lee et al. in [10]. Similar voltage distortion can be expected in a medium voltage power system with large power motors and ASDs.

Multiple transformers with cascade H-bridge connection of VSCs are commonly used for controls of large power motors and power quality in power grids at medium voltage level. The typical topology of the multilevel H-bridge connection of VSCs is shown in Fig. 3. The primary winding of the multiple transformer is supplied from a power grid of 11.5 kV, and the secondary winding consists of fifteen three-phase output sections. Each transformer output supplies one power cell with VSC generating a phase supply of power output. Voltage distortion problems caused by the operation of power electronics are transferred and multiplied by them into medium voltage distribution power systems. Performed measurements and simulations by F. Endrejat and P. Pillay in [11] show significant resonances at frequencies between 4 and 10 kHz depending on various operating conditions. For example, the frequency analysis (by FFT) of simulated and measured voltage at motor terminals (at source bus) for the controlled output frequency of 40 Hz is shown in Fig. 4. In the graph, detected amplified resonance at 4.2 kHz is compared with the emitted distortion of the used inverter as well.

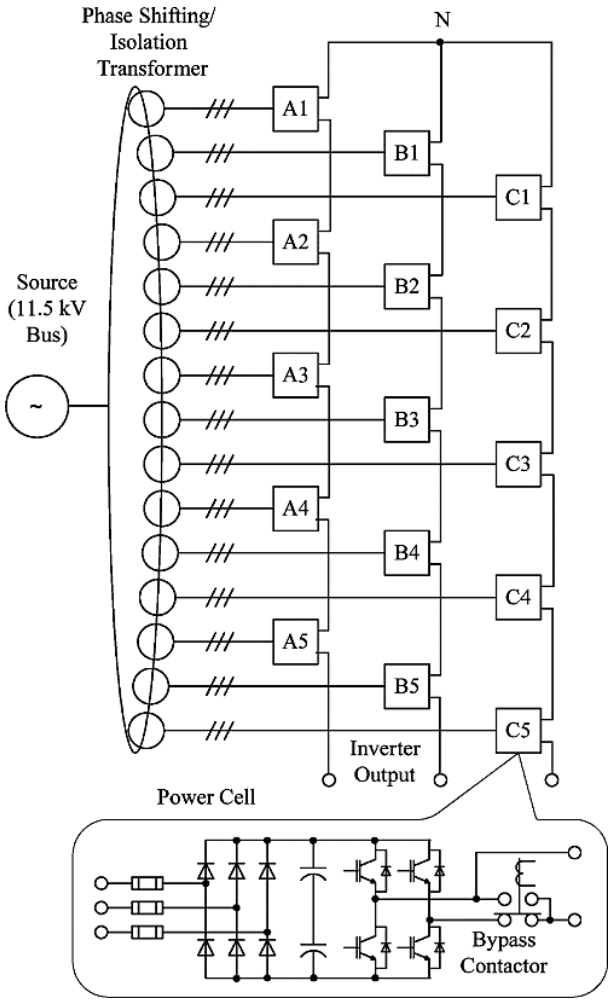

Fig. 3 Example of a typical topology of the multilevel H-bridge connection of VSCs with the multiple transformer to obtain a controlled output voltage of up to 11.5 kV (Reproduced from [11])

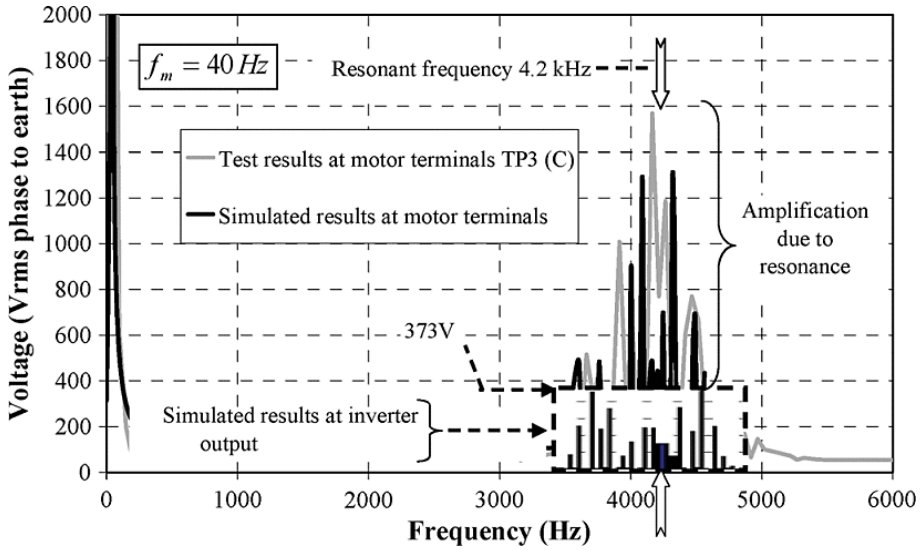

Fig. 4 Frequency analysis (by FFT) of simulated and measured voltage at motor terminals (at source bus) for the controlled output frequency of 40 Hz (Reproduced from [11])

Serious problems with medium voltage fan motors were detected in underground mines by J. Rodriguez et al. [12]. The power supply topology was composed of power transformer, VSCs in multilevel H-bridge connection, and harmonic filter. Measurements and numerical simulations were carried out on motor terminals to explain the detected overvoltages. Examples of measurements with significant high-frequency overvoltages are shown in Fig. 5.

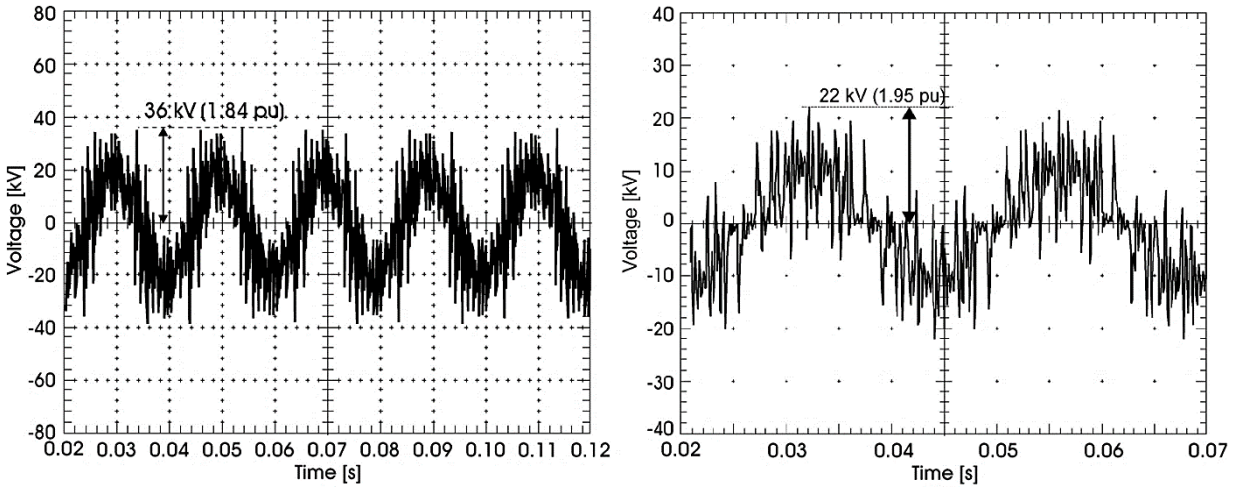

Fig. 5 Measurements on the 13.8-kV motor terminals; ***On the left:*** *Line voltage without the control of frequency - 50 Hz;* ***On the right:*** *Phase voltage with the control of frequency – 38 Hz (Reproduced from [12])*

The fundamental frequency of motors was 50 Hz, and the switching frequency of PWM was 1 kHz. The frequency of a voltage distortion was determined to be around 9 kHz. This is about three times larger than the detected major harmonic produced by PWM in the power system. The impact of various system components and their electrical parameters on the resonance formation was studied as well.

2.1.2. Systems with Control of Power Flows

One of the first studies on the issue of high-frequency voltage distortions in distribution power grids was published by L. Paulsson et al. In the study [13], the authors were dealing with failures of medium voltage cable terminations, which repeatedly took place at the substation in Eagle Pass, Texas, USA, at the connection between the U.S. and Mexican power grids by Back-to-Back tie. The Back-to-Back connection of VSCs with controlled IGBTs by PWM is the new technology for providing the reliable interconnection of two asynchronous ac power systems. The Back-to-Back installation provides power transfer between the two power systems via dc connection in both directions. The Back-to-Back system allows the control of magnitude, phase angle, and frequency of voltage on both sides independently and thus provides needed reactive power support for dynamic voltage control at both interconnected power systems. The specific Eagle Pass back-to-back installation is shown in Fig. 6.

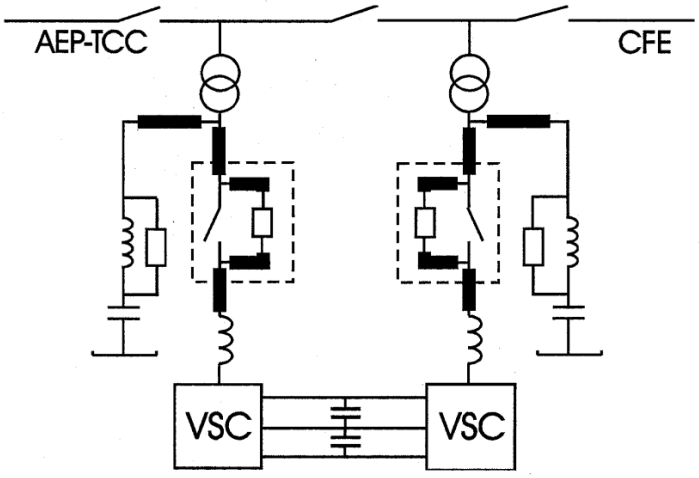

Fig. 6 Schema of the Eagle Pass back-to-back installation for the power quality control and the transmission between U.S. (AEP-TTC) and Mexican (CFE) power grids; The single line diagram shows voltage source convectors (VSC), dc capacitors, phase reactors, harmonic filters, step-up transformers (138 kV / 24 kV), line breakers and medium voltage cables (black rectangles) (Reproduced from [13])

Voltage measurements were taken between medium voltage cable conductor and wire shield on the CFE side transformer for two states of the power system. The first state was when the AEP-TCC side was blocked and disconnected. The other state was when CFE and AEP-TCC sides were in back-to-back operation mode. Voltage waveforms and harmonic spectrums of measurements are shown in Fig. 7. The dominant harmonics are 21st (1.26 kHz, IGBT switching frequency) and 3rd (180 Hz) for the blocked operation. The dominant harmonics for the back-to-back mode are also 3rd and 21st, but there are significant 207th (12.4 kHz) and 63rd (3.78 kHz, three times the switching frequency) harmonics as well. The unexpected 12.4-kHz harmonic had variable amplitude between 13 % and 40 % of the power frequency voltage depending on the operating mode of the back-to-back installation and the angle difference between AEP-TTC and CFE. Amplitudes of other significant harmonics are roughly constant for different operation modes. These results indicate that the IGBT switching causes undesirable high-frequency resonances. Resonances are determined by the circuit reactance,

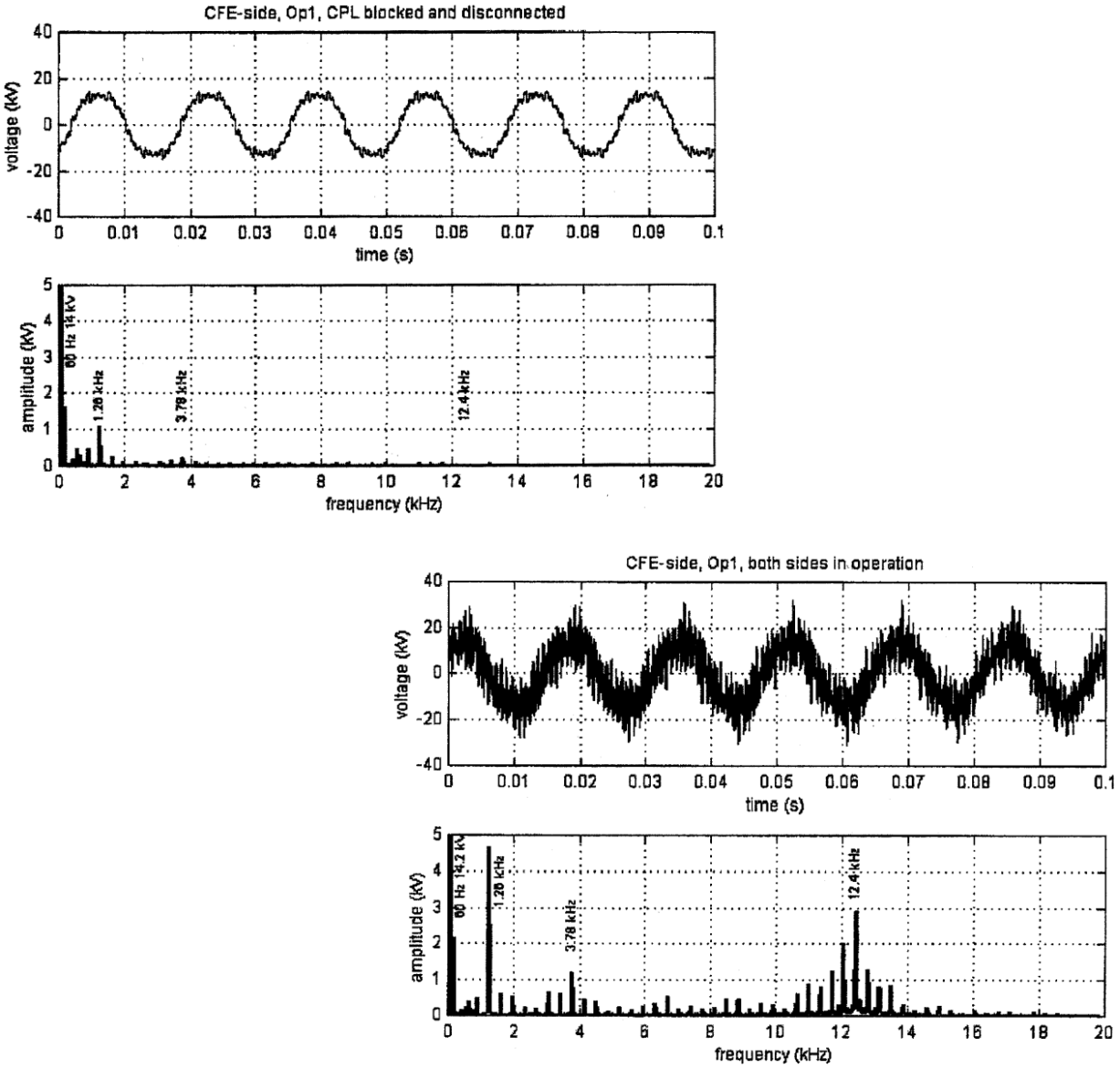

Fig. 7 Measured phase voltage (top) and harmonic spectrums as an average over 1 min (bottom) of the medium voltage CFE side; ***On the left:*** *The AEP-TCC side is blocked and disconnected;* ***On the right:*** *AEP-TCC and CFE sides are in the back-to-back operation (Reproduced from [13])*

the cable capacitance, the stray capacitance, and the transformer winding inductance. The impacts of this real operation on an insulation system were subsequently discussed by T. Bengtsson et al. in [14].

The emergence of the high-frequency harmonic resonance caused by a VSC was clarified by K. Temma et al. in [15]. The authors have numerically simulated the high-frequency resonance phenomenon between a power grid transformer and a multiple transformer with a VSC connected by a long cable. Field measurement was carried out to verify the high-frequency resonance phenomenon on the static compensator (STATCOM) with a similar configuration as the previous numerical model. The multiple transformer with a 53-MVA VSC was connected to the power grid transformer by the 500-m long cable. Voltage and current measurements were performed for two different operation modes of the STATCOM. The

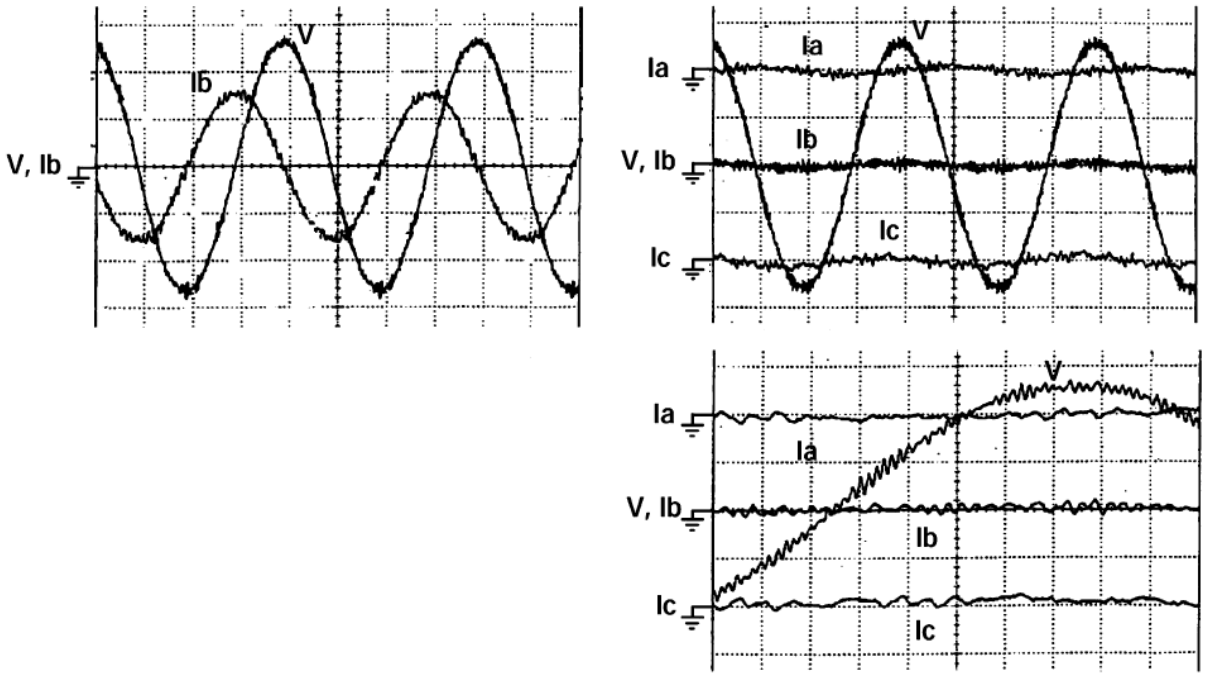

Fig. 8 Measurements of 53 MVA STATCOM (vertical axis: V = 20 kV/div, I = 300A/div; horizontal axis: Time = 5 ms/div, enlarged view Time = 1 ms/div); ***On the left:*** *Phase voltage and current at Q = +37.5 MVAr;* ***On the right:*** *Phase voltage and currents at Q = 0 MVAr (with the enlarged view at the bottom) (Reproduced from [15])*

measurement site was on the primary side of the multiple transformer with VSCs. The high-frequency voltage distortion around 130th harmonic can be determined from measurement results in Fig. 8. These measurement results confirm the exactness of numerical models with series and parallel resonances. The significant dependence of resonance on cable length was detected by the subsequent numerical simulation of the measured power system.

O. Galland et al. in [16] assembled frequency-dependent numerical models of transmission and distribution networks of the Geneva region in Switzerland, which is a combined ac-dc power system. Significant resonance frequencies above 2 kHz were observed in this network analysis. Especially the high resonance amplitude was found at a frequency of 7568 Hz. The "grey-box" power transformer model was compared to the standard inductive power transformer model in models of the distribution network. The capacitive coupling influences the frequency behavior of power transformers for frequencies over 2 kHz. Thus, it cannot be ignored in studies with network simulations. The VSC topology with modular multilevel converters and system filters was also considered in the models of the complex electrical network. Significant impacts of new transmission lines, disconnections of power transformers from the distribution network, and network changes generally were detected for frequency behavior for frequencies over 2 kHz as well. No significant differences were observed in the frequency scan and resonance analysis up to the frequency of 2 kHz. It was shown that system reinforcements could change the resonance node share. Node participation factors directly correlate with resonance frequency and amplitude. Therefore, resonance is affected by network changes due to the size of node participation factors that are close to the expanded area. A high participation factor means significant changes in resonance frequencies

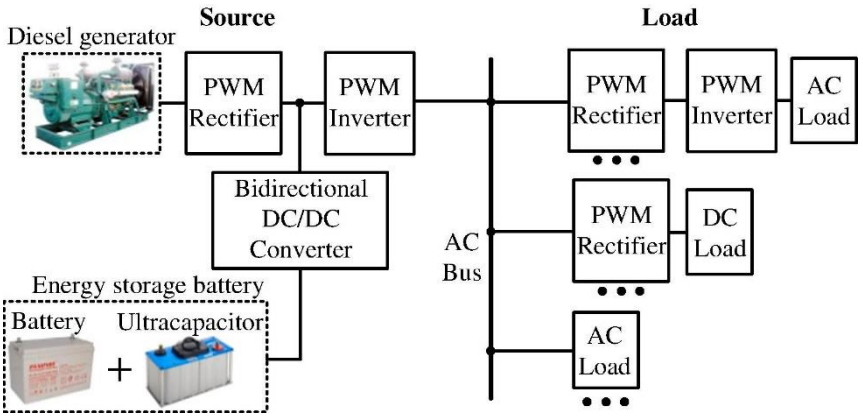

Fig. 9 An example of the structure of an island power system (Reproduced from [17])

and amplitudes, and vice versa, a small participation factor means negligible changes in resonance frequencies and amplitudes.

As is evident from many performed and mentioned studies, the short-circuit power in the place of interest has a significant effect on the occurrence and presence of high-frequency voltage distortions. This means that long branches of transmission and distribution systems and isolated small power systems may be riskier places in terms of this phenomenon. The recent research by W. Wu et al. in [17] focuses on simulation studies of island power systems.

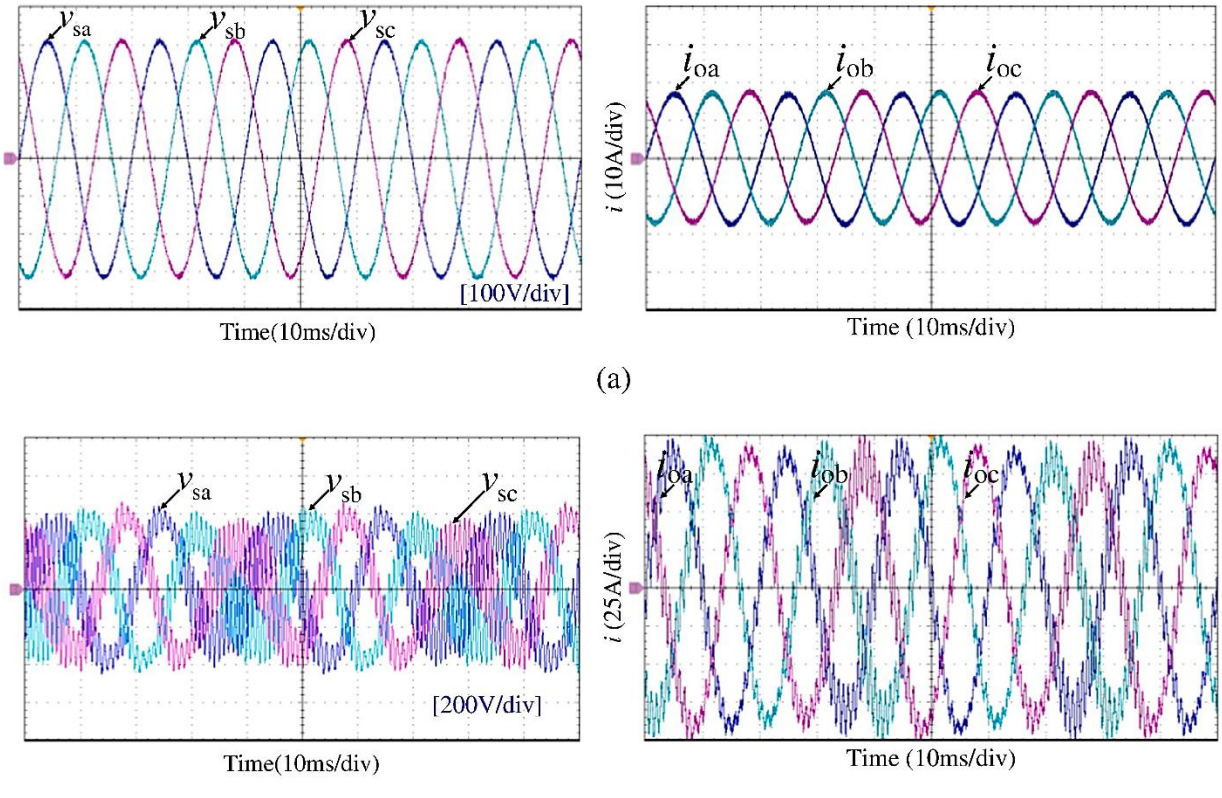

Fig. 10 Some experimental simulation results of the interaction between: a) the source PWM inverter controlled by the conventional dual-loop method and the resistive load; b) the source PWM inverter and the load PWM rectifier both controlled by the conventional dual-loop method (Reproduced from [17])

Typical features of these systems are unconventional power sources such as diesel generators, photovoltaic and wind power plants, etc. These include dc-ac or ac-dc-ac converters controlled by PWM. On the other side, many loads include power electronics as well. Moreover, frequent components in island power systems are energy storage batteries and their individual converters. An example of the structure of an island power system is shown in Fig. 9. The resulting interaction of harmonic emissions from many different power electronic components may cause significant high-frequency resonance oscillations. The resulting interaction is also affected by operation modes of individual power electronic devices, which mainly depends on their power load. Some experimental simulation results of the interaction between the source PWM inverter and the resistive load or the load PWM rectifier controlled by the conventional dual-loop method is shown in Fig. 10. The consequences of the interaction of harmonic emissions from power electronic equipment are evident. When the source PWM inverter is loaded with resistive load, the output voltages and currents are stable. On the other hand, when the load is a PWM rectifier, the output voltages and currents of the source PWM inverter exhibit severe high-frequency oscillation. Similar results were observed for different power loads.

2.1.3. Railway Electrification Systems

Many papers deal with harmonic resonances on high-speed railways, but mostly only up to 50th harmonic order. However, some recent papers describe resonances also for higher frequencies where significant resonances were observed as well [18]-[23]. These papers deal mainly with simulation models, nevertheless with good results in discussions and comparisons with each other. All detailed models describe high-speed traction railways where traction transformers energize the traction power supply system 2 x 25 (27.5) kV from a primary transmission system. Pantograph terminals with locomotive models, which include complex systems of controlled motors with power electronic devices, were also simulated. The point of the issue is the constant change of power system parameters as the train continuously changes its position relative to traction substations. Some results of such simulations are shown in Fig. 11 and Fig. 12.

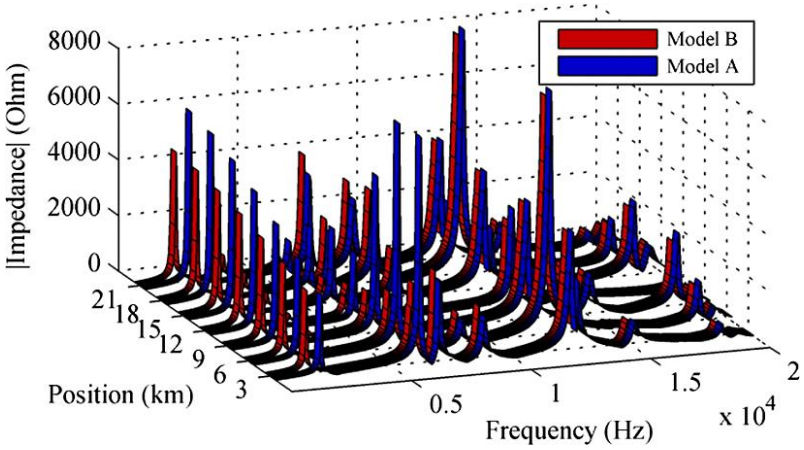

Fig. 11 Frequency response of the traction network impedance at pantograph terminals with two different power system models and in added dependence of the train position (Adapted from [19])

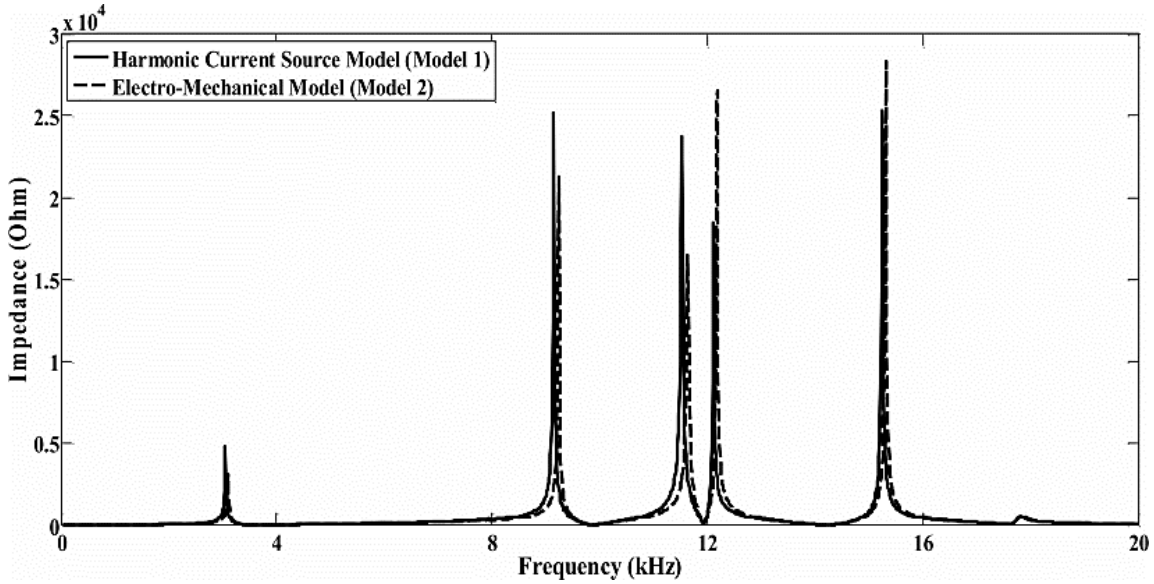

Fig. 12 Frequency response of the traction network impedance at pantograph terminals with two different train models where the train is placed 6 km far from traction substation (Reproduced from [20])

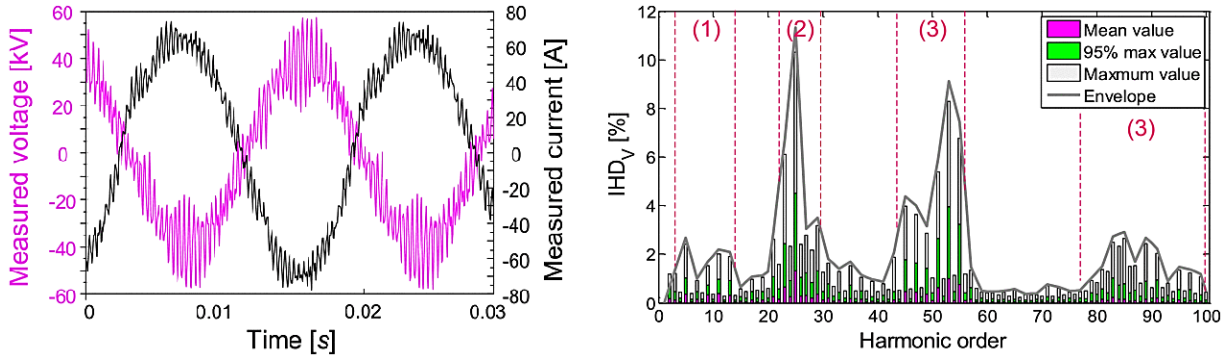

Fig. 13 ***On the left:*** *Measured voltage and current waveforms in traction substation under a resonance condition;* ***On the right:*** *Measured voltage harmonic distortion in traction substation during a 24-h period – (1) low-frequency background harmonics, (2) resonance-region harmonics, and (3) high-frequency characteristic harmonics (Reproduced from [23])*

As is evident from the results of mentioned investigations, frequency analyses greatly depend on the position of pantograph terminal in a railway electrification system. Significant impedance resonances are detected at higher frequencies. Some real measurements also confirm the existence of high-frequency resonance phenomena in railway electrification systems, e.g., in [18] and [23]. The example of real measurements of voltage and current in the high-speed railway electrification system is shown in Fig. 13.

2.1.4. Systems with Wind Power Plants

L. Monjo et al. in [24] describe the occurrence of high-frequency resonances in wind parks. The study focuses on frequency scanning simulations that allow the determination of frequency and peak impedance of parallel resonances. The simulated wind farm consisted of several wind turbines operating at the low voltage level. Each turbine had a harmonics filter and was connected by cable to its own transformer, which increases the voltage to the medium voltage level. All these transformers were interconnected to one medium voltage collector bus by underground medium voltage cables. Further, the medium voltage collector bus was connected through high voltage transformer and high voltage overhead line (or underground cable) to the power grid. A capacitor bank was connected to the medium voltage bus for some simulation cases. The simulated wind power plant is shown in Fig. 14.

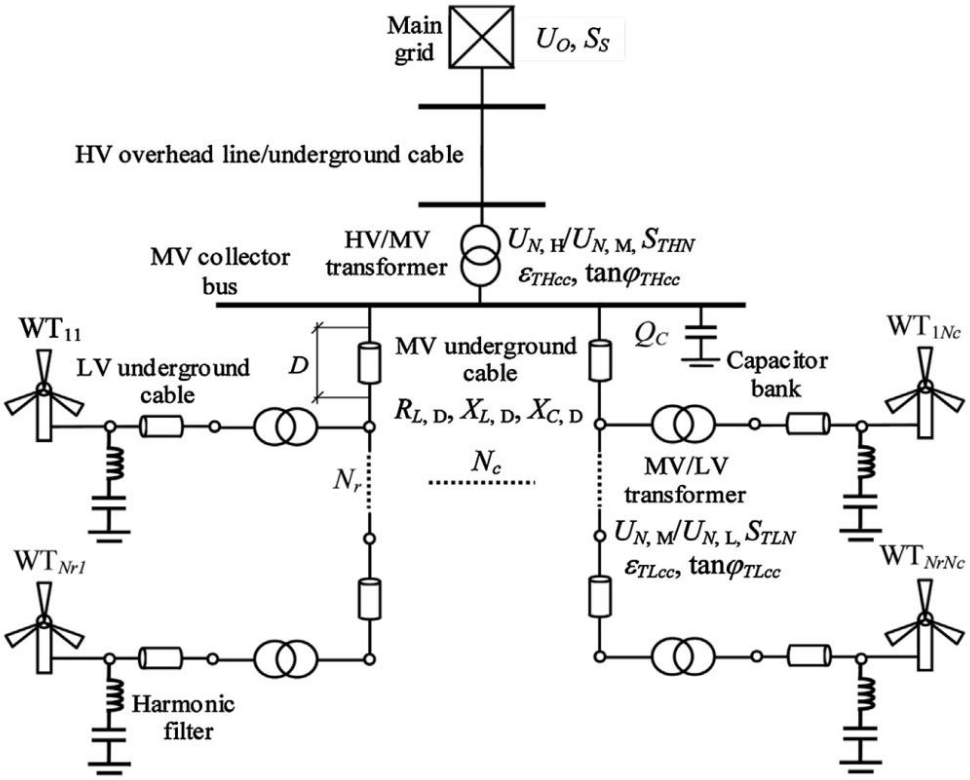

Fig. 14 Diagram of simulated wind power plant (Reproduced from [24])

Many simulation cases were performed with different parameters of the modelled wind park. Some of the simulation results are shown in Fig. 15. Part a) shows the current harmonics emission limit with respect to the VDEW (German Electricity Association) standard. Such current was injected into the model by each wind turbine. Part b) shows three different cases of the model. The case 1 is an initial state. The case 3 examines the situation when all distances are increased by about 1 km (longer cable lengths). The case 4 is the model after the disconnection of the capacitor bank. The strong influence of changes in capacitance on voltage distortions is evident from the simulated model.

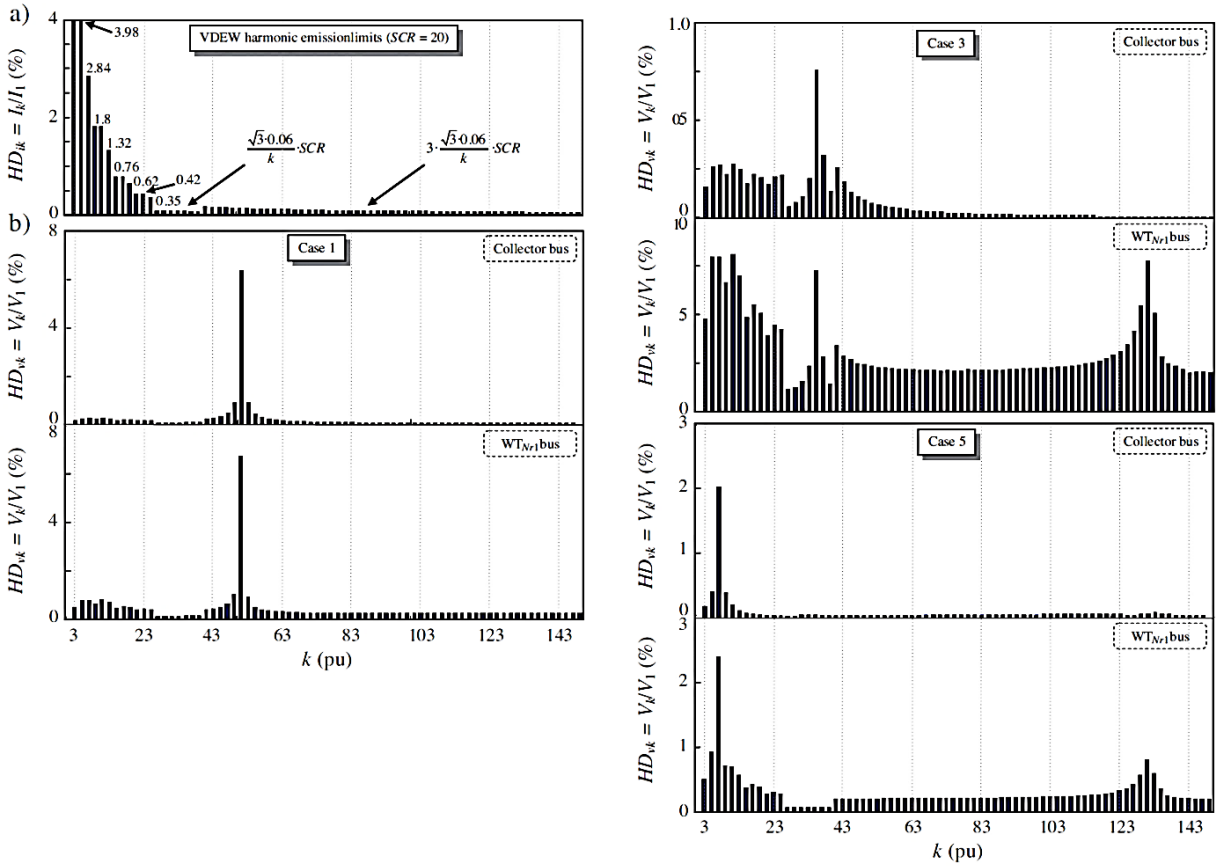

Fig. 15 Simulated harmonic distortions in the wind park: a) current emission limit under German Electricity Association (VDEW) standard from turbines; b) voltage distortions at medium voltage collector bus and wind turbine bus (WT_{Nr1} bus) for three different cases (Reproduced from [24])

The practical investigation by Jim Guo in [25] refers to the issues with the reliability of medium cable terminations in installations with wind farms in U.S. Many terminations suffered premature failures within one year of installation. Strong voltage distortion was detected close to wind turbines and has been identified as the cause of these failures.

2.1.5. Systems with Photovoltaic Power Plants

The possible emergence of high-frequency resonances in low-voltage networks with a large photovoltaic (PV) power plant has been investigated in several recent papers. L. Jessen and F. W. Fusch in [26] studied impedance changes of the distribution network with a connected large PV power plant. They found high resonances at various higher frequencies above 2 kHz for different operating conditions of PV power plant and power system loads. The investigation results were obtained from numerical simulations as well as verification measurements. The more comprehensive and detailed numerical model of the more complex distribution grid with a large power plant was compiled by O. S. Nduka and B. C. Pal in [27]. The simulation results have revealed complex interaction between harmonics produced by a PV power system and the background distortions of the grid. Resonance excitations (both serial and parallel) were observed mainly between 80th and 100th harmonic orders. Real measurements of three different inverters installed in the large Brazilian solar farm were

performed by R. Torquato et al. [28]. The results confirm the emission of dominant high-frequency resonances at a frequency of 16.5 kHz.

Investigation on the penetration of distortion caused by PV resources into power distribution network has also been described by T. Joshi et al. in [29]. The 15-km long three-phase line at a voltage level of 12.47 kV with several transformers connected to a low voltage level of 120 V was selected for the study. The total rated power of this part of the power grid is 10 MVA. The low voltage sections supply a total of about 3300 customers and connect 130 residential rooftop PV systems. The nominal power of each PV residential unit is between 2-4 kW, and the total installed PV power is about 450 kW. Two utility-scale PV power plants of a nominal power of 400 and 700 kW are also installed in this part of the grid. Furthermore, the investigated system includes three capacitor banks that are connected to the medium voltage level in three different locations. Each of these capacitors has a nominal reactive power of 600 kVAr. In the investigated system, the connected PV resources make up approximately 15 % of the total rated power of the feeder. Frequency scans and simulation models were performed for the above-described power system in the frequency range of 2-20 kHz in the main 12.47-kV three-phase bus close to the main substation 69/12.47 kV. Various resonances were detected at frequencies between 3-15 kHz. Some examples of frequency impedance scans are shown in Fig. 16. The significant effect of capacitor banks on the resonance behavior of the power system was observed. Their disconnection reduces by about half the size of resonances in the frequency range of 3-10 kHz.

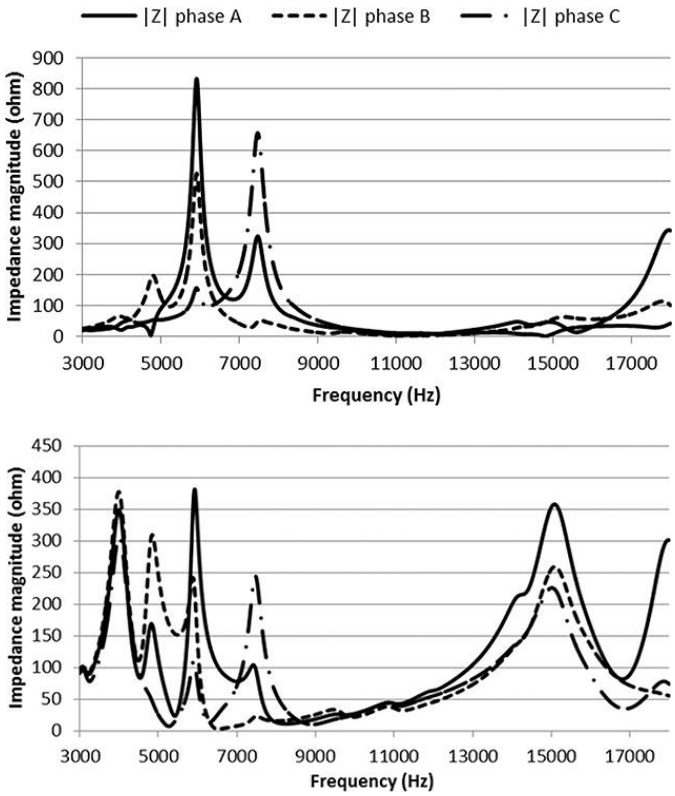

Fig. 16 Frequency response at system main bus (all capacitor banks are switched, power load of the system is 3 MW): ***On the top:*** *three-phase 700-kW utility-scale PV power plant generate positive power;* ***On the bottom:*** *three-phase 700-kW utility-scale PV power plant generate zero power (Reproduced from [29])*

Another reference to the emission of high-frequency distortions into medium voltage systems from a large three-phase power plant is in the CIGRE brochure [30]. The summary of some different studies shows resonant overvoltages at frequencies around 3, 4, 6, 9, and 16 kHz. Distortions in the frequency range of 2-150 kHz are called supraharmonics here.

2.1.6. State of the Art of Voltage Distortions in Power Systems

The papers mentioned above [7]-[30] reveal the existence of high-frequency distortions in medium voltage power systems. The switching of each power electronic device characteristically emits high-frequency distortions that interact with passive parameters of power systems (resistance, capacitance, and inductance), non-linear loads, and emissions produced by the operation of other power electronic devices. The results are often unexpected high-frequency resonances or impulses that are superimposed on power frequency sinusoidal voltage. Such voltage distortions cause continuous overvoltages, which can be a risk for the durability of many different insulation systems.

Published studies show that PWM is the riskiest method of controlling of power electronic components in terms of high-frequency distortions. Another high-risk point is if power system structures, which are usually inductive, contain significant capacitive components, such as medium voltage cables or large capacitor banks. The use of such capacitors is associated with an expansion of renewable energy sources. If emission frequencies of connected devices are close to resonance frequencies of power system impedance, very significant distortion may occur. The frequency content of these distortions is usually between 4 to 16 kHz, and individual magnitudes may range from a few percent to a few tens of percent of the fundamental voltage harmonic.

There are possible ways to reduce these distortions, but since each system is unique, the approach must be individual. Any change in the system, such as reconnecting equipment, connecting new devices, changing loads, changing operation modes of connected equipment, etc., can change high-frequency voltage distortions. Because power distribution systems with many connected components are complex, reliable prediction of resonance phenomena in these systems is very difficult, if not impossible.

Distortions in power systems are usually expressed by the total harmonic distortion (THD) index, which uses only harmonics components of the evaluated signal, not interharmonics [1]-[3]. The voltage distortion is traditionally defined as:

$$THD_{Vn} = \frac{\sqrt{\sum_{h=2}^{n} {V_h}^2}}{V_{1rms}} \cdot 100 \ (\%) \tag{1}$$

where h is the harmonic order (multiple order) of the angular frequency of the reference fundamental voltage (with a temporal frequency of 50 or 60 Hz), n is the maximum considered harmonic order, V_h is the rms voltage of the h-th harmonic order, and V_{1rms} is the rms voltage of the reference fundamental harmonic. According to current standards, e.g. [1]-[3], the values

of THD_{Vn} are conventionally determined for n = 40 or 50, but of course, this is not a limit for this definition. THD for currents can be expressed analogously.

2.2. Structure of Medium Voltage Cable Systems

A contemporary medium voltage cable system consists of a shielded cable usually with cross-linked polyethylene (XLPE) or ethylene-propylene rubber (EPR) insulation, cable terminations, and sometimes cable joints. An example of a 22 kV shielded cable with XLPE insulation, which is commonly used in Europe and was therefore chosen for testing in this doctoral research, is shown in Fig. 17. The technical detail parameters are listed in the product catalog [31]. This cable has semiconducting layers on both sides of the XLPE insulation for the better electric field distribution. The electrical shield (Cu wire screen and counter helix Cu tape) is placed in the semiconducting soft tape to minimize air gaps. The shield is covered by the non-conducting tape to keep water away and the outer polyethylene (PE) sheath. Sometimes the PE sheath may be covered with an added PVC sheath to improve the external mechanical resistance of the cable. V. Vahedy published a summary of structures and materials used in polymeric high voltage cables in [32].

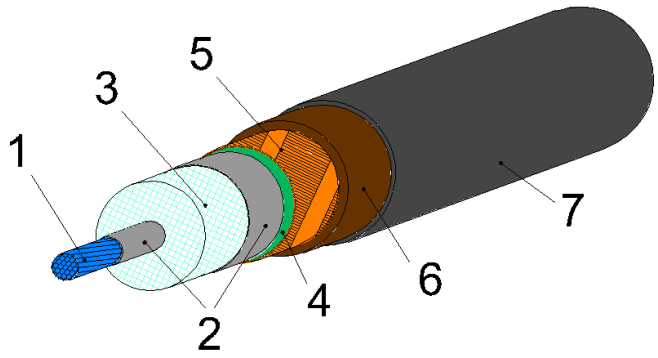

Fig. 17 Medium voltage cable with the XLPE insulation – type 22-AXEKCE: 1 – Aluminum conductor, 2 – Inner and outer semiconducting layer, 3 – XLPE insulation, 4 – Semiconducting tape, 5 – Cu wire screen and counter helix Cu tape, 6 – Non-conducting tape, 7 – Outer PE sheath

Electrical field distribution and the whole construction of a medium voltage cable is very homogenous and invariable in length. The problem with the electrical field distribution is mainly in cable terminations between conductor and screen. Contemporary medium voltage cable terminations are very complicated because the uniform electric field distribution is required [33], [34]. Stress grading methods are used to control the electric field in terminations. These methods can be generally divided into two groups: a geometric stress grading (capacitive stress cone) and a non-geometric stress grading (resistive, refractive, or resistive-refractive). Usually, stress grading materials are composites with the electric field dependent conductivity. Such composites are most commonly zinc oxide (ZnO) or silicon carbide (SiC).

Terminations may also be divided on the base of the installation method. Three basic installation methods are heat-shrink, cold-shrink, and slip-over methods. Each method has its

advantages and disadvantages as quality, price, installation condition, instrument demands, trained workers, etc. Individual producers give specific details.

An example of the most commonly used heat-shrink and slip-over cable terminations with non-geometric stress grading for medium voltage systems are shown in Fig. 18 and Fig. 19. These types were used for laboratory testing in this doctoral thesis.

For both types, a cable lug is installed on the cable conductor, and the outer semiconducting layer is removed from the XLPE insulation to the distance defined by the installation manual. A smaller section of the XLPE insulation remains covered with the outer semiconducting layer near the Cu wire screen. The Cu wire screen outlet is located on the fixed and sealant tape. The infill tape reinforces the discharge resistance of a heat-shrink termination on the interface between the XLPE insulation and the semiconducting layer. The whole termination is covered by the heat-shrink silicone tube with inner ZnO or SiC heat flexible layer (stress grading and sealant layer). The stress control of an elastomeric termination is ensured by self-fusing stress grading sheet located from the half of XLPE insulation over the semiconducting layer to the Cu wire screen. Red sealant tapes cover interfaces between the

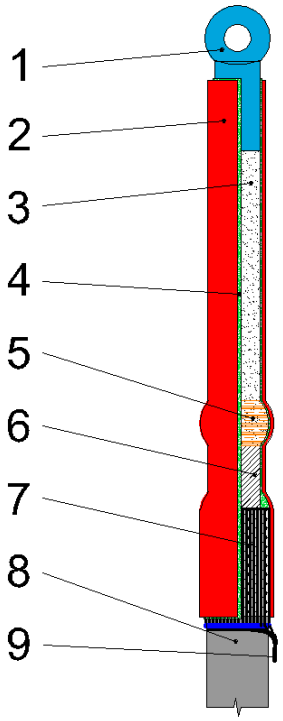

Fig. 18 Heat-shrink cable termination with the non-linear stress grading for 22 kV indoor use: 1 – cable lug, 2 – heat-shrink silicone insulation tube, 3 – XLPE insulation, 4 – stress grading and sealant heath flexible layer (ZnO or SiC), 5 - infill tape, 6 – semiconducting layer, 7 – fixed and sealant tape with Cu wire screen, 8 – medium voltage cable with PE/PVC sheath, 9 – Cu wire screen

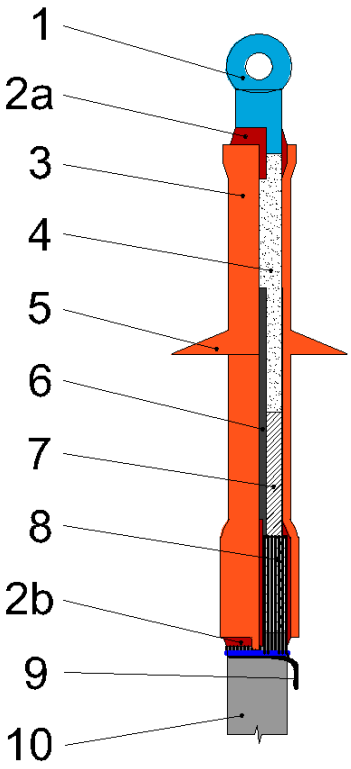

Fig. 19 Elastomeric (slip-over applied) cable termination with the non-linear stress grading for 22 kV indoor use: 1 – cable lug, 2 – red sealant tapes, 3 – silicone rubber insulation tube, 4 – XLPE insulation, 5 – protect silicone shed, 6 – self-fusing stress grading sheet, 7 – semiconducting layer, 8 – fixed and sealant tape with Cu wire screen, 9 – Cu wire screen, 10 – medium voltage cable with PE/PVC sheath

cable lug and the XLPE insulation, and between the electrical stress control slide and the Cu wire screen outlet. The elastic silicone rubber tube is slipped over onto the termination. Both ends of the tube cover red sealant tapes. Detailed structures of cable terminations are mentioned in assembly manuals [35] and [36]. Structure differences between inner and outer cable terminations are dimensions (length) and the number of silicone sheds. The same differences are also between cable terminations for different voltage levels.

2.3. Degradation Mechanisms of Cable Insulation Systems under High-Frequency Voltage Distortions

Numerous research groups have presented many different implications of voltage waveform distortions on various insulation systems. However, only studies related to medium voltage cable systems are discussed below. Some papers aim only on cable insulation itself, others address only problems with cable terminations, and some investigations were conducted with small samples of pure insulation materials. The main results of these works are mentioned and described in the following subsections.

2.3.1. Dissipation Losses in Insulation Materials

The effect of impulse and high-frequency sinusoidal voltages on properties of solid dielectric materials has been widely discussed in some papers, e.g., in [37]-[39]. Generally, change in parameters of insulation materials, such as dissipation factor, capacitance, resistance, temperature, etc., is directly related to change in the shape of the applied voltage waveform.

The dissipation losses, which are defined further, represent the thermal stimulation of a dielectric material under an ac electric field. In general, thermal stimulation is given by the delay of dipole polarization in the dielectric material according to the change in polarity of the electric field. If the delay of the dipole rotation after the voltage reversal is zero, the heat production is also zero. Theoretically, this is possible, but in practice, there is always a slight delay in the rotation of dipoles according to the polarization effect. This phenomenon intensifies with the increasing frequency of the electric field. The polarization ability of dipoles in a dielectric material under ac voltage is represented by its permittivity. The complex frequency-dependent permittivity ε^* of an insulation material under ac voltage is given by the formula:

$$\varepsilon^* = \varepsilon'(\omega) - j \cdot \varepsilon''(\omega) \tag{2}$$

where ε' is the frequency-dependent real component of permittivity, ε'' is the frequency-dependent imaginary component of permittivity, and $\omega = 2 \cdot \pi \cdot f$ is the angular frequency at frequency f. Should any repetitive voltage at a repetition rate R be applied, the overall voltage can be expressed as:

$$v(t) = a_0 + \sum_{n=1}^{\infty} a_n \cdot cos(2\pi R \cdot n \cdot t) + \sum_{n=1}^{\infty} b_n \cdot sin(2\pi R \cdot n \cdot t) \quad (3)$$

where a_o, a_n, and b_n are coefficients of the Fourier series expansion of the voltage $v(t)$. The leakage current of insulation material can be expressed as:

$$i(t) = G \cdot \left\{ \begin{array}{l} \sum_{n=1}^{\infty} -a_n \cdot \varepsilon_n^* \cdot 2\pi R \cdot n \cdot sin(2\pi R \cdot n \cdot t + \delta_n) + \\ \sum_{n=1}^{\infty} b_n \cdot \varepsilon_n^* \cdot 2\pi R \cdot n \cdot cos(2\pi R \cdot n \cdot t + \delta_n) \end{array} \right\} \quad (4)$$

where G is the geometric constant (in the case of a planar capacitor, $G = A/d$, where A is the electrode surface, and d is the distance between electrodes), complex permittivity ε_n* and loss angle δ_n are given by formulas:

$$\varepsilon_n^* = \sqrt{\varepsilon'^2(2\pi R \cdot n) + \varepsilon''^2(2\pi R \cdot n)} \quad (5)$$

$$\delta_n = tan^{-1}\left(\frac{\varepsilon''(2\pi R \cdot n)}{\varepsilon'(2\pi R \cdot n)}\right) \quad (6)$$

Average total dissipation losses of solid insulation material can be expressed as:

$$P_{tot} = \frac{1}{T}\int_0^T v(t) \cdot i(t) \cdot dt \quad (7)$$

where T is the duration of the applied repetitive voltage. Equations (3) and (4) can be substituted into the equation (7) with respect to the orthogonality of sine and cosine functions with different frequencies:

$$P_{tot} = K \cdot \sum_{n=1}^{\infty} 2\pi R \cdot n \cdot \varepsilon_n^* \cdot (a_n^2 + b_n^2) \cdot sin\,\delta_n \quad (8)$$

The above equation (8) can describe any repetitive voltage waveform.

The frequency and temperature dependences of polyethylene terephthalate (PET) and epoxy resin have been discussed and measured by B. Sonerud et al. in [38]. The behavior of both materials was very similar. Some measurement results of the PET are shown in Fig. 20. As is evident from the graphs, the capacitance decreases with growing frequency and increases with rising temperature. The dissipation factor increases with the increasing frequency and increases with the rising temperature as well.

Further, the dissipation factor was determined for square bipolar impulse stresses with variable rise time. Dependence of the rise time of impulses on harmonic power factor, which is a ratio of total dissipation losses to dissipation losses of the fundamental sinusoidal frequency (50 Hz) at room temperature (22 °C), is shown for PET in Fig. 21. Results show that dissipation losses are significantly higher for steep impulses than for sinusoidal shape with the

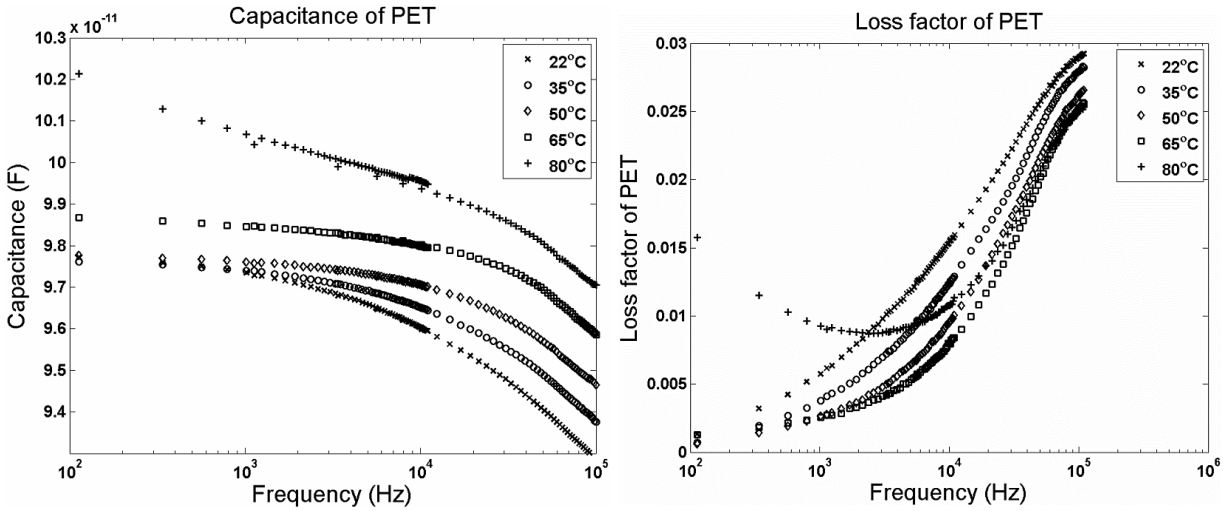

Fig. 20 ***On the left:*** *Frequency dependence of capacitance of PET samples at different temperatures;* ***On the right:*** *Frequency dependence of dissipation factor of PET samples at different temperatures (Reproduced from [38])*

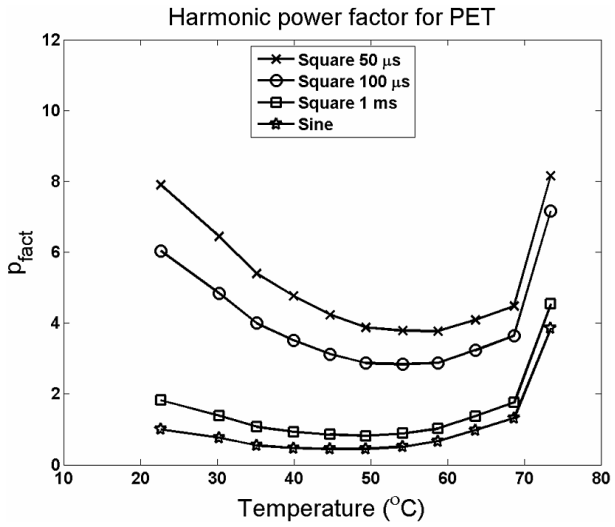

Fig. 21 Temperature dependence of harmonic power factor, which is the ratio of total dissipation losses to dissipation losses of the fundamental sinusoidal frequency (50 Hz) at room temperature (22 °C), for PET for different voltage waveforms (Reproduced from [38])

same period. Power losses significantly increase with the rise time of bipolar impulses, which confirms the theoretical assumptions. In an extreme case performed at room temperature, the total dissipation losses of bipolar square waveform with a rise time of 50 μs reached values about eight times larger than in the case of the sinusoidal waveform of the same RMS voltage.

Another research by K. Niayesh and E. Gockenbach in [39] was focused on the impacts of repetitive trapezoidal impulses on the dissipation factor of solid insulation materials. The authors theoretically explain the influences of rise time, fall time, duration, and repetition frequency of voltage impulses on the total dissipation losses. Numerical simulations were verified by measurements on samples of oil-impregnated paper. Samples were exposed to trapezoidal voltage impulses of 3 kV with varying parameters. The heat generated by the damped oscillation of molecular dipoles significantly stressed the insulation material. The

dissipation factor of the dielectric material, which is directly linked to the heat generation, was growing with the increasing frequency in the range of units to thousands of kHz under the impulse load. The decreasing rise time or period time of impulses significantly increased the dissipation factor. The impulse duration time influenced the dissipation factor as well. The paper has confirmed the increased degradation effect of steep medium voltage impulses on solid insulation materials and has explained some related theoretical aspects.

2.3.2. Partial Discharges in Insulation Systems

A partial discharge (PD) is an incomplete localized electric breakdown of a small portion of gaseous, liquid, or solid insulating medium. PDs can initiate from an electrode or occur in cavities in insulation systems, in which the cavity content has lower dielectric strength than the surrounding insulation material (e.g., air gas voids in epoxy resin). Partial discharges take place in every medium voltage electrical system. Some of them are very weak and negligible, while others, often consequences of long-term stresses or manufacturing errors, are unacceptable for long-term operation. However, in all cases, the behavior of partial discharges depends primarily on the waveform of the applied voltage. Different behavior of partial discharges for different shapes of applied voltages waveforms was observed in various papers [40]-[47]. Investigations on this topic were also conducted by the author's research group in [A3], [A4], and [A8] as well.

In voltage waveforms with conventional higher harmonics, change in PD activity with the increasing frequency of harmonics was observed by M. Florkowski et al. in [40] and [41]. Phase-resolved PD measurements were carried out. The comparison between a 50-Hz sinusoidal voltage waveform and a similar voltage waveform with a significant content of 11^{th} harmonic (THD_V = 11 %) is shown in Fig. 22. From the measurements, it is clear that the increased frequency of superposed harmonic distortions leads to decreased PD intensity (number of PDs), but on the other hand, increased PD magnitudes.

Many research groups have also investigated behavior of partial discharges under square and trapezoidal impulse voltages, e.g., E. Lindell et al. in [42], B. Florkowska et al. in [43], P. Wang et al. in [44], and X. Wang et al. in [45]. The essential parameters of impulse voltages are amplitude, rise/fall time, impulse duration, repetition frequency, and overvoltage of individual impulses depending on the load impedance. All these studies have reached similar conclusions – the rise time and repetition frequency of impulses strongly affects inception voltage, magnitude, and quantity of partial discharges. A higher gradient of voltage (faster rise time) results in lower PD intensity, but higher magnitudes of individual PDs. Repetition frequency and steepness of impulses influence also affect the partial discharge inception voltage (PDIV). Both the increasing repetition frequency and higher steepness of impulses reduces the PDIV. It may be noted that the decrease in PD inception and extinction voltages leads to longer presence of PDs, thereby increasing the magnitude and energy of individual PDs. This effect increases the degradation impacts of PDs on insulation systems. Some examples of the above-mentioned findings are graphically depicted in Fig. 23 and Fig. 24. The

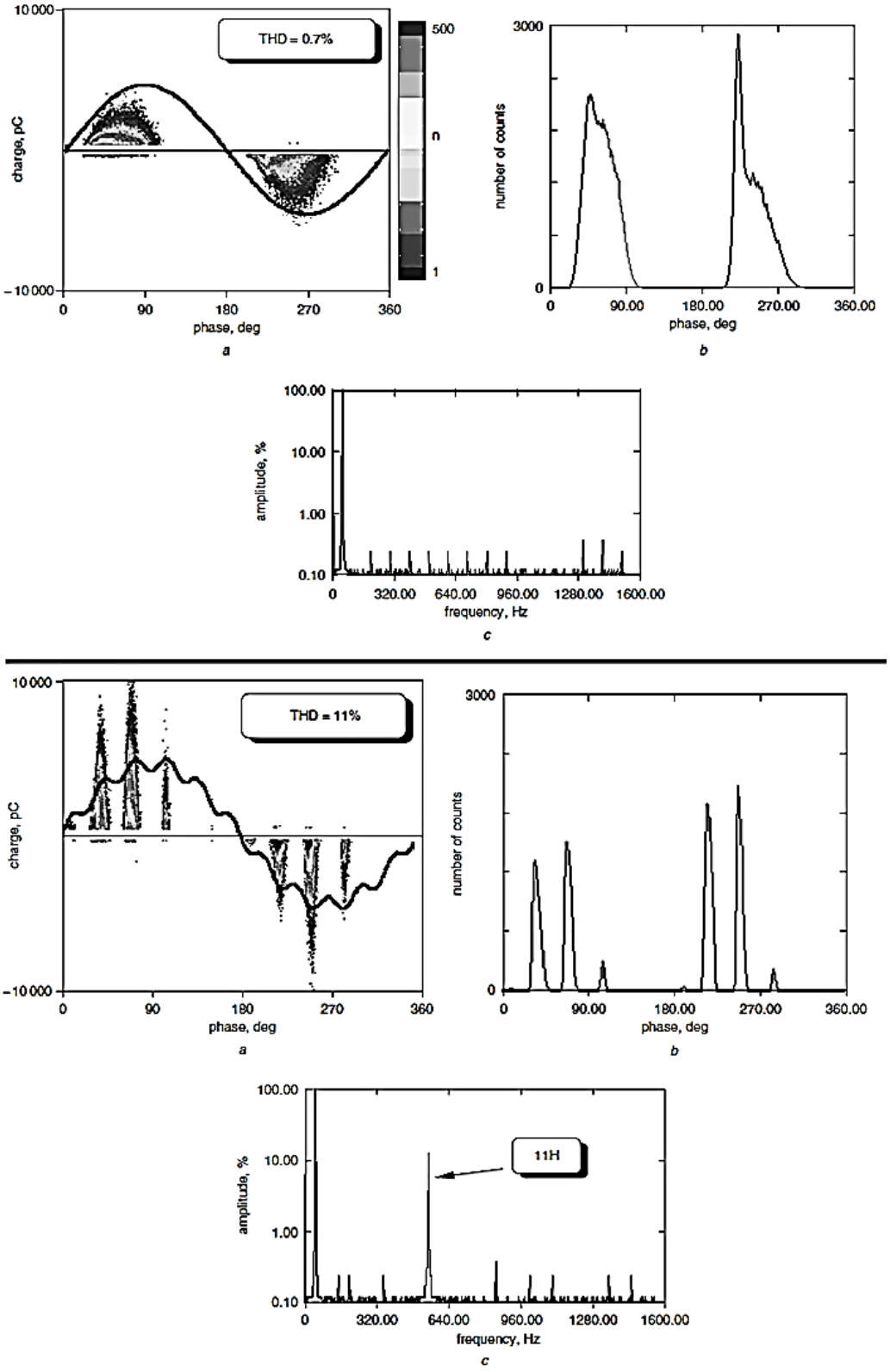

Fig. 22 PD measurements on generator stator bar with polymer thermosetting insulation system at the rms voltage of 15 kV; ***on top:*** *PD measurement at "pure" sinusoidal voltage with the frequency of 50 Hz (THD_V = 0.7 %);* ***down:*** *PD measurement at the same 50-Hz sinusoidal voltage with 11^{th} harmonic (THD_V = 11 %):* ***a)*** *Phase-resolved PD measurement;* ***b)*** *Phase distribution of PD intensity;* ***c)*** *Frequency spectrum of the test voltage (Reproduced from [40])*

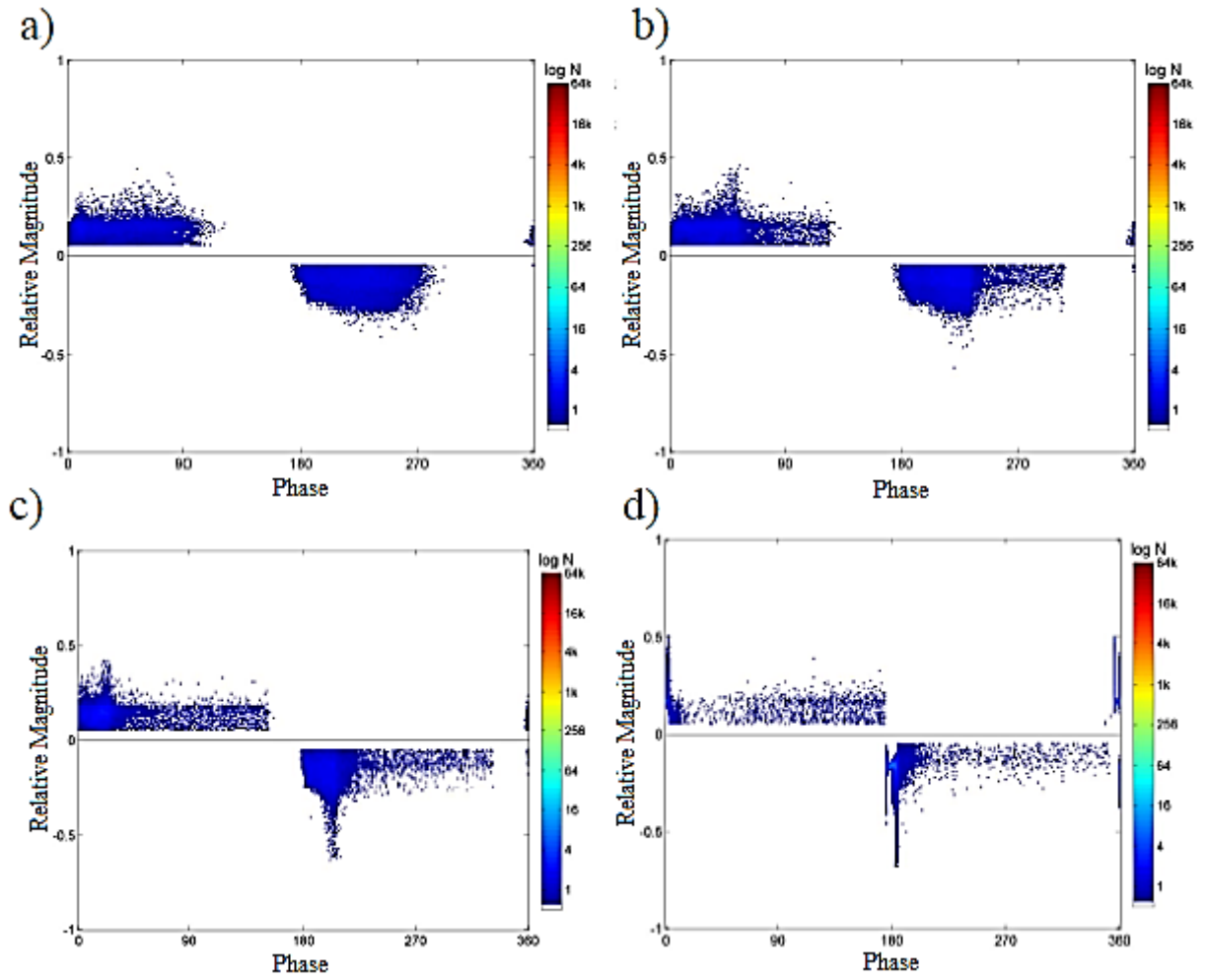

Fig. 23 PD patterns for a cavity in epoxy resin at: ***a)*** *sinusoidal voltage;* ***b)*** *trapezoidal voltage with the rise time of 3 ms;* ***c)*** *trapezoidal voltage with the rise time of 1.5 ms;* ***d)*** *trapezoidal voltage with the rise time of 0.14 ms; the magnitude of the voltage was the same in all cases (Reproduced from [43])*

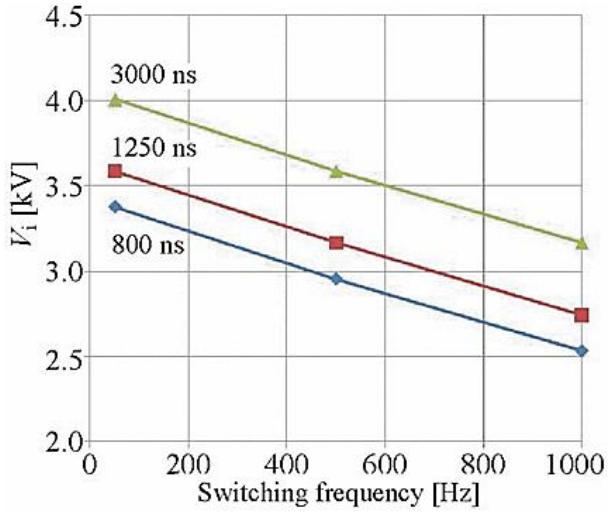

Fig. 24 Dependence of switching frequency and steepness (rise time) of semi-square voltage impulses with the positive slope on the PD inception voltage V_i (Reproduced from [43])

first figure shows the comparison of PD patterns for cavity in epoxy resin under pure sinusoidal voltage and trapezoidal voltage of various rise times at the same voltage magnitude. The other figure shows the dependence of rise time (steepness of impulses) and repetition frequency on the PDIV.

The effects of combined sinusoidal and impulse voltage stresses on PD activity have been so far investigated in only a few studies. Densley et al. in [46] describe measurements on samples of polymeric material under sinusoidal ac voltage with superimposed high impulse voltages. Results show that a single superimposed impulse of high amplitude can initiate PDs that persevere under the original sinusoidal ac voltage, if certain conditions are met. Further relevant experiments on PDs under ac voltage with superimposed high impulse voltages have been published only recently by J. Wu et al. in [47]. This study has been focused on PD characteristics for artificial defects in medium voltage XLPE cable joints under distorted voltage waveforms. Gradual PD initialization was observed during the sequential application of several impulses at constant sinusoidal voltage. The effect of surface charges, which were created by the previous impulse (or impulses), significantly influenced the occurrence of PDs. Both mentioned studies focus only on voltage distortion caused by occasional very high voltage impulses, not high-frequency repetition transients of magnitudes that were much lower than the fundamental voltage magnitude.

The respective investigations of the author's workgroup confirm the findings of the other published studies mentioned above. Measurement setup, which was used in the following studies, was based on the specialized test site that is described in detail in chapter 4. Different behavior of PDs was observed under various distorted voltage waveforms [A8]. Measurements were carried out on the Trichel cylinder and epoxide insulation sample with few artificially-made small cavities. High-frequency distortions of 10 % of the fundamental voltage amplitude were superimposed on sinusoidal rms voltage of 13 kV/50 Hz. The employed shapes of distortions were harmonics of a frequency up to 15 kHz, impulses with a vertically rising edge and exponentially falling edge, and square impulses with a 50 % duty cycle.

As the results indicate, superimposed high-frequency components initiate higher PD activity. This effect is greater in the case of fast impulses than in the case of harmonics. Detailed measurements of PD activity were performed with one specific internal cavity, which was formed of two pieces of Plexiglass (synthetic polymer of methyl methacrylate) [A4]. Hemispherical holes were machined in the center of both parts, which were subsequently glued together under high pressure to form an internal void with a diameter of approximately 2 mm. Damped oscillations with a fundamental frequency of 10 kHz were superimposed on a sinusoidal voltage of 50 Hz with repetition frequency from 700 Hz to 1500 Hz. Magnitudes of superimposed pulses were set to 0 %, 10 %, and 15 % of fundamental voltage amplitude.

Again, significant impacts of voltage distortion on PD activity were observed. PDIV decreases with increasing magnitude of superimposed transients, see Tab. 1. The results also show that the higher peak value of superimposed voltages increases the number of PDs with stronger magnitudes, as shown in Fig. 25. The opposite effect was observed in the measurement, in which the peak value remained constant, and the repetition frequency of superimposed impulses was increased. The magnitude of PDs gradually decreased with

Tab. 1 Dependence of PDIV on the value of superimposed voltage distortion with the repetition frequency of 700 Hz (Adapted from [A4])

Percentage of superimposed high-frequency component	0	10	15
PD inception voltage (kV)	5.1	4.7	4.6

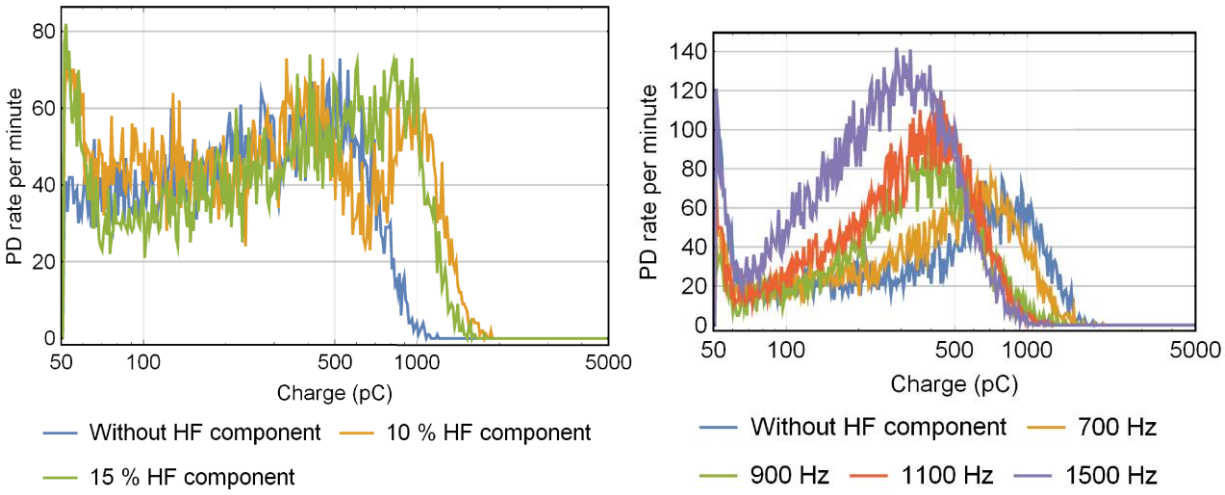

Fig. 25 Dependence of PD rate on charge magnitude; ***On the left:*** *for various peak values and the constant repetition frequency of 700 Hz of the superimposed high-frequency component;* ***On the right:*** *for the constant 10 % peak value and various repetition frequencies of the superimposed high-frequency component (Reproduced from [A4])*

increasing repetition frequency; on the other hand, the PD rate increased with increasing repetition frequency, see Fig. 25.

2.3.3. Development of Surface Discharges

Surface discharges are a specific type of partial discharges. On this basis, behavior of surface discharges at different voltage waveforms is almost the same as that of internal partial discharges. However, there are some substantial differences.

The presence of high-frequency voltages and impulses with fast rise and fall times may increase the delayed polarization of some dipoles in dielectric materials [37]. Moreover, some electrical charges may not disappear with the very fast voltage reversal, and in that case local opposite space charges may form. If the polarization time of some dipoles is longer than the voltage reversal time, a new type of charges may arise. These charges are called blocked charges and create a local opposite polarity of the electric field on the electrode surface. The graphical representation of the polarization effect for sinusoidal and trapezoidal impulse voltages is shown in Fig. 26. The polarization of dipoles in a dielectric material and free charges on the surface of electrodes follows the voltage change of sinusoidal voltage.

Some dipoles react with free charges on the electrode surface at trapezoidal impulse voltage and then are blocked in the last polarization state during a voltage reversal. These

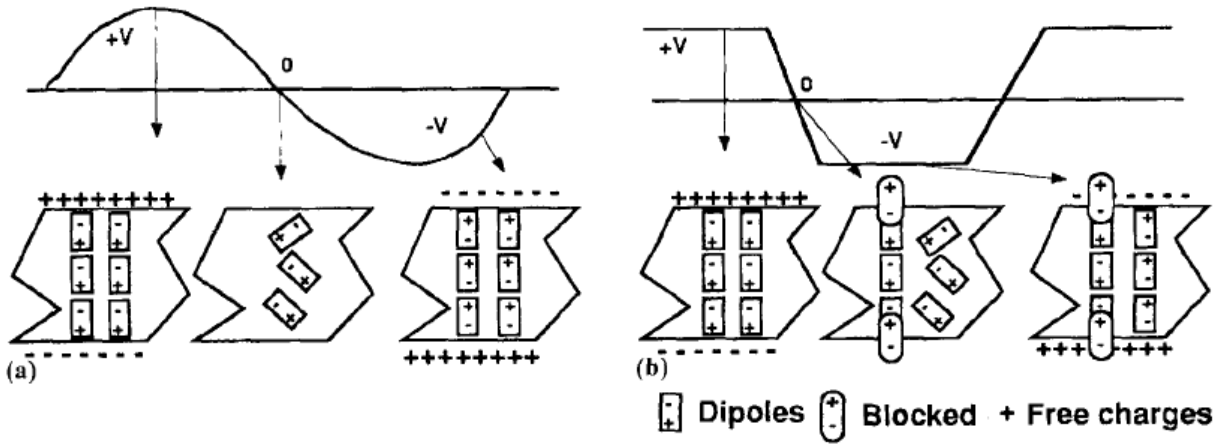

Fig. 26 Graphical explanation of the polarization process of dielectric material: ***a)*** *at sinusoidal voltage;* ***b)*** *at trapezoidal impulse voltage with the very fast rise time (Reproduced from [37])*

blocked dipoles create local differences in potential. An example of a surface potential distribution for applied sinusoidal and trapezoidal impulse voltages is shown in Fig. 27. Local potential differences may support electrical and water tree degradation, surface discharges propagation, and other unfavorable phenomena. The effect of surface charge on surface discharge propagation has been explained by R. A. Fouracre et al. in [48]. The results show that the presence of surface charge strongly influences surface discharges. The surface discharge may continue to propagate even if the initial voltage stress is no longer present. An example of equipotential distribution in the head of surface discharge at the interface of air/solid insulation material with a relative permittivity $\varepsilon_r = 4$ is shown in Fig. 28. The effect of surface charge on surface discharge propagation tends to be greater with the positive polarity of applied impulses. This phenomenon was observed and partially explained by X. Wang et al. in [45].

Many other surrounding conditions affect the development of surface discharges. Although it has been the subject of many researches, a comprehensive explanation and

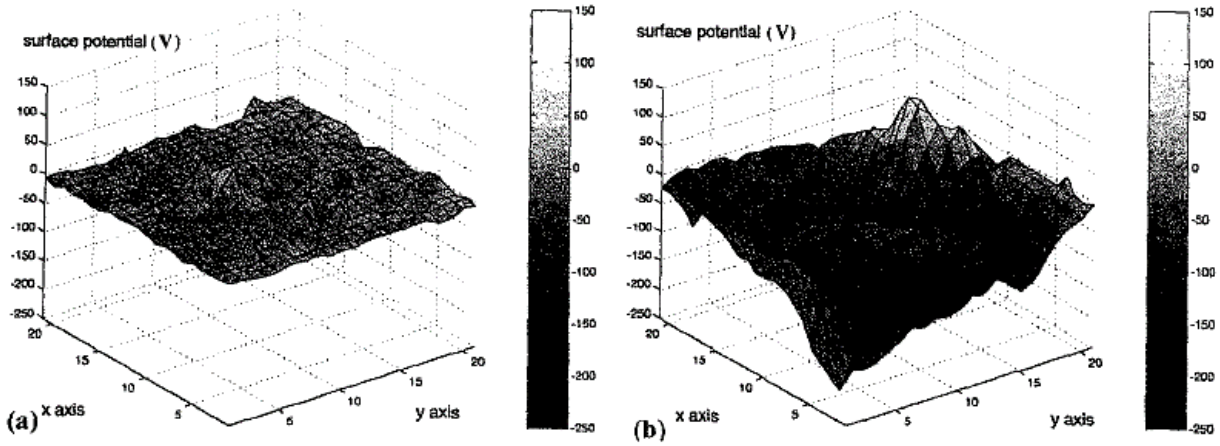

Fig. 27 Example measurements of surface potential distributions on the sample of PET: ***a)*** *after ac sinusoidal voltage stresses;* ***b)*** *after trapezoidal impulse voltage stresses with dV/dt = 5 kV/μs (Reproduced from [37])*

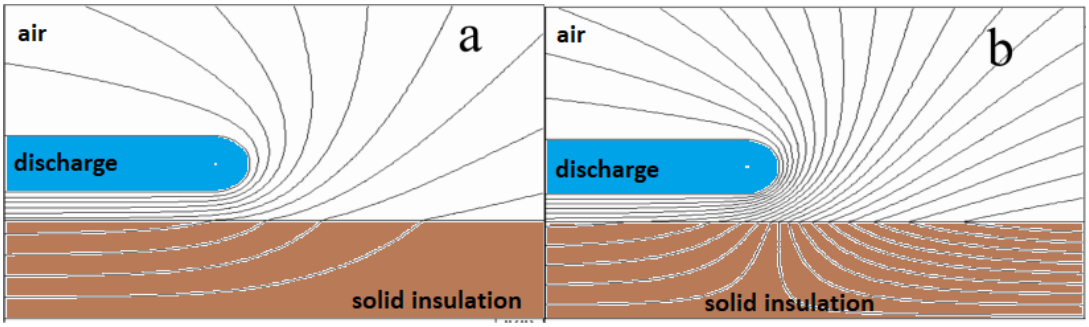

*Fig. 28 Two-dimensional representation of equipotential distribution in the head of a surface discharge on the interface of air/solid insulation material with the relative permittivity of $\varepsilon_r = 4$: **a)** the presence of no surface charge; **b)** the presence of a surface charge (Adapted from [48])*

understanding are still lacking. Possible surrounding conditions, which affect surface discharges, include structure and condition of insulation systems, environmental conditions, etc. For example, the level of surface pollution is a proven impact on surface discharges [A9]. All of this can affect surface discharges differently at sinusoidal voltage stresses and otherwise at impulse or distorted voltage stresses. One of the new problems of stressing materials by steep voltage impulses is surface erosion and migration of electrode atoms into the insulating polymer material, which have been investigated by M. Florkowski et al. in [49] and [50]. This effect is the result of complicated combined action of thermal, electrical, and chemical processes and has not yet been sufficiently explained. A more detailed analysis of this very complex phenomenon is beyond the scope of this thesis.

2.3.4. Overheating of Cable Terminations

Contemporary terminations for medium voltage cables with polymer insulation represent complex insulation components with non-linear electric field distribution. Some investigations address the issue of unexpected heating and degradation of medium voltage cable terminations [51]-[56]. However, the first explanation of this problem has already been given by L. Paulsson et al. in [13]. Semiconducting stress grading materials dissipate ohmic heat as a consequence of the electric field distribution. Heat dissipation may be dramatically increased under fast voltage changes such as high-frequency harmonics or impulse voltages. This process differs slightly from heat dissipations of solid insulation materials described above and is closely related to the non-linear electric field distribution.

Thermal behaviors of cable terminations were investigated at applied high-frequency voltages by Li Ming et al. in [51]. Mathematical models and verification measurements were carried out for the indoor slip-over cable termination with non-linear resistive stress grading at nominal rms voltage stress of 10 kV and frequencies of 50 Hz and 22 kHz. The results of the simulations and measurements are shown in Fig. 29. The thermal simulation corresponds to the measurement of surface temperatures. The large temperature increase was caused by the different electric field distribution. The measurements and simulations indicate a significant heating effect and the occurrence of hot spots on the cable termination surface at high-frequency medium voltage stresses. Fig. 29 (on the right) shows their location. The hot spots were found near the interface between the edge of cable semiconducting layer and the stress

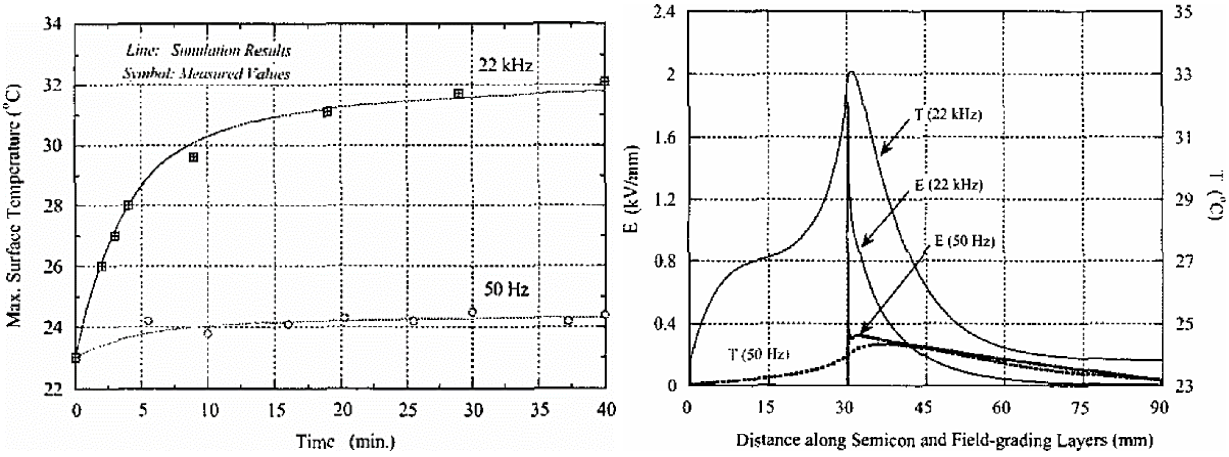

Fig. 29 ***On the left:*** *Measured and simulated maximum surface temperatures of the cable termination at rms voltages of 10 kV/50 Hz and 10 kV/22 kHz as a function of time.* ***On the right:*** *Electric field and temperature distributions along the stress grading layer after 40 minutes of rms voltage stresses of 10 kV/50 Hz and 10 kV/22 kHz (Reproduced from [51])*

grading layer at a termination distance of 30 mm (a distance of 0 mm corresponds to the termination end on shielding wires; a distance of 90 mm corresponds to the other termination end near the cable lug).

Similar investigations were conducted for impulse voltage stresses by research groups around S H. Jayaram in [52]-[54]. The behavior of various stress grading materials under voltage impulses with fast rise times was investigated by the numerical model and verification measurement presented in [52]. Multiple samples of silicone rubber composites were prepared with three different stress grading materials – SiC, ZnO, and ZnO/SiC composite. The determined dissipation losses were practically identical for all the measured samples. The measured thermal conductivity was the lowest for pure ZnO and the highest for ZnO/SiC composites. However, significant hot spots were detected in all samples. The numerical simulation showed that certain materials with high permittivity can have decent resistance to high voltage impulses with fast rise times. Unfortunately, this group of materials is often not suitable for use in medium voltage cable terminations, and so the issue with conventional stress grading materials remains.

In another study, standard cable terminations were exposed to three types of impulse waveforms, i.e., square impulses (with a 50 % duty cycle), PWM impulses, and exponential impulses with fast rise times [53]. The tested terminations were of the conventional cold-shrink type with a concentric stress grading layer. The surface temperature was measured in dependence on the applied voltage values for different switching frequencies. Some results are shown in Fig. 30. Results for PWM impulses and square impulses were almost identical. Higher temperature rise was detected for higher switching frequencies of applied impulse voltages in all cases. Differences in the temperature rise also grow with increasing applied voltage. As can be seen from the resulting curves, the temperature increase for exponential impulses with a switching frequency of 9 kHz is similar to the temperature increase for square impulses with a switching frequency of 2 kHz. Thus, the square impulse waveform generates

more heat dissipation compared to the exponential impulse waveform in the tested cable termination. Electro-thermal numerical simulations with square impulses and additional measurements subsequently confirmed the findings of these measurements [54]. Similar results were observed, and critical points of hot spots were detected at interfaces between the stress-grading layer and the cable semiconducting layer. An example of uneven temperature distribution on the cable termination surface is shown in Fig. 31, which was created by a thermal imager.

The same research groups investigated thermal behavior of cable terminations under combined sinusoidal and high-frequency voltages [55]-[56]. In the first study [55], the electric field distribution was measured along the cable termination at rms voltage of 1 kV/60 Hz in the presence of the conventional 5th harmonic. The surface potential distribution was measured for voltage THDs of 0, 10, 20, and 30 %, respectively. Measured and normalized electric potential distributions are shown in Fig. 32. An increase in electric potential is seen at the interface

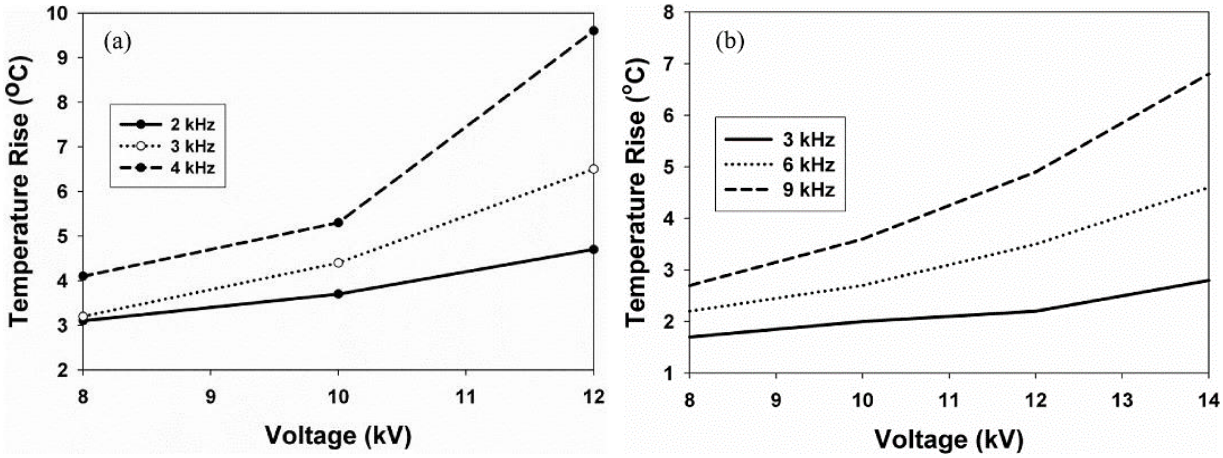

Fig. 30 Maximum measured temperature rises on the surface of the cold-shrink cable termination at different voltages and switching frequencies: ***a)*** *square impulse waveforms (with a 50 % duty cycle);* ***b)*** *exponential impulse waveforms (Reproduced from [53])*

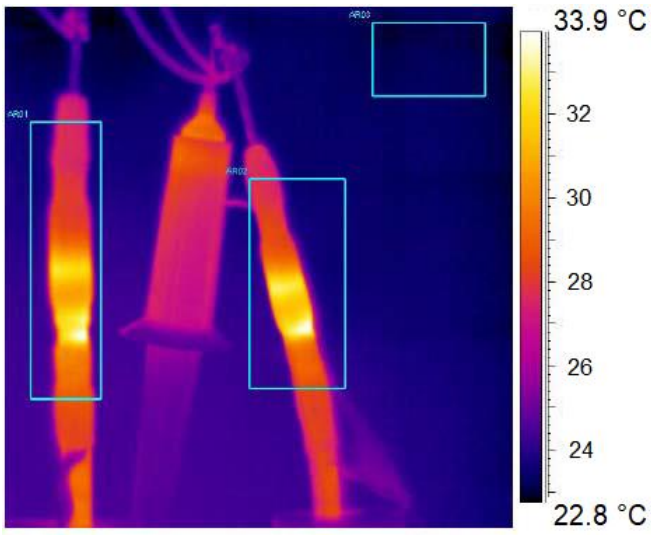

Fig. 31 Example of uneven temperature distribution on the cable termination surface of the cold-shrink cable termination under square impulses; created by thermal imager (Adapted from [54])

between the cable semiconductive layer and the stress grading layer. This effect intensifies with voltage distortion and may cause increased local heat dissipation.

The second similar investigation [56] focuses on measurement of six different types of cable terminations under six various voltage stresses. These stresses were pure power frequency rms voltage (60 Hz) between 0 to 13 kV, high-frequency rms voltage (7 kHz) between 0 to 13 kV, the combination of power frequency rms voltage of 13 kV and high-frequency rms voltage of 0-13 kV, and all above combinations with a power frequency current of 250 A. Maximum temperatures of the cable termination surfaces were measured. A significant temperature increase was observed in the presence of high-frequency voltages. The occurrence of significant hot spots was detected in all forms of high-frequency voltage applications as well. For example, the dependence of surface temperature increase of the cold-shrink cable termination on voltage under different stress conditions is shown in Fig. 33.

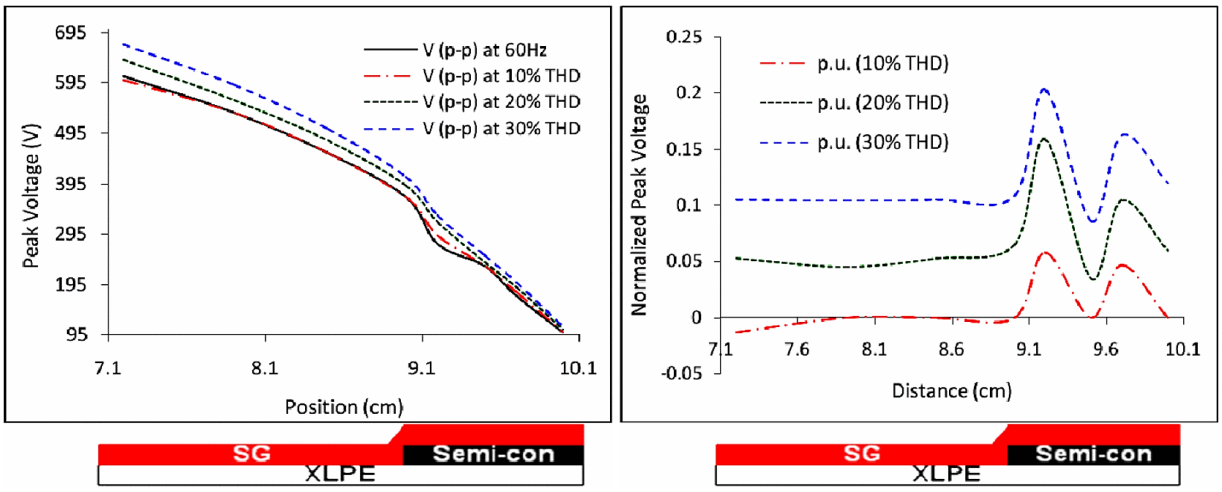

Fig. 32 Measured electric field distribution along the cable termination at a voltage of 1 kV/60 Hz with various THDs: ***On the left:*** *Electric potential distribution;* ***On the right:*** *Normalized electric potential distribution (Reproduced from [55])*

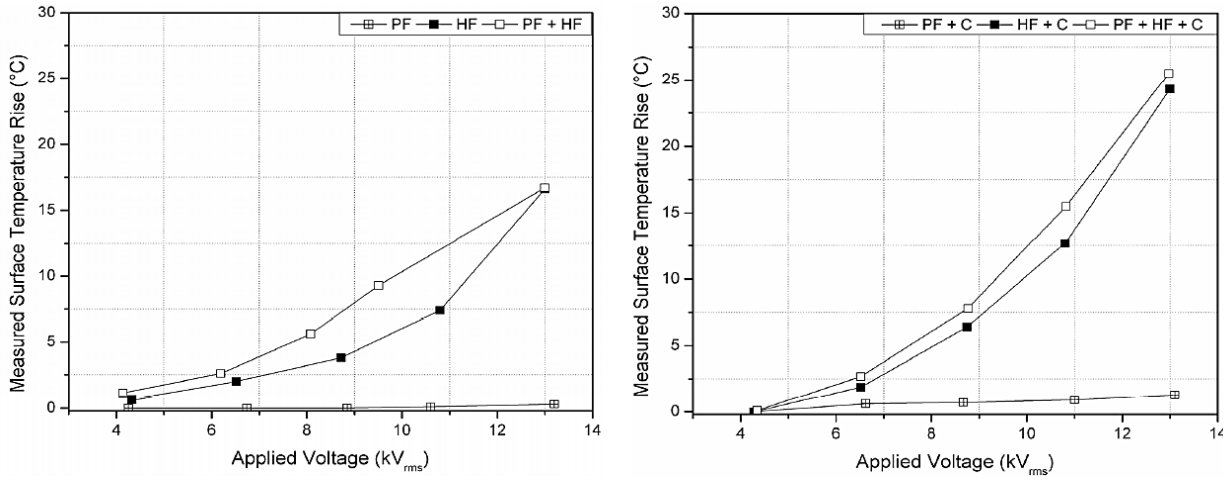

Fig. 33 Maximum measured surface temperature increase of the cold-shrink cable termination at varying applied voltages with different combinations of stresses (legend: PF – power frequency voltage (60 Hz), HF – high-frequency voltage (7 kHz), C – a current flow of 250 A) (Reproduced from[56])

Another result of the paper is the detection of different behavior of various types of cable terminations at high-frequency voltage. The differences originate from the use of diverse stress grading materials and methods of electric field control. The most resistant cable terminations in terms of increased warming under high-frequency voltage distortions were determined to be the ones using the geometric stress grading method (capacitive stress cone). The least resistant cable terminations were the terminations using non-linear resistive metal-oxide stress grading, which are the most widespread.

The different electric field distribution along cable terminations that results into unexpected heating is one of the impacts of high-frequency voltages to medium voltage cable terminations, but not the only one. This effect is closely related to other degradation processes that may be induced or supported by them, e.g., the formation of small cavities resulting in higher PD activity, etc.

2.3.5. Electrical and Water Treeing in Insulation Materials

Treeing is an electrical pre-breakdown phenomenon in solid insulation materials (mainly epoxy resins and polymeric insulation), which was discovered more than 50 years ago. Electrical treeing is a degradation process that creates air channels between electrodes in insulation material. If water is present in the emerging channels, the treeing mechanism is more complicated and is called water treeing.

The initialization of electrical treeing can be explained by the local strengthening of electrostatic field due to the interface roughness or the presence of foreign particles in the insulation material. Besides, electrostrictive forces generated by ac voltage in insulation material may initiate the formation of micro-voids by mechanical stress. Accumulation of space charge on these inhomogeneities and positive-negative cycling of ac voltage may lead to the injection of high energy electrons (hot electrons). These high energy electrons, as well as ultraviolet radiation emitted during charge recombination, cause scission of chemical bonds in insulation materials. The degradation continues by subsequent repetitive electrical discharges that occur inside the miniature voids formed by the bond scission. High energy electrons, ultraviolet radiation, and free radicals enlarge the voids and transform them into small channels, i.e., electrical trees.

In the case of water treeing, the degradation mechanisms are more complicated. However, the initial processes, including cleavage of chemical bonds, are very similar to electrical treeing. The difference lies in the development of micro-voids into larger structures. In this case, there are no high energy electrons or gas discharges. Instead, water molecules penetrate into micro-cracks and micro-voids of the insulation under the influence of the electric field. Subsequently, micro-channels grow from these defects. This process is stimulated by the large electrostatic and mechanical forces that occur at the tips of the created micro-channels. Mechanical forces at the ends of the tips are given by osmotic pressure of water (osmosis is stimulated by the electric field as well, and leads to the forming of supersaturated water solution, from which water precipitates into the area surrounding the tips). The electrostatic forces are given by space charge and are referred to in the literature as Maxwell forces,

Coulomb forces, or electrostatic pressure. These two types of forces are counterbalanced by the mechanical stress inflicted on the structure surrounding the tips, which leads to its erosion.

The process of water treeing strongly depends on the electrical conductivity and composition of the penetrated water. Any chemical reactions of radicals present in the material or the penetrated water strongly affect water treeing development. Water treeing occurs at much lower electric field strength than electrical treeing as well.

The description of treeing phenomena mentioned here is brief, as it represents a very complex issue that goes beyond the scope of this thesis. Moreover, the exact processes of water and electrical tree formations are still not fully understood, despite the numerous studies of the treeing phenomenon that have been published in recent decades. The latest studies also indicate that the simulated electrical and water treeing in laboratory conditions may be different from those occurring in insulation materials in real operations. A more detailed explanation of mechanisms of water and electrical treeing can be found in many studies, e.g., in [57]-[60], which were used for the introductory description in this work. An example of basic tree types is shown in Fig. 34.

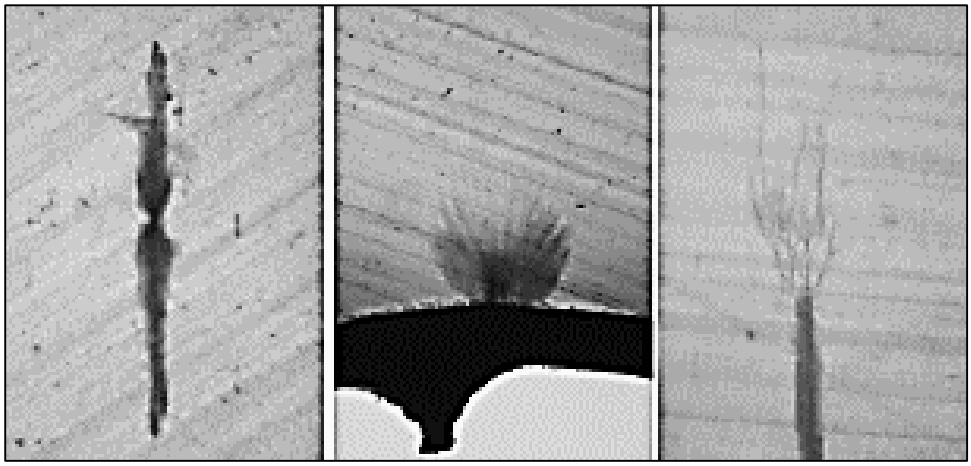

*Fig. 34 Examples of trees that were carried out in the laboratory under various theories of water treeing inception; **from the left:** Bow-tie type tree – a structure formed from an eroded surface; bush type tree (vented tree) – a structure formed from a preexisted micro-channel; branch type tree – a structure formed from the top of a preexisted channel created by partial discharges or different tree types (Reproduced from [60])*

Electrical Treeing under Distorted Voltages

Many studies have been focused on electrical treeing activity under high-frequency voltage stresses, e.g., [61]-[65]. The first laboratory experiments with low-density polyethylene (LDPE), conducted by F. Noto and N. Yoshimura in [61], observed the adverse impact of frequency on the electrical treeing phenomenon over 40 years ago. However, the initialization and following growth of electrical trees were initially associated with a theoretical strong heat generation at the tip of an electrode by dielectric heating of the dielectric material. This idea was partly disproven by the later treeing theories, which are briefly discussed above.

Electrical treeing propagation in the higher frequency range (20-500 Hz) has been more thoroughly investigated later by G. Chen and C. H. Tham in [62]. The authors focused on fractal analysis and time-dependent propagation of electrical trees in a needle-plane arrangement in XLPE samples, which were created from a standard medium voltage cable. The distance between the electrodes was set to 2 mm. The electrical treeing phenomenon was observed until the breakdown of the samples at continuous rms voltage of 7 kV for all cases of various frequencies. Accelerated development of electrical trees with higher frequency was found, which naturally led to a faster breakdown. The growth of electrical trees also shows an almost linear relation to the number of cycles of the electrical field. This effect may indicate that the voltage zero-crossing is responsible for the growth of electrical trees in XLPE insulation.

A similar experimental study was carried out with epoxy resin insulation by I. Iddrissu and S. M. Rowland in [63]. Electrical trees were grown in test samples with a needle-plane arrangement (with a distance between the electrodes of 1.8 mm) at a constant peak ac voltage of 15 kV in the frequency range of 50-450 Hz. The structure and development of electrical trees were recorded every minute using a monochromatic CCD camera with dc-powered backlight illumination. The structures of electrical trees for different frequencies at the time of 5 min after initialization and immediately just before breakdown are shown in Fig. 35. It has been confirmed again that the initialization and development of electrical trees accelerate with increasing frequency of applied voltage; thus, times to breakdown are decreased.

Other investigations were focused on structural analysis of electrical trees under higher frequencies in a similar test arrangement, as in the previously described studies. Experimental research in the frequency range 4-10 kHz by M. Bao et al. in [64] and analysis between

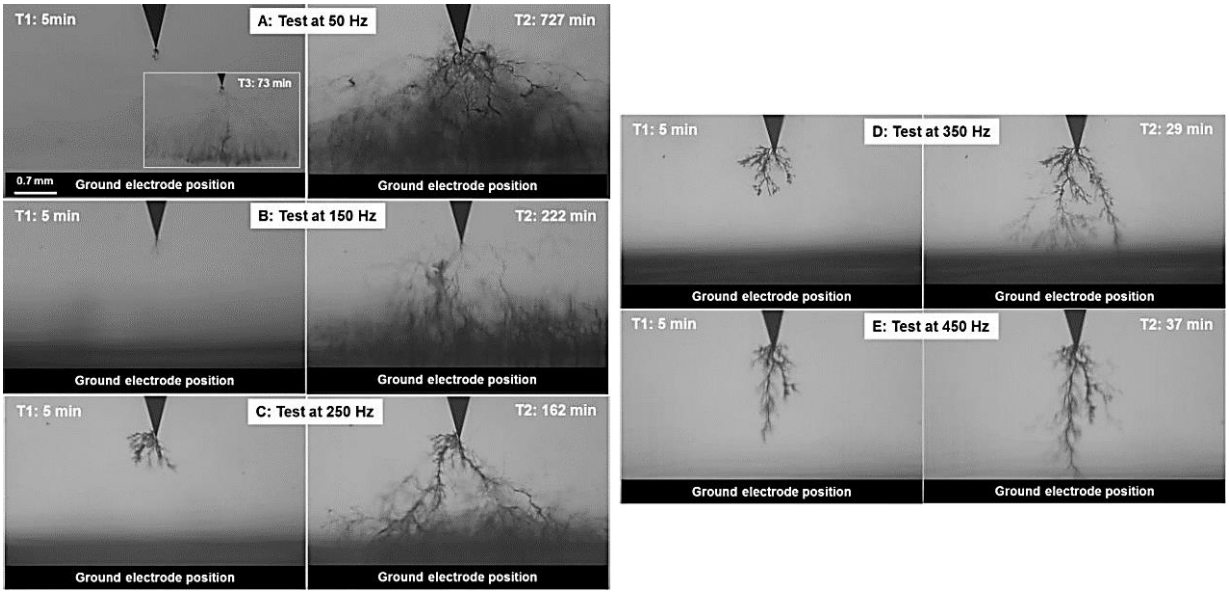

Fig. 35 Structure of electrical trees at voltage frequency of: A) 50 Hz, B) 150 Hz, C) 250 Hz, D) 350 Hz, and E) 450 Hz; T1 = trees at 5 min after initialization, T2 = trees immediately just before breakdown except for image A where the test was manually stopped due to huge damage and time of 727 min; the scale bar of 0.7 mm applies to all images (see fig. part A-T1 at down) (Reproduced from [63])

frequencies of 50 Hz and 130 kHz by Y. Zhang et al. in [65] show shape dependence of electrical trees on the magnitude and frequency of applied voltage. For constant voltage (approximately nominal), the shape of the initial electrical treeing changes with increasing frequency from branch type to bush type. If the intensity of the electric field is high, a bush type of trees is formed directly regardless of the frequency of applied voltage. At frequencies above 100 kHz, bubble formation within trees has been observed, followed by a rapid process of bubble-treeing breakdown, which occurred in tested silicon rubber insulation. Generally, the initial voltage of electrical treeing decreased with increasing frequency of the applied voltage, and the density of the initiated electrical trees was higher at higher frequencies as well.

Furthermore, the impacts of harmonic distortions of power frequency voltage on electrical treeing have been studied by R. Sarathi et al. in [66] and [67]. Test specimens were created from XLPE insulated cable using a sharp needle electrode. Some standard harmonics (2^{nd}-11^{th} order) or their combinations were superimposed on power frequency sinusoidal voltage with various THDs (4%, 10%, and 40%). Moreover, electrical treeing under low-frequency and triangular voltages has been investigated in [67]. In both studies, the branch type of trees was observed under the distorted power frequency voltage. When the level of THD or harmonic order increased, tree structures changed as well. The number of their branches was lower, but their length was increased. It was observed that the shape of the voltage waveform has a substantial impact on the growth of electrical trees. It can be concluded that the increase in the order of superimposed harmonics and the THD causes earlier failure of insulation materials.

Water Treeing under Distorted Voltages

In the case of pure dc voltage, water treeing is not observed (or is very low). The magnitude of the applied ac voltage slightly affects the growth of water trees. However, the increasing frequency of the applied ac voltage significantly accelerates the process of water treeing phenomenon. Many research papers describe these behaviors of the water treeing at high-frequency voltages [68]-[72]. Typical time dependences of water tree lengths at different frequencies of sinusoidal voltage were measured for low-density polyethylene (LDPE) and silicon rubber by N. Yoshimura et al. in [68]. Some of the detected characteristics from this experimental study are shown in Fig. 36. Frequency dependences (for sinusoidal voltage waveform) of water tree growth for three different polymeric materials were investigated experimentally by R. Bartnikas et al. in [69], and results are shown in Fig. 37.

The water treeing in PE (LDPE, XLPE) has been investigated at the power frequency voltage with high-frequency components by some research groups as well [70]-[72]. The results of investigations by research groups around Y. Ohki in [70] and [72] are summarized in Tab. 2. The water tree length, the total number of zero-crossings, and the consecutive number of zero-crossings (defined only for voltages with a 50-Hz component, see Fig. 38) were measured for various combined voltage stresses in a needle-plane configuration with a distance between the electrodes of 0.8 mm. The effect of high-frequency components was unexpected since the growth of water trees was faster for the pure frequency of 2 kHz than for power frequency voltage with superimposed 2-kHz high voltage. A similar result was measured for voltage combinations with a frequency of 4 kHz. This effect can be explained by the different

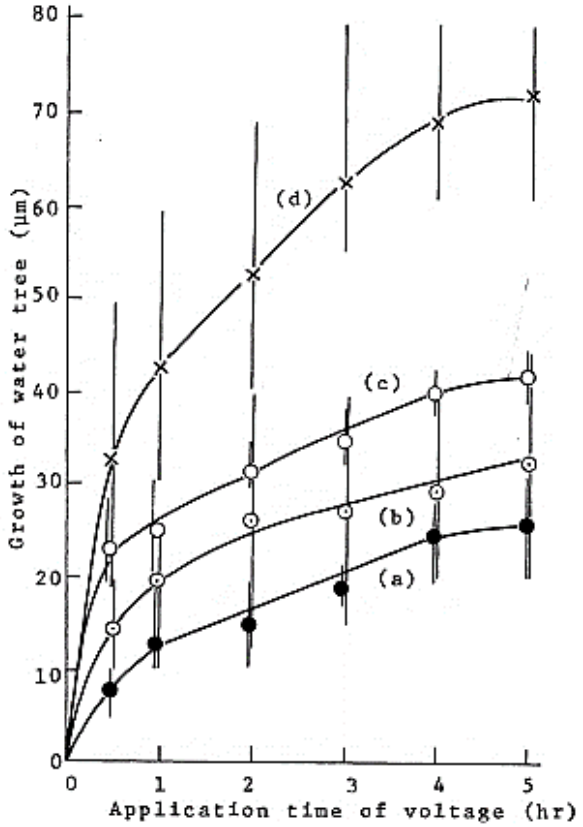

Fig. 36 Time dependence of water tree growth at different frequencies (at ac electric field of 2.5 kV/mm) in low-density polyethylene (LDPE) with the distilled water (with a resistivity of 150 Ω·cm): a) 200 Hz, b) 500 Hz, c) 1 kHz, d) 3 kHz (Reproduced from [68])

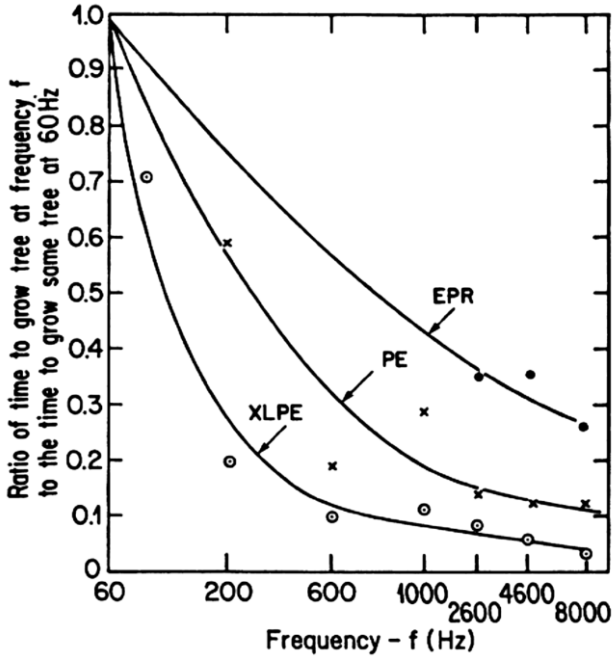

Fig. 37 The growth rate of water trees in dependence on frequency for PE, XLPE, and EPR (Reproduced from [69])

numbers of voltage zeros. The results indicate that the increasing number of zero-crossings enhances the growth of water trees. The dependence of water tree lengths for various combinations of voltage stresses over time is shown in Fig. 39.

Tab. 2 Lengths of water trees grown in a needle-plane configuration of 0.8 mm at various combinations of voltage stresses (Adapted from [70] and [72])

Voltage stress	Water tree length (μm)	Number of zero-crossing:	
		Total for 10 s	Consecutive
50 Hz (13 kV_{rms})	60	1.0×10^3	1
50 Hz (10 kV_{rms}) + 2 kHz (3 kV_{rms})	170	8.0×10^3	9
50 Hz (4 kV_{rms}) + 2 kHz (3 kV_{rms})	260	2.2×10^4	2.3×10^1
2 kHz (3 kV_{rms})	470	4.0×10^4	/
50 Hz (10 kV_{rms}) + 4 kHz (3 kV_{rms})	230	1.6×10^4	1.7×10^1
50 Hz (4 kV_{rms}) + 4 kHz (3 kV_{rms})	330	4.4×10^4	4.3×10^1
4 kHz (3 kV_{rms})	460	8.0×10^4	/

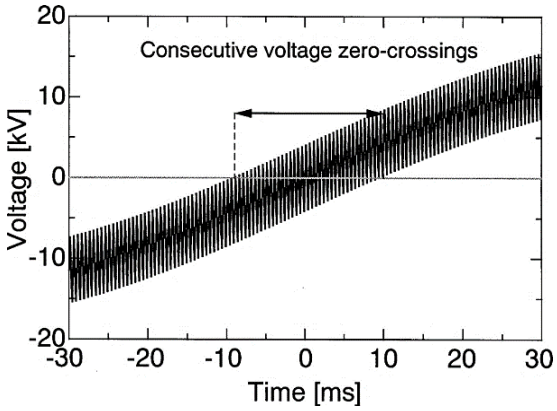

Fig. 38 Example of expressing the consecutive number of zero-crossings (Reproduced from [72])

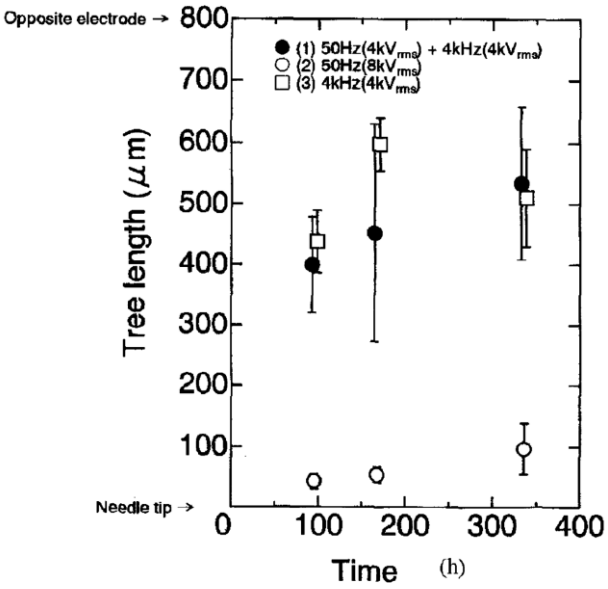

Fig. 39 Dependence of mean lengths of water trees with standard deviations as a function of time for three different voltage stresses in a needle-plane configuration of 0.8 mm (Reproduced from [70])

Other than that, paper [72] examines the overall impact of the high-frequency distortion on various types of baseline voltage, such as power frequency voltage, low-frequency voltage, and dc voltage. The zero-crossing phenomenon has been confirmed and also explained. The impact of various impulse voltage distortions on the water treeing activity can be considered significant due to the proven effects of high-frequency sinusoidal voltage distortions.

2.4. Existing Studies on Aging of Polymeric Insulations under Nonsinusoidal Voltage Stresses

2.4.1. Early Studies on Aging under Nonsinusoidal Voltage Stresses

Research into the aging of electrical insulations and dielectric materials under nonsinusoidal voltage began about 35 years ago. The first studies focus on the effect of standard harmonics, e.g., in [73]-[76]. Recalculation of superimposed voltage harmonics to added dissipation losses was a widely used method of expressing the negative influence of harmonic voltages. Higher dissipation losses mean higher thermal stresses, which were simply used in the Arrhenius thermal aging model and for accelerated thermal aging tests. This investigation procedure demonstrated an increased influence of harmonics on material degradation. However, this method of determining the effects of harmonics on insulation systems is not entirely correct due to the neglect of many other degradation mechanisms.

2.4.2. Aging under Power Frequency Voltage with Standard Harmonics

The research group around G. C. Montanari was the first who began working with accelerated aging models and testing under real nonsinusoidal voltage waveforms, including mainly standard harmonics up to 20^{th} order. Their findings from many years of research have been extensively published, e.g., in [77]-[85].

At first, they developed the standard exponential aging model and inverse power aging model into a specific probability model of aging for self-healing polypropylene power capacitors respecting superimposed standard harmonic voltages in [77]. Subsequently, the model was used to fit and verify results from real aging tests that were performed in a laboratory, see [78] and [79]. Typical harmonics up to the 11^{th} order were used in various combinations and different magnitudes with a fundamental harmonic for test voltage stresses. The effect of nonsinusoidal voltage stresses was investigated by defining three different shape parameters [79]:

$$K_p = \frac{V_p}{V_{1p}} \tag{9}$$

$$K_{rms} = \frac{V_{rms}}{V_{1rms}} \tag{10}$$

$$K_f = \sqrt{\sum_{h=1}^{n} h^2 \left(\frac{V_h}{V_{1rms}}\right)^2} \tag{11}$$

where h is the harmonic order (multiple order) of the angular frequency of the reference fundamental harmonic (voltage with a temporal frequency of 50 or 60 Hz), n is the maximum harmonic order containing an examined voltage waveform, V_{1p} and V_{1rms} are peak and rms voltage of the reference fundamental harmonic, V_p and V_{rms} are total peak and rms values of the examined voltage, V_h is the rms voltage of the h-th harmonic order. The shape factors are given by equations (9) to (11) that identify the peak modification K_p, the rms modification K_{rms}, and the waveshape modification K_f. The authors claim that these shape parameters better describe the voltage waveform than the conventional THD index described in (1) above. Coming from the following derivative, the waveshape parameter K_f is related to the slope of the examined voltage waveform. Let us consider Fourier decomposition of a voltage waveform $v(t)$ that is affected by harmonics:

$$v(t) = \sum_{h=1}^{N} V_h \sin(h\omega_1 t + \varphi_h) \tag{12}$$

where ω_1 is the angular frequency of the reference fundamental harmonic, and φ_h is the phase shift of h-th harmonic according to the fundamental harmonic. If the subsequent derivative is:

$$\frac{dv(t)}{dt} = \sum_{h=1}^{N} h\omega_1 V_h \cos(h\omega_1 t + \varphi_h) \tag{13}$$

then the rms value of the derivative is:

$$\left.\frac{dv(t)}{dt}\right|_{rms} = \frac{\omega_1}{\sqrt{2}} \sqrt{\sum_{h=1}^{N} h^2 {V_h}^2} \tag{14}$$

Dividing equation (14) by the rms value of the derivative of a pure sinusoidal waveform at a supply frequency of 50 or 60 Hz that has the same magnitude of the fundamental component as the distorted waveform, i.e. $V_{1rms}\omega_1/\sqrt{2}$, expresses equation (11). All three shape parameters defined above tend to the value of 1 for a pure sinusoidal waveform of the supply frequency (50 or 60 Hz).

The standard inverse power aging model of the first order has been modified by relating failure time L to characteristic parameters of a voltage waveform K_p, K_{rms}, and K_f [79]:

$$L = L_0 K_p{}^a K_{rms}{}^b K_f{}^c \tag{15}$$

where L_0 corresponds to the life under sinusoidal voltage waveform at the nominal voltage magnitude ($L = L_0$ for $K_p = K_{rms} = K_f = 1$) and coefficients a, b, and c provide some direct material parameters of accelerated aging insulation. This model was used in a logarithmic form to fit the measured results of accelerating aging tests of power capacitors under voltage stresses with standard harmonics.

From obtained results, it was concluded that the evaluation of material aging under voltage harmonics using recalculation of dissipation losses and the Arrhenius model is not acceptable, because the electric field plays a significant role in degradation processes. The effect of increased intrinsic heat generation emerging in capacitors under harmonics was observed to be negligible in comparison with the effect of voltage stresses (up to a value of waveshape parameter $K_f = 20$, which corresponds to very large distortion level). Detailed results with extensive descriptions are given in studies [78] and [79].

Another investigation by the same authors in [80] has detected similar results for polypropylene (PP) and XLPE material samples as well. Results of the investigation of the XLPE insulating material are shown in Tab. 3 and Fig. 40. In both cases, suitable statistical techniques were used to single out the main factors affecting aging. Three used techniques were the analysis of variance (ANOVA), the standardized Pareto chart (SPC), and the main

Tab. 3 Summary of voltage waveforms and life test results of XLPE specimens; E_1, E_3, E_5, E_7, E_{11}, and E_h are the magnitude of the 1st, 3rd, 5th, 7th, 11th, and h-th harmonic component of the applied electric field ($E_1 = E_3 = \ldots = 20$ kV/mm); the harmonic phase angle is 180° with reference to E_1 unless otherwise specified; the symbol ° indicates phase angle of 0°; the times to failure, corresponding to 63,2% probability, are given with 90% confidence intervals (Adapted from [80])

Sample #	Supply voltage ($E_1 = E_3 = \ldots = 20$ kV/mm)	E_{rms} (kV/mm)	E_p (kV/mm)	K_f (-)	K_p (-)	K_{rms} (-)	t_f (h)
1	$3E_1$	60.0	84.8	1.00	3.00	3.00	14.0 (6; 34)
2	$2.82E_1$	56.5	79.9	1.00	2.82	2.82	114 (70; 185)
3	$2.82E_3$	56.5	79.9	3.00	2.82	2.82	45.7 (7; 336)
4	$2.82E_5$	56.5	79.9	5.00	2.82	2.82	12.9 (3; 53)
5	$2.87(E_1 + 0.1\Sigma^{19}_{h=3}E_h)$	60.0	79.9	3.66	2.82	3.00	16.6 (3; 110)
6	$3.01(E_1 + 0.1\Sigma^{19}_{h=3}E_h)$	63.0	84.8	3.66	3.00	3.15	2.2 (0.22; 22)
7	$0.86(E_1 + E_3 + E_5° + 0.5E_7)$	31.0	84.8	6.87	3.00	1.55	47.0 (4; 532)
8	$2(E_1 + E_3°)$	56.5	87.0	3.16	3.08	2.82	5.0 (0.68; 36)
9	$2(E_1 + E_3)$	56.5	113.0	3.16	4.00	2.82	0.25 (0.1; 0.5)
10	$2(E_1 + E_5°)$	56.5	113.0	5.10	4.00	2.82	0.05 (0.03; 0.07)
11	$2.82E_{11}$	56.5	79.9	11.00	2.82	2.82	3.9 (1.0; 15)
12	$1.41(E_1 + E_{11})$	39.9	79.9	11.00	2.82	2.00	24.8 (7.6; 81)
13	$1.15(E_1 + 1.5E_{11})$	41.4	79.9	16.50	2.82	2.07	5.5 (1.9; 16)
14	$2.5E_1$	50.0	70.7	1.00	2.50	2.50	215 (125; 372)
15	$3E_1 + 0.5E_5°$	60.8	98.9	1.30	3.50	3.04	3.7 (0.82; 16)

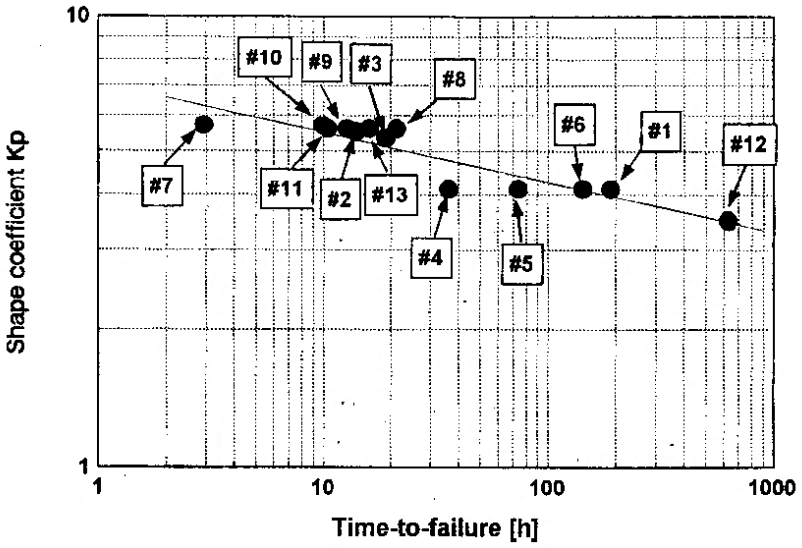

Fig. 40 Life behavior of XLPE specimens as a function of shape coefficient K_p (peak voltage) for various types of waveforms from Tab. 3 (Reproduced from [80])

effect plot (MEP). Statistical analyzes (ANOVA, SPC, and MEP) for PP and XLPE materials are shown in Tab. 4 and Fig. 41.

The ANOVA technique provides an estimate of the variance of the test results as a function of test factors, where greater variance means a greater influence of determining factors on the aging mechanism. Tab. 4 contains the values of a mean square (MS) for each test factor that is proportional to the variance. Values of F-ration and P-value, which were obtained from significance tests, are also shown in the table, where greater F and lower P indicate greater statistical significance. All these indicators support the prevailing statistical significance of peak voltage on the lifetime of XLPE and PP insulation materials.

A similar result is obtained by the SPC and the MEP, as shown in Fig. 41. The SPC relates the logarithm of experimental waveshape parameters K_p, K_{rms}, and K_f to the logarithm of a lifetime and provides a size of the ratio of the estimated effect on the relevant standardized error. The vertical thicker line in the SPC indicates the lower 95% significance limit, which characterizes the non-negligible significance of the evaluated parameters on lifetime with respect to its variance. Both SPCs for XLPE and PP show the importance of all waveshape parameters on the lifetime statistically. The MEP also confirms the significant dependence of peak factor K_p on lifetime for both tested materials. The lines represent the estimated effect of each factor, in which a higher slope indicates a more significant impact of the relevant factor on the lifetime. Therefore, all results show the significant effect of added peak voltage due to

Tab. 4 Results for XLPE and PP materials obtained by ANOVA for effects of logarithms of waveform shape parameters on the logarithm of life (Adapted from [80])

Source	XLPE			PP		
	MS	F	P	MS	F	P
$\ln K_f$	10.75	38.67	0.0002	2.90	33.38	0.0007
$\ln K_p$	38.10	137.0	0.0001	3.57	41.25	0.0004
$\ln K_{rms}$	7.83	28.18	0.0005	0.51	5.93	0.0451
Total Error	0.28			0.086		

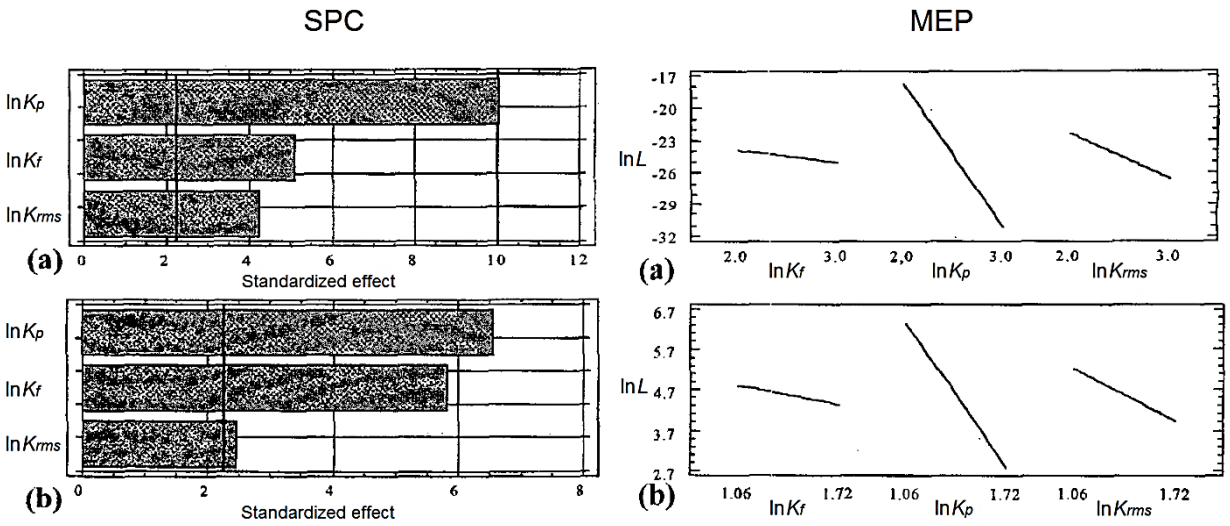

Fig. 41 SPC (on the left) and MEP (on the right) relevant to the estimated effects of logarithms of waveform shape parameters on the logarithm of life; the vertical thicker line in the SPC indicates the lower 95% significance limit; a) XLPE insulation, b) PP insulation (Reproduced from [80])

voltage distortion on intrinsic aging of XLPE and PP insulation materials. The impact of voltage waveshape and then the rms voltage is smaller but also statistically significant.

Thermal stresses were added into aging under harmonic voltages in subsequent investigations [81] and [82]. Life tests were performed at three different temperature levels (20, 60, and 90 °C) to obtain information on the multi-stress behavior of the power capacitors. The thermal parameter was defined for factorial analysis as:

$$T = \frac{1}{\theta_0} - \frac{1}{\theta} \tag{16}$$

where θ_0 = 293 K is the reference (room) temperature, and θ is the test temperature. Then the thermal parameter can be added into the modified inverse power aging model from (15):

$$L = L_0 {K_p}^a {K_{rms}}^b {K_f}^c T^d \tag{17}$$

where coefficients *a*, *b*, *c*, and *d* provide some direct material parameters of insulation under accelerating aging. Equation (17) can be written in an alternative logarithmic form according to the well-known Arrhenius thermal aging model [81]:

$$ln\, L = ln\, L_0 - a\, ln\, K_p - b\, ln\, K_{rms} - c\, ln\, K_f - kT \tag{18}$$

where *k* is the thermal material coefficient. This structure of equation (18) usually fits the measured data better than (17) and was used to evaluate measurements on power capacitors in studies [81] and [82]. Statistical analyses SPC and MEP from this experiment are shown in Fig. 42. The SPC shows that all proposed parameters are statistically significant, with a probability of 95 % (the estimated effect is greater than the limit value marked by the dotted vertical line). Peak value parameter K_p is the predominant among the considered aging factors, resulting from the MEP. In the following order of significance, K_{rms}, T, and K_f were found for

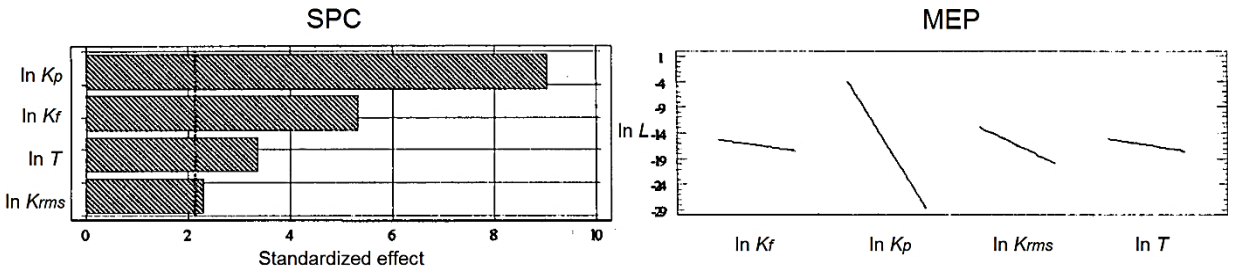

Fig. 42 SPC (on the left) and MEP (on the right) relevant to the estimated effects of logarithms of waveform shape parameters on the logarithm of life for the tested power capacitor; the vertical dotted thicker line in the SPC indicates the lower 95% significance limit (Reproduced from [81])

the tested power capacitor. Unfortunately, this investigation, which considered the influence of thermal stress, was only carried out on the self-healing power capacitor and not on any cable insulation. The lifetime of XLPE materials may be differently influenced by each proposed experimental waveshape or thermal parameters.

Finally, all research works on this issue by G. C. Montanari et al., including the above, have been summarized in the three-part article [83]-[85]. Publications generally discuss the origin of harmonic voltage distortion in electrical systems and its effect on electrical insulating and dielectric materials. Especially, the impact of harmonics on power capacitors (with PP dielectric material) has been explained, as well as effects of PWM on PDs in enameled wire insulations of ac motors. However, this is another type of insulation system that does not occur in the medium voltage cables.

The following investigations of the aging of polymeric materials by other research groups generally show the adverse impact of harmonics on long-term degradation of electrical insulations as well. An example may be experimental studies with epoxy resin by S. Bahadoorsingh et al. in [86] and [87], or investigations of XLPE insulation materials by R. Sarathi et al. in [66] and [67]. All these studies were carried out on material specimens in needle-plane configurations, observing propagations of electrical trees and lifetime characteristics at a specific voltage with harmonic distortions.

Harmonics up to the 25th order were used in various combinations to form the distorted voltages for testing epoxy resin insulations by S. Bahadoorsingh et al. in [86] and [87]. Parameters THD_V and K_f, as defined in equations (1) and (11) above, were used to evaluate the test voltage waveforms. These detected parameters were subsequently compared according to breakdown times for different shapes of voltage waveforms. Thermal stresses were not included in these experiments. Observed data from lifetime tests were also used for statistical analyses using a two-parameter Weibull distribution. The used cumulative density function of the distribution can be expressed according to the joined standard IEC 62539/IEEE 930 [88]:

$$F(t) = 1 - e^{-\left(\frac{t}{\alpha}\right)^{\beta}} \tag{19}$$

where t is a random variable (usually time to breakdown), α is a scale parameter, and β is a shape parameter of the distribution. The scale parameter α represents the time to failure with a probability of 63.2 %, which is analogous to the mean of the normal distribution. The shape parameter β is a measure of the range of breakdown times. The function $F(t)$ indicates the

proportion of tested specimens that fail at time *t*. The linear natural logarithmic relationship for the estimation of parameters using a graphical method is given by:

$$\beta\, ln(t) - \beta\, ln\,\alpha = ln\big[-ln\big(1 - F(t)\big)\big] \tag{20}$$

An example of selected Weibull plots for results from [86] is shown in Fig. 43. Statistical analysis of failure times at approximately constant parameter K_s and increasing THD_V yielded the reduced Weibull shape parameters that indicate earlier failure rates despite less than 10% variation in respective Weibull scale parameters. This effect was not observable for constant THD_V and increasing parameter K_s. Greater influence of the 7th harmonic compared to the 5th harmonic on the degradation was also observed at voltage waveforms with identical peak values. Besides, waveforms with a combination of more harmonics, which were characterized by higher distortion levels, produced consistently larger α values. The β plots revealed a slight effect that more distorted waveforms produced proportionally larger β values. The main conclusion from these investigations by S. Bahadoorsingh et al. is confirmation of faster degradation of insulations under distorted voltage.

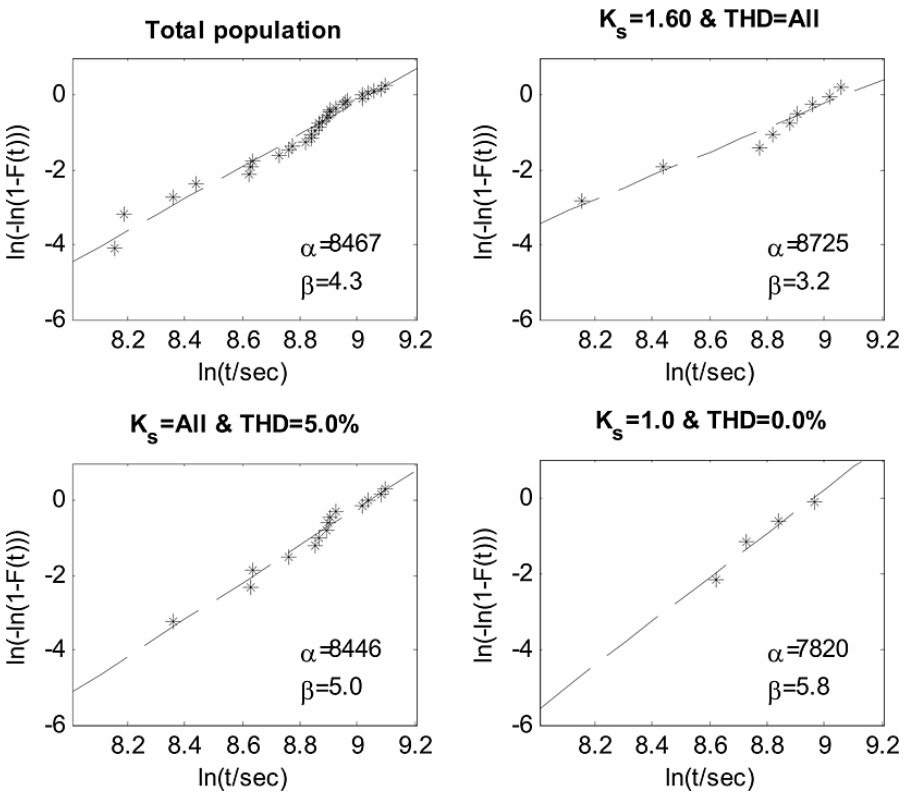

Fig. 43 Weibull plots with α and β values of the total sample population and three subsets: K_s = 1.60, THD_V = 5 %, and undistorted waveform where K_s = 1.00 and THD_V = 0 % (Reproduced from [86])

Treeing phenomena and lifetime investigations for XLPE insulation materials by R. Sarathi et al. in [66] and [67] were carried out at voltage waveforms with combinations of THD_V up to 40 % and harmonics up to the 11th order. Two-parameter cumulative Weibull distribution was used for statistical evaluation as well, see expressions (19) and (20). An example of resulting Weibull plots is shown in Fig. 44. Graph a) shows a significant reduction in the lifetime for the 50 Hz triangular voltage stress than for the 50 Hz sinusoidal

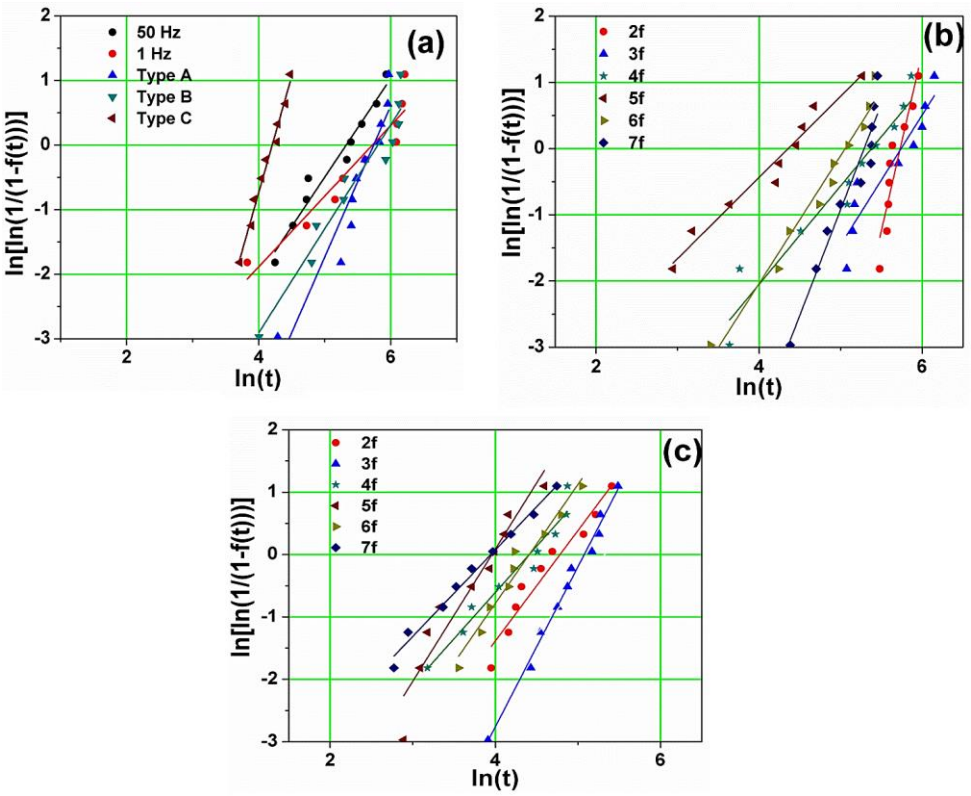

Fig. 44 Weibull plot for failure time of XLPE insulation due to electric trees under harmonic ac voltages; a) voltage without higher harmonics having the identical peak value (Type A: frequency of 50 Hz for 1 hour then 1 Hz until to failure; Type B: frequency of 50 Hz for 2 hours then 1 Hz until to failure; Type C: 50 Hz triangular voltage), b) sinusoidal voltage with THD_V of 4 % and different harmonic order, c) sinusoidal voltage with THD_V of 40 % and different harmonic order (Reproduced from [67])

voltage stress, which has additionally reduced the lifetime compared to the 1 Hz sinusoidal voltage stress. Other graphs show a shorter lifetime with increasing THD_V as well as with increasing order of superimposed harmonics. Four different phase shifts of superimposed harmonics from the fundamental harmonic were investigated in the context of lifetime testing. However, the results showed no significant impact on the degradation rate of tested XLPE insulations. Based on this study, it is suggested that the voltage waveshape (du/dt rate) has a greater impact than the peak voltage factor. This finding is conflicting with the results of Montanari et al. as described above.

2.4.3. Aging under Square Impulse Voltages

Various research groups conducted lifetime experiments of polymeric materials under square impulse voltage waveforms, e.g., in [89]-[91]. Some material structure changes were discussed by Y. Cui et al. in [89] and M. Florkowski et al. in [90]. A significantly shortened lifetime of tested XLPE samples was detected for PWM voltage shape in comparison with power frequency ac or dc voltage. An example of some detected lifetime curves for different frequencies and amplitudes of test voltage impulses at different thermal stresses is shown in Fig. 45. The strong impact of temperature and frequency on the lifetime is evident. This type of

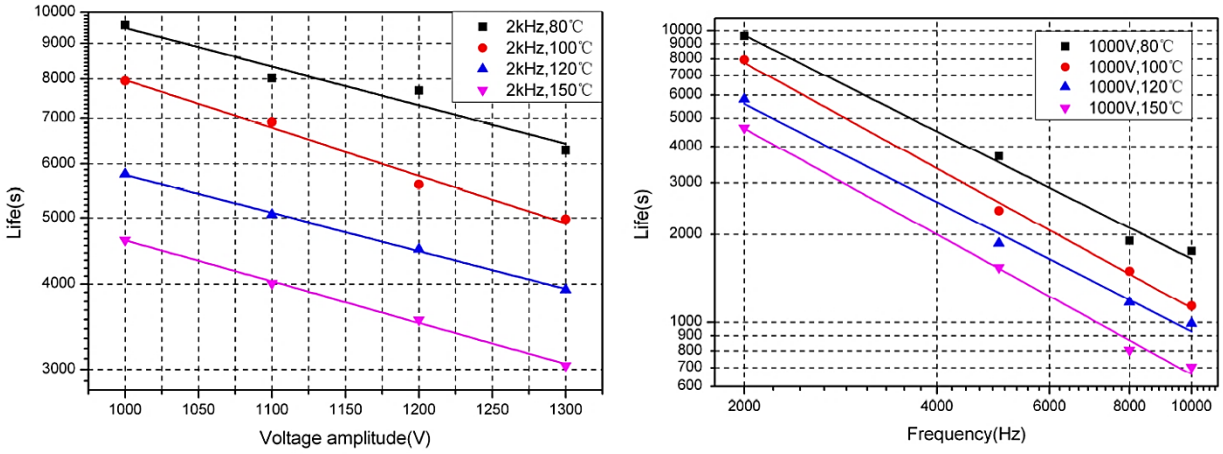

Fig. 45 Lifetime curves of polyimide film under continuous square impulses; ***On the left:*** *Aging life affected by the amplitude of voltage impulses;* ***On the right:*** *Aging life affected by repetition frequency of voltage impulses (Reproduced from [89])*

voltage stresses is closely related to the direct connections between motors and their ASDs. Due to power quality standards and standards for connecting power electronic devices, power systems with medium voltage cables are not usually stressed directly by square impulses.

2.4.4. Aging under Sinusoidal Voltage with Switching Impulses

Several accelerated aging studies were performed for cross-linked polyethylene (XLPE) and ethylene-propylene rubber (EPR) cables with a nominal line voltage of 15 kV by the research group around S. Grzybowski. The first laboratory tests were carried out only with switching impulses, e.g., published in [92]. After that, subsequent experiments, which have been published in [93] and [94], were conducted under multi-stress conditions, including increased temperature, power frequency voltage, and switching impulses. Used switching impulses had the standard shape of 250/2500 μs (front/tail time).

In the first multi-stress case, see [93], voltage impulses of the positive polarity with a magnitude of 62 kV were combined with ac power frequency rms voltage of 26 kV (3 times higher than the nominal phase voltage of tested cables). The set stress temperature of 70 °C of cable cores was given by ac current flow of 226 A. Constant ac voltage and current were continuously applied to the EPR cable sample, and 1000 switching impulses were applied every 100 hours with an interval of 30 seconds between each impulse. Partial discharges inception voltages (PDIVs) were measured every 50 hours. The aging was completed after 1300 hours, and then breakdown tests were performed. Similar measurements were carried out only for pure ac voltage stress and for pure ac voltage stress with the current load. Results of all measurements were compared, and a lifetime model has been discussed.

Reductions of PDIV after aging were not observed for samples that were exposed only to ac voltage stress. However, the PDIV was reduced by 26 % for samples that were exposed to ac voltage stress with the current load. Further, the PDIV was reduced by 44 % for samples that were exposed to the combined stress with superimposed impulse voltages. The charge magnitude of PDs was increased by the aging of about 53 % for ac voltage stress with the current load and about 75 % for combined stress with superimposed switching impulses. A large impact of multi-stress on the lifetime has been detected and confirmed by breakdown tests.

The impact of switching voltage impulses with a magnitude of 100 kV on cable insulation aging was also observed in the last paper [94]. Ten thousand switching impulses were successively applied to insulation samples of 15 kV cables with a time interval of 30 seconds between each other. The effect of aging was detected by decreasing PD inception and extinction voltages and decreasing breakdown voltages of cable insulations. This effect was confirmed by the increasing charge magnitude of PDs as well. The results were discussed with the exponential life model, using the lifetime estimation of measured cable samples, see Fig. 46.

Another research by M. I. Qureshi et al. in [95] was focused on accelerated laboratory aging of heat-shrink cable joints that are a part of medium voltage cable systems. The authors tested cable joints that were produced by four different manufacturers for a nominal line voltage of 15 kV. Aging stresses consisted of power frequency voltage, daily heating cycles, and successive switching impulses. Power frequency ac voltage of three times the nominal value was continuously applied for 63 days. The current transformer generated a heating current flow of 2 kA in the test loop to reach a core temperature of cable joints of 130 °C for 8 hours each day. For the rest of each day, tested samples were without heating. Every 7 days, the tested samples were disconnected from the test circuit, and a group of standard switching impulses (250/2500 µs) with a magnitude of 71 kV was applied to them. Each group of impulses consisted of 170 impulses of positive polarity and 170 impulses of negative polarity.

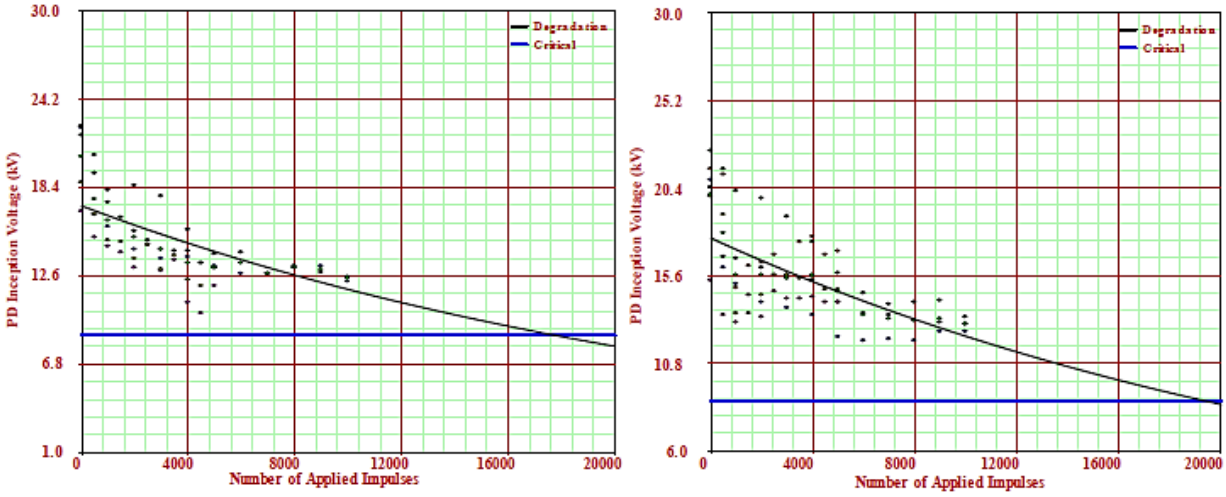

Fig. 46 Extrapolated curves for estimating the lifetime of measured cable samples from PDIVs that were measured during the aging process; ***On the left:*** *Measured data and estimation for the XLPE cable;* ***On the right:*** *Measured data and estimation for the EPR cable (Reproduced from [94])*

Each type of cable joints was aged in air and the water tank parallelly.

PDs and dissipation factor (successively under a frequency of 50 Hz and 0.1 Hz) were measured for all tested samples before and after the aging process. PD inception and extinction voltages have clearly shown severe degradation of tested cable joints. Increased dissipation factors have indicated aging as well. However, it has been only shown substantially and clearly with measurements at a frequency of 0.1 Hz, having a better resolution. Breakdown tests, which were performed after the aging processes, have shown no impact of aging to resulting breakdown voltages. This phenomenon may be due to the structure of the cable joints and the type of failure (breakdown path). Almost always, the breakdown path ran longitudinally along with the interface between the cable insulation and joint body. All result tables with specific numbers are listed in [95].

2.4.5. State of the Art of Research into Aging and Degradation Processes under Nonsinusoidal Voltage Stresses

All of the presented degradation mechanisms of medium voltage insulation systems, which are exposed to voltage stresses with high-frequency distortions, evoke current needs for comprehensive investigations of material aging. The great challenge is that most of these mechanisms have not yet been sufficiently understood and explained. However, all impacts of voltage distortions on insulation systems are closely interrelated. Therefore, the current greatest challenge is to understand the more complex impact of combined degradation mechanisms on the lifetime of compound insulation systems.

Some accelerated aging researches under combined multi-stress have already been carried out. However, the real operating conditions were usually not respected. Tested objects were often only material samples. Extremely high magnitudes of overvoltages were also used as well, e.g., Montanari et al. used the same size of superimposed harmonic voltages as the fundamental voltage, or Grzybowski et al. applied voltage impulses with a magnitude of 100 kV to cables with a nominal voltage of 15 kV. Besides, high-frequency voltage distortions, which occur in power systems with power electronic installations, have not been used in any investigation on accelerated aging conducted so far. The accelerating aging studies, as mentioned above, have been performed under their specific conditions, which are not realistic in real operations.

Moreover, the recent article by M. Ghassemi in [96] demonstrates that this issue is very current. The review has summarized many performed studies and shows their inconsistency. The aging processes of whole real insulation systems under combined nonsinusoidal voltage and thermal stresses are not understood yet. Even some studies in the review contradict each other, and aging models are often not sufficiently accurate. It also notes that realistic studies of real complex insulation systems under actual conditions from operations are still missing. It is essential for the quality design of insulation systems for future power systems with increasing power electronics installations.

Therefore, further investigations are needed to more accurately verify and understand the impact of voltage distortion on a complex cable insulation system in real electrical networks. Such simulation of realistic conditions could be a test of complex medium voltage cable system at maximum allowable temperature and system voltage with superimposed high-frequency oscillation impulses of 15 % of fundamental system voltage. This following comprehensive experimental investigation is the main object of this thesis.

3. VERIFICATION OF HIGH-FREQUENCY VOLTAGE DISTORTION IN POWER GRIDS USING NUMERICAL MODEL

3.1. Motivation for Numerical Model

Due to the challenges connected with both equipment demands of higher-frequency range voltage measurements and obtaining a permit to perform them in a real power system, a numerical simulation was needed to verify possible shapes of distorted voltage waveforms. A photovoltaic (PV) power plant with an installed power of 1 MW was chosen as the modeled object, as it represents a typical application of power electronics with larger power flow in the area of Central Europe.

As was found in previously published investigations, the distortion emitted by a large PV power plant can be transferred from a low voltage level to a medium voltage level of the distribution system. For example, this phenomenon was observed by T. Joshi et al. in their simulation study [29]. Various operation modes of the 700-MW PV power plant, which was installed at the low voltage level, significantly changed the impedance resonances of the power system at the medium voltage level. Unfortunately, no examples of voltage waveforms are included in this study. The excitation of harmonic resonance oscillations in a medium voltage distribution system by harmonic emissions from a large PV power plant, which was installed at the low voltage level, was simulated by R. R. A. Fortes et al. in [97]. There are examples of voltage waveforms, but this study was evaluated for frequencies up to the 25^{th} order of the fundamental harmonic only. Nevertheless, this study confirms the adverse impacts of switching large power electronics devices at a low voltage level on the voltage waveform at a medium voltage level of the power distribution system.

In order to follow up on the studies mentioned above, a model of a real part of a distribution grid with a large PV power plant was assembled in Matlab Simulink software. Results were subsequently used to set up experiments in this doctoral research. The numerical model and its results were partially published in [A1] and [A2].

3.2. Structure of Numerical Model

3.2.1. Photovoltaic Power Plant

The simulated PV power plant with a total installed power of 1 MW consists of four identical power units with a rated peak power of 250 kW. The model of the unit in the Simulink environment is shown in Fig. 47.

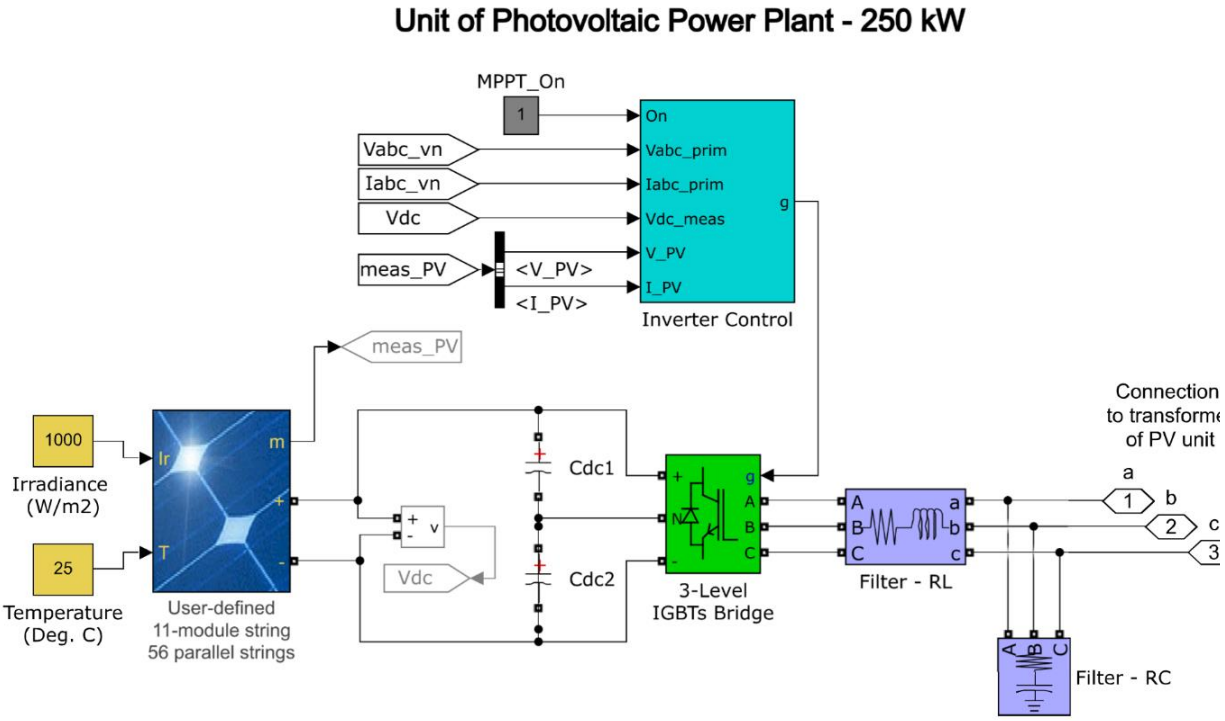

Fig. 47 Model of the 250-kW PV power plant unit; shown in the Simulink environment (Reproduced from [A2])

The guidelines for simulating the PV power systems by A. Yazdani et al. in [98] provide many recommendations that were respected in the model to provide as convincing results as possible. Regarding the power generation parameters, both irradiance (1000 W/m^2) and temperature (25 °C) of PV panels were set to constant values for all performed simulations. The converters of PV modules were considered as sources of high-frequency distortion. Controlled three-level IGBT inverter converted dc voltage of 770 V to ac voltage of 400 V. The switching frequency of IGBTs was set to 3 kHz (60th harmonic order). An output filter subsequently shaped the generated ac voltage. The filter consisted of a series inductance of 300 µH and a parallel capacitance of 500 µF. Parameters of the sinusoidal filter were selected to reach sufficient, low-cost filtering of produced power according to current power quality standards, such as EN 50160 [1], IEC 61000-3 series (especially IEC TR 61000-3-6 [2]), or IEEE Std. 519-2014 [3]. The power factor of each power plant unit was set to 0.95, which is in agreement with the common practice and related standards. Each PV power plant unit was connected by a unit transformer to the distribution network with a rated voltage of 22 kV, as shown in Fig. 47 and Fig. 49.

3.2.2. Unit Power Transformer

Each PV power plant unit was connected to a 22-kV network by a distribution power transformer with the following parameters: nominal apparent power of 250 kVA, primary/secondary side voltage 400 V/22 kV, and D1/Y connection of phase windings. The actual three-phase transformer was modeled as three single-phase units, whose equivalent circuits respected high-frequency behavior up to several tens of kilohertz, as shown in Fig. 48. This is a standard modeling method, which is explained, for example, by A. S. Alfuhaid in [99]. In comparison with the transformer models for power or low frequencies, the capacitance between windings C_p and capacitance between windings and ground (transformer tank) C_g had to be considered. These capacitances were estimated according to the procedure that was published by L. Dalessandro et al. in [100]. Resistance and inductance values in the equivalent circuit were calculated from the specifications in the datasheet of a real distribution transformer. The summary of all used parameters is given in Tab. 5.

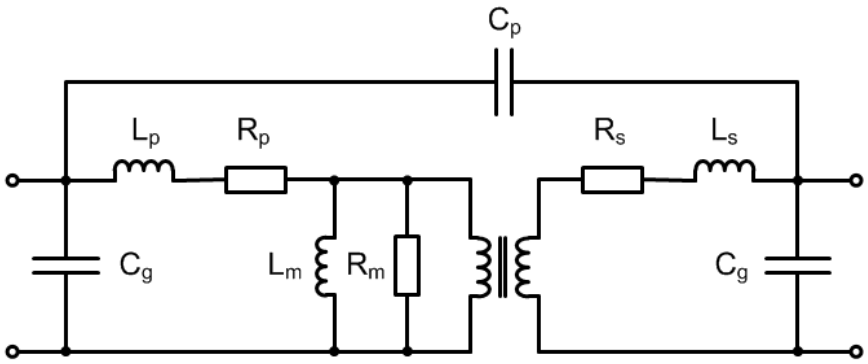

Fig. 48 The equivalent circuit of a single-phase transformer respecting high-frequency behavior (Reproduced from [A2])

Tab. 5 Parameters of the distribution transformer used in simulations (Adapted from [A2])

Distribution Transformer of Photovoltaic Power Plant Unit			
Datasheet spec. of real 3-phase transformer:		*Caculated parameters for 1-phase equivalent circuit:*	
Nominal apparent power	250 kVA	Primary winding resistance (MV) R_1	46 Ω
Primary voltage	400 V	Primary winding self-inductance (MV) L_1	270 mH
Secondary voltage	22 kV	Secondary winding resistance (LV) R_2	0.015 Ω
Short-circuit losses	3950 W	Secondary winding self-inductance (LV) L_2	0.09 mH
Short-circuit voltage	4.5 %	Mutual inductance L_m	75 H
No-load losses	770 W	Core equivalent resistance R_m	1885 kΩ
No-load current	0.3 %	Ground capacitance C_g	10 pF
Connection of phase windings	D1/Y	Capacitance between windings C_p	200 pF

3.2.3. Distribution Network

The power plant units with total self-consumption of 50 kW were connected to a common node (PCC) in the distribution network. The whole power plant was further interconnected to 110-kV upstream high voltage grid by a combination of cable and overhead lines that were terminated with a power transformer (10 MVA, 110 kV/22 kV, Yg/D1), as seen in Fig. 49.

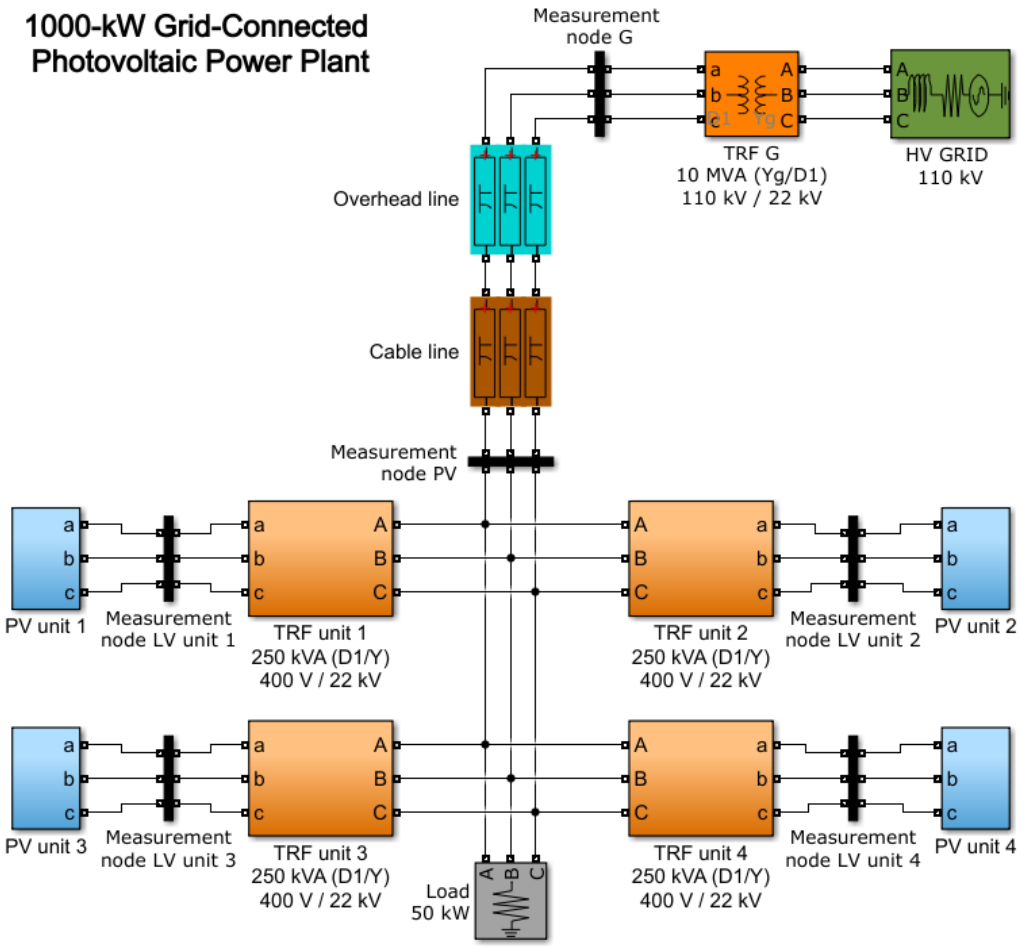

Fig. 49 Distribution network model with 1-MW PV power plant; shown in the Simulink environment (Reproduced from [A2])

A common practice in PV power plant designs is to connect the power plant with the nearest overhead line pole via a short cable junction. This practice was respected in the model. Both cable and overhead lines were modeled like a cascade of π equivalent circuits that represented the approximate model of distributed line parameters. The number of π equivalent circuits was determined for sufficient simulation up to a frequency of approximately 100 kHz. Each phase was simulated as a single-phase equivalent circuit due to the symmetrical power load and simplification of computational processes. The worst structure of the distribution network was simulated for the occurrence of high-frequency voltage distortion, where the PV power plant is installed at the end of a long power line branch. Another power load in this

Tab. 6 Parameters of the distribution network (Adapted from [A2])

Cable resistance	0.32	Ω/km
Cable inductance	0.4	mH/km
Cable capacitance	0.31	μF km
Overhead line resistance	0.24	Ω/km
Overhead line inductance	1.1	mH/km
Overhead line capacitance	4.5	nF/km
Transformer 10 MVA 120 kV/25 kV:		
Both winding resistances	0.003	pu
Both winding self-inductances	0.008	pu
Mutual inductance	500	pu
Core equivalent resistance	500	pu
Upstream grid 110 kV: X/R ratio	7	-

power line branch was assumed insignificant in comparison with the nominal power of the PV power plant (e.g., a small village is connected at the end of the power line branch). The parameters of both cable and overhead lines and the high voltage power transformer are summarized in Tab. 6. The short-circuit power of the high voltage grid and lengths of the lines were variable in the performed simulations.

3.3. Simulation Results

The phenomenon of high-frequency distortions in power systems should be more pronounced in power grids with relatively low short-circuit power. Therefore, the short-circuit power of the 110-kV upstream power grid was set to 100 MVA in initial simulations, representing the location of the 110-kV substation at the end of a long feeder. Lengths of cable and overhead lines were varied from 20 m to 1000 m and from 5 km to 50 km, respectively. The level of voltage distortions was evaluated by the voltage total harmonic distortion index (THD_V) that has given by expression (1). According to current power quality standards, the values of THD_{Vn} for $n = 40$ were determined and compared with those calculated for all harmonics up to the Nyquist frequency of the simulation (approx. 150 kHz). The resulting density charts showing THD_{V40} and THD_{Vall} in the PV node for different line lengths are shown in Fig. 50.

As can be seen in the density charts, a maximum THD_{V40} value of 8 % was determined for cable and overhead line lengths of approximately 20 m and 30 km, respectively. This value is consistent with the limits for medium voltage distribution networks in current power quality standards. However, if all harmonics are considered, then the THD_{Vall} value has reached almost 20 % for cable and overhead line lengths of approximately 20 m and 10 km, respectively. As is evident from the charts, an increased capacitance of the cable line (i.e., length) had a positive impact on the suppression of standard harmonics. However, impedance resonances of power systems may still cause an increase in magnitudes of high-frequency harmonics. The highest high-frequency resonances occur in combinations of relatively short cable and overhead lines up to a length of approximately 400 m and 30 km, respectively. Of course, it only applies to

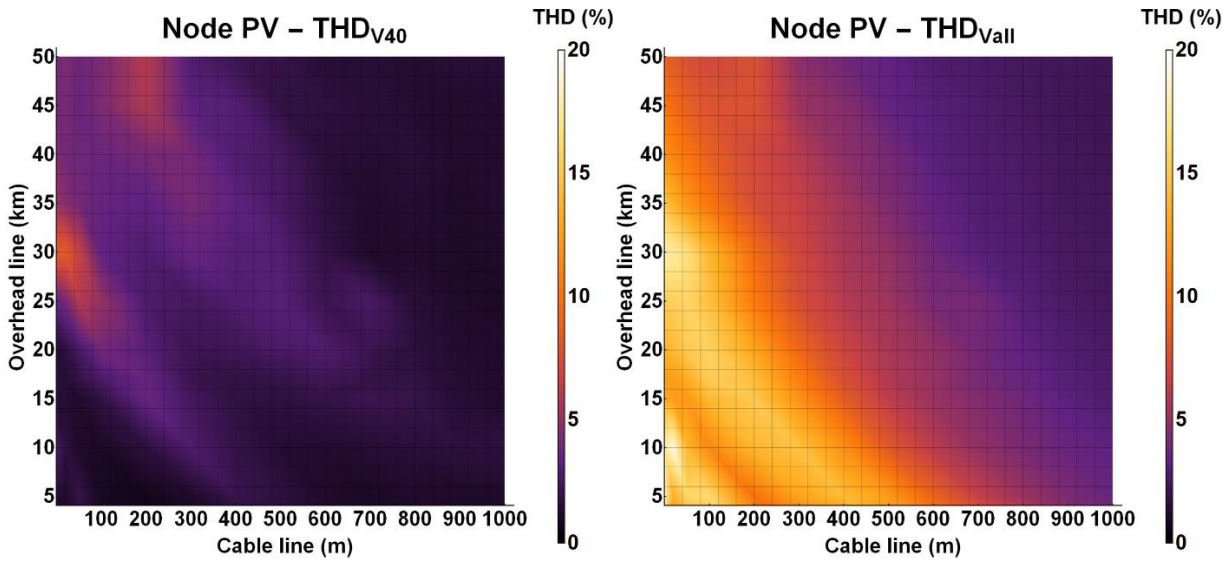

Fig. 50 Density charts for calculated THD_{V40} and THD_{Vall} in PV node for variable lengths of cable and overhead lines (short-circuit power of 110-kV upstream power grid was set to 100 MVA)

this specific structure of the modelled power grid, and the situation should be significantly different in other power systems. Based on density charts, four cases of the model structure were selected for detailed study:

- Case 1: cable line length of 20 m and overhead line length of 10 km
- Case 2: cable line length of 50 m and overhead line length of 30 km
- Case 3: cable line length of 100 m and overhead line length of 20 km
- Case 4: cable line length of 400 m and overhead line length of 5 km

All cases were simulated depending on the short-circuit power of the 110-kV upstream power grid in the range from 100 to 10000 MVA. From the simulations, voltage and current waveforms were recorded in PV and LV unit 1 nodes. Subsequently, frequency analyses and THD_V calculations were performed.

The highest THD_{V40} value of 8 % on the low voltage side of the PV plant unit was observed for Case 1 at a short-circuit power of 100 MVA of the 110-kV upstream power grid. This value is the maximum allowed according to the current power quality standards. When all harmonics were considered, a THD_{Vall} value of almost 33 % was evaluated. These values can be realistic in practice due to the very different quality of installed power converters and filters. Voltage and current waveforms and frequency spectrums of voltage are shown in Fig. 51. Frequency analysis of the voltage shows 5^{th} harmonic as dominant in the standard frequency range, which is typical for power converters. Dominant high-order frequencies were 3, 6, and 9 kHz, which corresponded to the switching frequency of the PV power plant converters. Other graphs for LV unit 1 node in Case 1 with different short-circuit power of the 110-kV upstream power grid are given in Appendix A.

High-order harmonics propagate though the power transformer from low voltage to the medium voltage level of the distribution network where are attenuated or amplified depending on impedances of the power grid. The example of voltage and current waveforms and

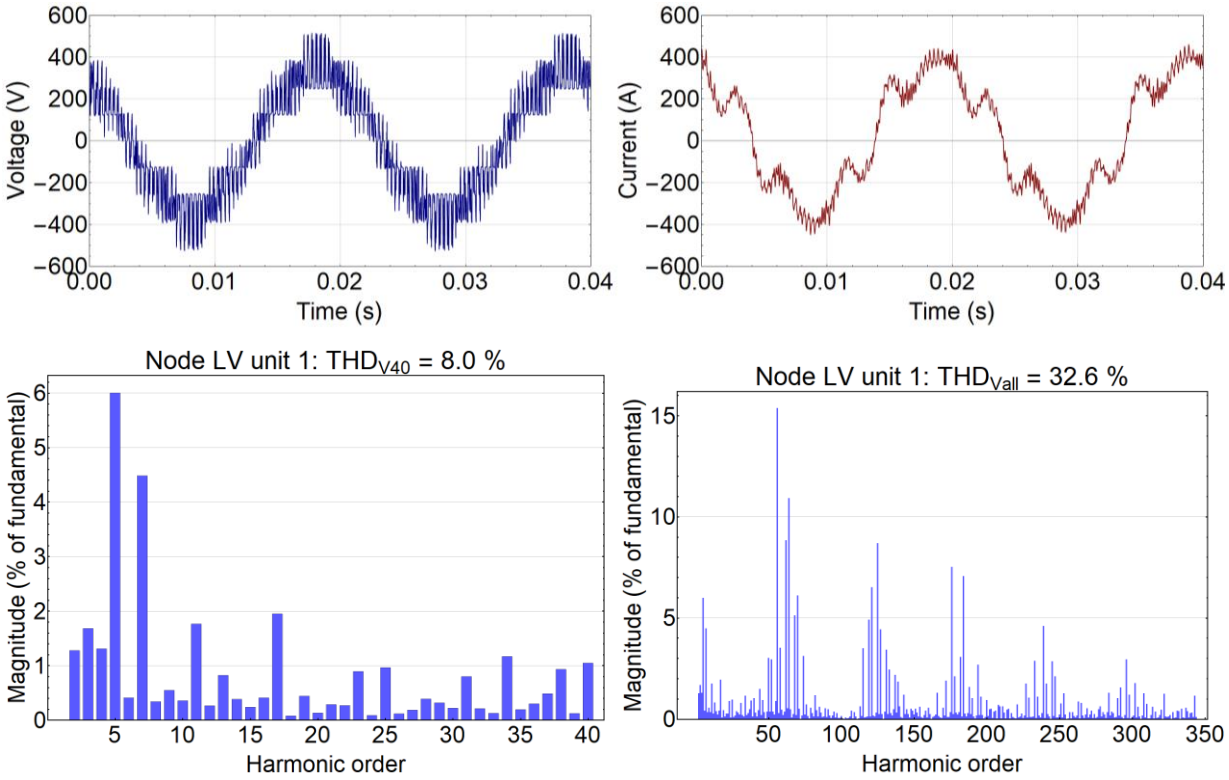

Fig. 51 Simulation results in the LV unit 1 node for 20-m cable and 10-km overhead line lengths and short-circuit power of 100 MVA of the 110-kV upstream power grid; ***On the top:*** *Voltage and current waveforms;* ***On the bottom:*** *Frequency spectrum of voltage up to 40th and 350th harmonic order with calculated THD_V values*

frequency analysis of the voltage in the PV node are shown in Fig. 52 for Case 1, where a short-circuit power of the 110-kV upstream power grid was set to 100 MVA. As can be seen in the graphs, significant resonances are superimposed on the sinusoidal power frequency voltage. The frequency spectrum of the voltage shows an acceptable distortion level in the standard frequency range, but on the other hand, significant harmonics occurred at higher harmonic orders. Resulting graphs for the four simulation cases are given in Appendix A. The results for all cases also include records at a short-circuit power of 100, 200, 1000, and 5000 MVA of the 110-kV upstream power grid. For different parameters of simulations, different high-order harmonics are dominant in a frequency range of 3 – 15 kHz that are usually directly multiples of 3 kHz or in their vicinity. When all harmonics were considered, a THD_{Vall} value of up to almost 18 % was evaluated for some cases in medium voltage electrical network.

As can be seen from the voltage waveforms that were simulated in the PV node, high-frequency harmonics can cause continuous overvoltages in power systems. The magnitude of overvoltages β is directly proportional to the amplitude of the highest voltage of the system, as shows from the following conventional expression:

$$\beta = \frac{V_p}{\frac{V_{max} \cdot \sqrt{2}}{\sqrt{3}}} \ (p.u.) \tag{21}$$

where V_p is the maximum peak value of the examined voltage, and V_{max} is the maximum line voltage of the power system (a value of 25 kV for 22-kV power systems). The overvoltage was determined for the four simulation cases depending on the short-circuit power of the 110-kV

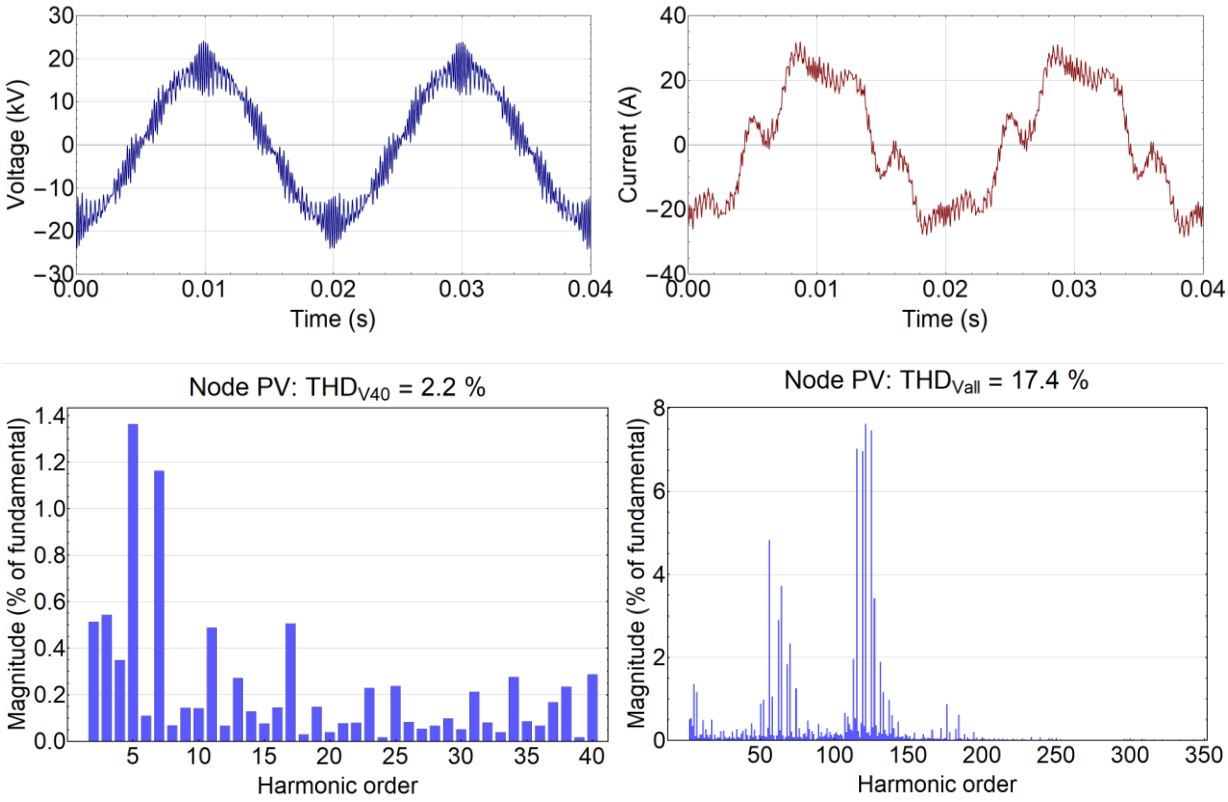

Fig. 52 Simulation results in the PV node for 20-m cable and 10-km overhead line lengths and short-circuit power of 100 MVA of the 110-kV upstream power grid; ***On the top:*** *Voltage and current waveforms;* ***On the bottom:*** *Frequency spectrum of voltage up to 40th and 350th harmonic order with calculated THD_V values*

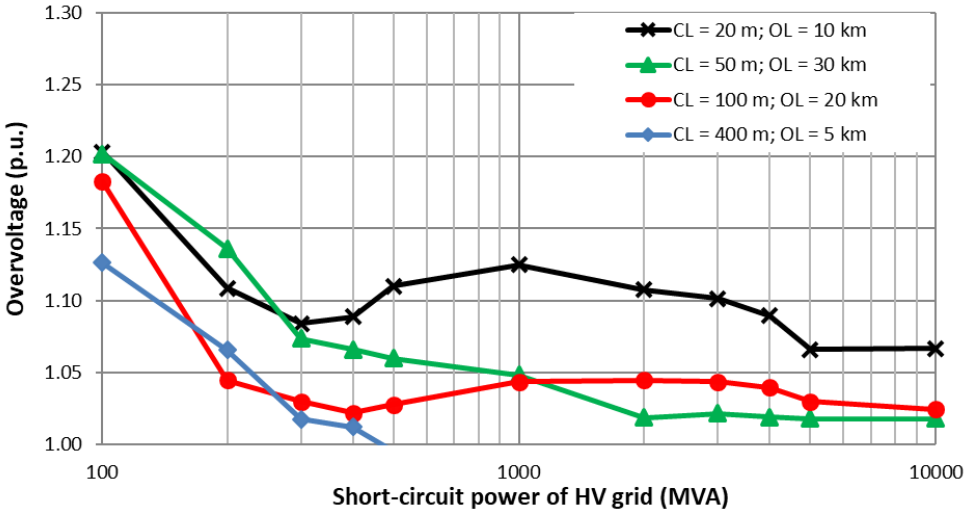

Fig. 53 Overvoltage dependence on the short-circuit power of the 110-kV upstream power grid for four different combinations of cable and overhead lines (CL – cable line, OL – overhead line)

upstream power grid, as shown in Fig. 53. The performed simulations showed that overvoltage might be up to 1.2 p.u. for small values of the short-circuit power. The determined high-frequency voltage distortions can permanently stress cable insulation systems with unexpected significant values of overvoltages. It may be a critical stress condition that could shorten their lifetime.

Observed possible shapes and values of high-frequency voltage distortion were used to set the voltage stresses in the following accelerated aging study of medium voltage cable systems. This numerical model should be used in the future as a basis for simulating more sophisticated electrical networks while respecting the phenomenon of high-frequency distortions. However, it is beyond the scope of this doctoral thesis.

4. TESTING SYSTEM FOR COMBINED STRESSES OF MEDIUM VOLTAGE INSULATIONS

4.1. Existing Systems for Combined Stresses of Insulations

The experimental focus of this thesis is accelerated aging under combined thermal and voltage stresses with superimposed high-frequency voltage distortion. The testing of samples of actual medium voltage cables under these conditions calls for a powerful and complex test site. Only a few previous works were focused on a similar experimental testing method. Their realization of test equipment is discussed below.

H. Suzuki et al. in [70] combined sinusoidal voltage of frequency of few kilohertz with the power frequency voltage by a series connection of power frequency transformer and high-frequency transformer with a ferrite core, as shown the diagram in Fig. 54. A bypass filter was used for high-frequency components on the power frequency transformer. This design looks solid; however, the realization was carried out only for insulation material samples, not for whole cable systems that typically have large capacitive loads. Heightened thermal stressing of the insulation system was not included, as well.

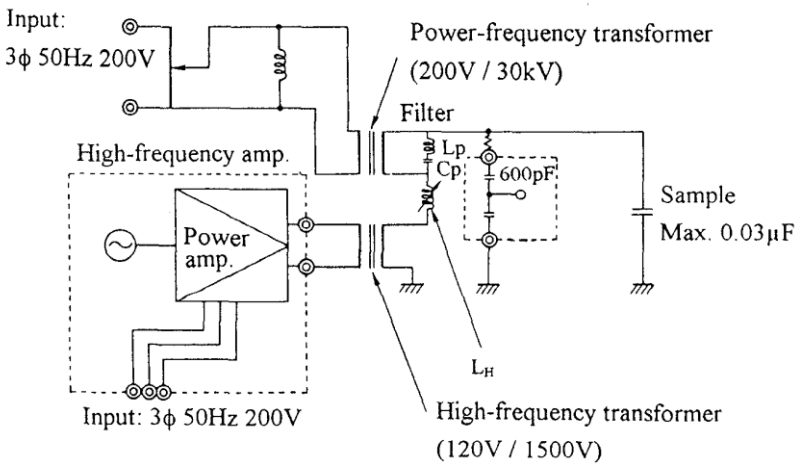

Fig. 54 Schematic diagram of combined voltage generator (Reproduced from [70])

Experimental aging of cables by L. Cao et al. in [93] was realized in the test site, whose schematic diagram is shown in Fig. 55. Tested cables were stressed by power frequency voltage with occasional superimposed switching impulses. The cables were kept at elevated temperature by high current flow, which simulated the real thermal distribution found in cable systems.

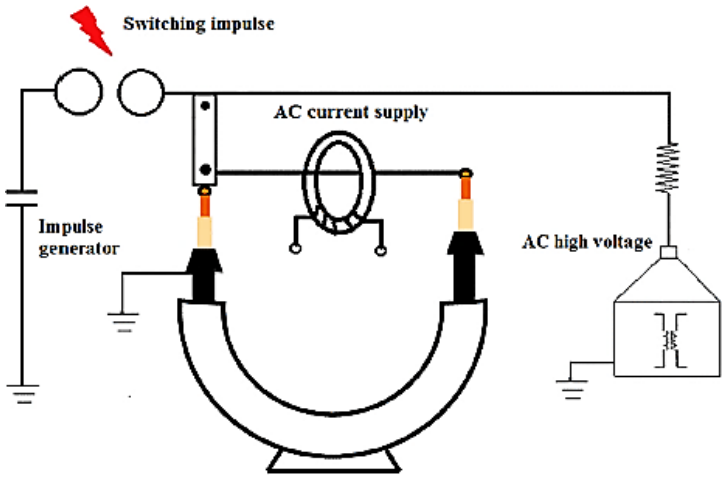

Fig. 55 Schematic diagram of the test site for combined aging of cables under superimposed switching impulses (Reproduced from [93])

An experimental station for testing of cable terminations under sinusoidal power frequency and superimposed sinusoidal high-frequency voltages was assembled by S. Banerjee and S. H. Jayaram in [56]. Its schematic diagram can be seen in Fig. 56. The test voltage was generated by the parallel connections of two voltage sources – a standard power frequency transformer and a high-frequency transformer with a ferrite core. Parameters of capacitors and inductors were based on numerical optimization of voltage source efficiency. Similar to the previous setup, the tested objects were thermally stressed by high current flow.

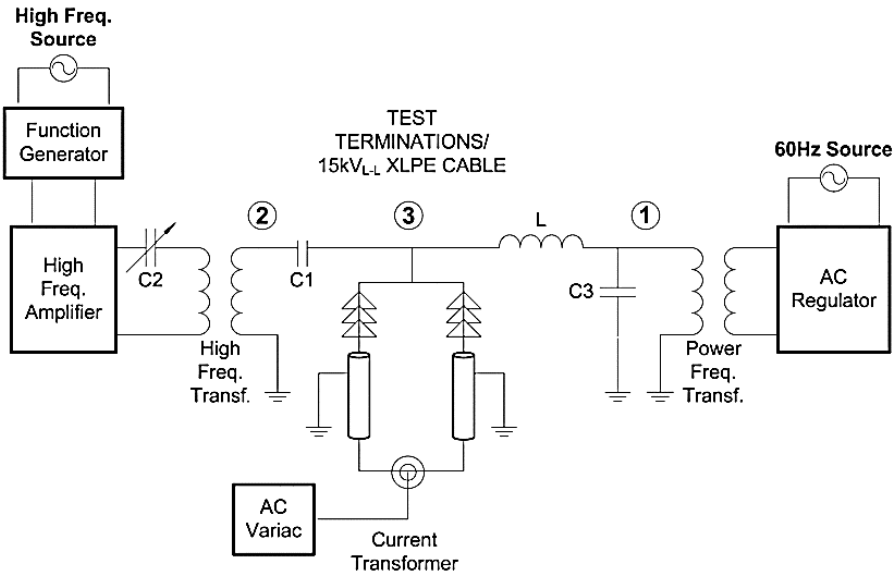

Fig. 56 Schematic diagram of combined thermal and voltage stresses with superimposed high-frequency voltage components (Reproduced from [56])

The experiments in this doctoral research required a more powerful and more variable test circuit. Thus, a specialized test site was developed. However, the design of the test circuit was based on the experience from the above studies.

4.2. Design of Testing System

4.2.1. Topology of Test Circuit

The preliminary proposal and the following realization of a universal test circuit for multi-stress aging with high-frequency voltage distortion were presented in [A7] and [A8], respectively. The design was based on two separate principal parts: a medium voltage circuit that can supply power frequency waveforms with superposed high-frequency distortions and a current loop that can simultaneously generate thermal stress on the tested objects. The use of separated sources is more effective and cheaper than the use of a single combined power source. A block diagram and the actual setup, realized in the High Voltage Laboratory of the Faculty of Electrical Engineering of CTU in Prague, are shown in Fig. 57 and Fig. 58, respectively.

The voltage source of the test system is realized as the series connection of two voltage transformers: a medium voltage test transformer 400 V/50 kV (VT1) and a high-frequency medium voltage transformer 120 V/10 kV (VT2). The power frequency test transformer is supplied from a controlled voltage source connected to the power grid. This transformer generates fundamental power frequency voltage stresses. As for the high-frequency

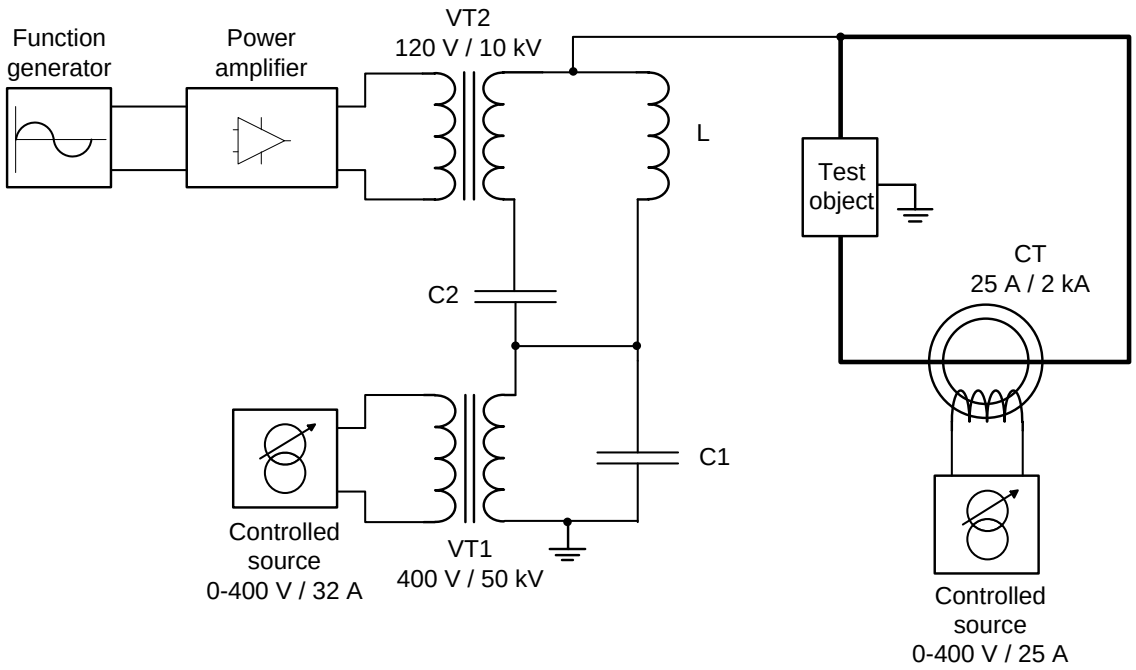

Fig. 57 The diagram of the assembled universal test system for accelerated aging of medium voltage insulation systems (Reproduced from [A7])

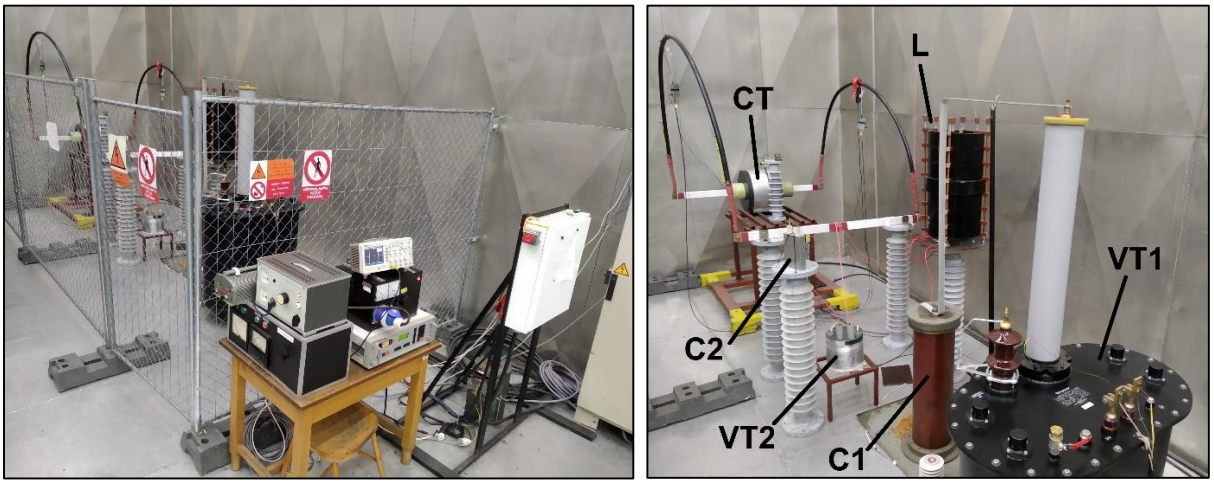

Fig. 58 The test system realized in the High Voltage Laboratory of the Faculty of Electrical Engineering, CTU in Prague

transformer, its magnetic core is made from nanocrystalline material with an operating frequency range of 3 to 100 kHz. The excitation of the high-frequency transformer is achieved by a function generator through a power amplifier. This setup enables the generation of various types of voltage distortions. Concerning the voltage operating range, the insulation between primary and secondary windings of the custom-ordered high-frequency transformer was designed to withstand the nominal voltage of 60 kV, respecting high-frequency voltage shapes.

Furthermore, the system also consists of a current loop, which can create elevated thermal stresses of the tested sample. The current loop consists of toroidal current transformer (CT) with an output of up to 2 kA (short-circuit), copper busbars, and active conductive part of a tested object (e.g., a core of tested cable sample). During the operation, the loop is closed by these components forming a one-turn secondary winding of the current transformer, which is supplied by a controlled source from the power grid. The insulation between primary and secondary windings of the custom-ordered current transformer was designed to withstand the nominal voltage of 60 kV, respecting high-frequency voltage shapes as well.

Some auxiliary passive components are used to increase the efficiency of the test circuit and to protect voltage transformers from saturation. The parameters of these components, i.e., capacitors C1 and C2 and inductor L, must be adjusted appropriately to suppress high-frequency voltage elements on the VT1 terminals, and the power frequency voltage elements on the VT2 terminals. Detailed descriptions, parameters, and pictures of all main parts of the test circuit are presented at the end of this thesis in Appendix B. All equipment of the test system was supplied from the test site switchboard that was specially constructed for this purpose. The circuit diagram of this switchboard is shown in Appendix C.

The realized test system enables the application of actual thermal and voltage stresses that can be used to test real complex samples of various medium voltage insulation systems. The functionality of the test system consisting of two voltage sources was verified in the related research project, in which oil-filled transformer insulation paper was tested in a similar manner (see [A5] and [A6]). The samples were stressed by a distorted voltage with a total peak

voltage of up to 10 kV. Voltage-time characteristics of the insulation were measured for sinusoidal voltage and for sinusoidal voltage with superimposed high-frequency oscillations.

4.2.2. Use of Transformer with Nanocrystalline Core

In comparison with the previously constructed and published similar test sites, the main innovation of this solution is the use of a high-frequency voltage transformer with a nanocrystalline magnetic core (VT2) that enables generation of voltage distortions in many shapes, ranging from high-frequency harmonics to repetitive fast impulses. The magnetic core of this type of transformer cannot be constructed from conventional silicone steels, because their permeability is sufficiently high only to a frequency of a few kilohertz. The material of the transformer core was chosen due to the beneficial properties of soft magnetic materials, which are suitable for such applications [101]-[104].

As is shown in Fig. 59, nanocrystalline materials have a stable high permeability at frequencies up to tens of kilohertz, which is a basic requirement for high-frequency applications. In addition to the superb permeability, nanocrystalline materials also have a high saturation polarization value, as can be seen in Fig. 60. These two parameters predestine the nanocrystalline material to be suitable for a magnetic core of a powerful source, which also retains a reasonable size. The reason for the latter is that the excellent magnetic properties of nanocrystalline materials reduce the required size of a transformer core, and the number of needed winding turns. Such reduction directly lowers the copper losses and winding capacitances and thus improves transformer performance at high frequencies. Other advantageous properties of nanocrystalline materials include low power losses, favorable temperature dependence, good long-term thermal stability, and even low price.

The other materials shown in the figures have certain shortcomings. Ferrites are one of the most popular materials for high-frequency applications due to frequency-stable permeability, relatively low cost, and low power losses. However, these materials are rather suitable for applications of lower powers and additionally have a strongly temperature-

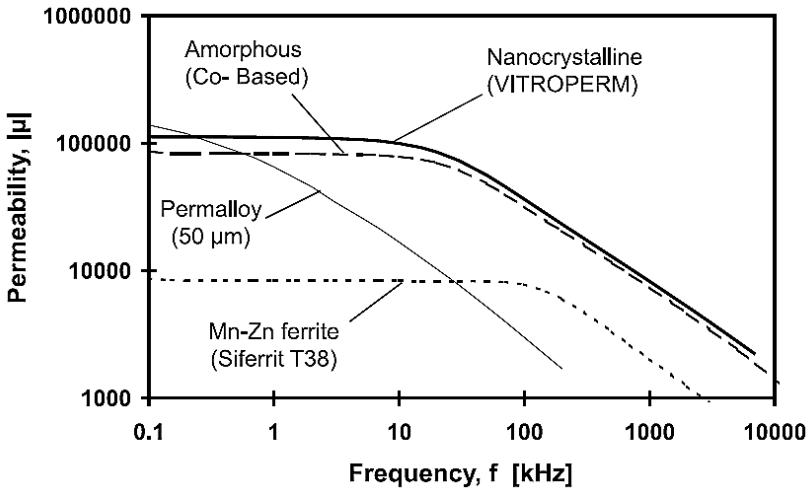

Fig. 59 Dependence of permeability on frequency for soft magnetic materials (Reproduced from [102])

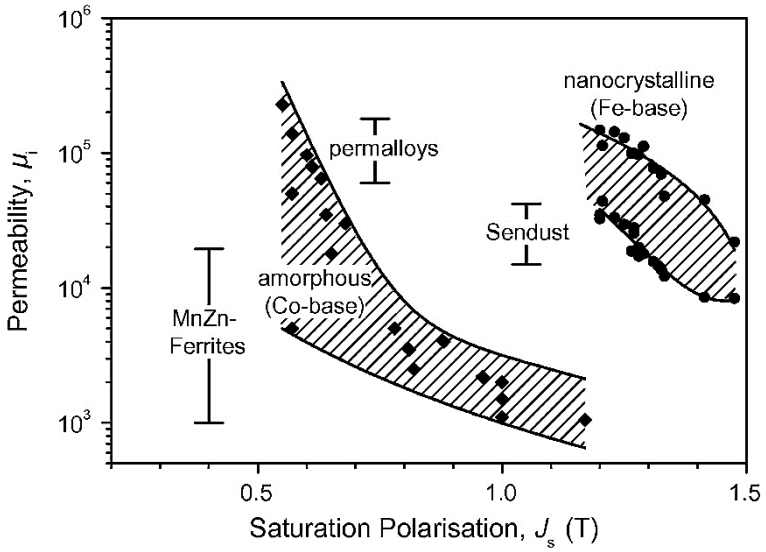

Fig. 60 Dependence of initial permeability on saturation polarization for soft magnetic materials (Reproduced from [101])

dependent permeability. Permalloys have excellent magnetic properties, but with significant dependence on temperature and mechanical stresses. Another disadvantage for the required application is the frequency dependence of permalloys' permeability, which is significantly stronger than the one of nanocrystalline materials. The frequency dependence of amorphous materials' magnetic properties is similar to nanocrystalline materials, and their production processes are analogous as well. On the other hand, due to the lower saturation polarization, more material and a larger magnetic core is needed to construct a transformer with similar parameters as the one with the nanocrystalline core. Therefore, even with similar production costs per kilogram, the amorphous magnetic core would turn out as the more expensive option. As is thus evident, the nanocrystalline magnetic core provides the best features for the design of high-frequency power transformers.

Transfer ratios were measured for instrument voltage transformer TUR 100 V/35 kV with a conventional magnetic core of silicon steel (IVT) and for a custom-ordered high-frequency voltage transformer with nanocrystalline magnetic core (VT2). The voltage on the primary side of the transformer V_1 and the voltage on the secondary side of the transformer V_2 were measured in the frequency range from 20 Hz to 200 kHz. The attenuation A was calculated according to the well-known formula:

$$A = 20\,log\left(\frac{V_2}{V_1}\right) \tag{22}$$

It was assumed that the test transformer should usually be loaded with very high impedances on the output, including a high content of capacitance (several meters of cable insulation between conductor and wire shielding). Therefore, the amplitude-frequency characteristics of measured transformers were determined for two states – without load and with a capacitive load of 2.5 nF representing the tested cable samples. The resulting characteristics are shown in Fig. 61.

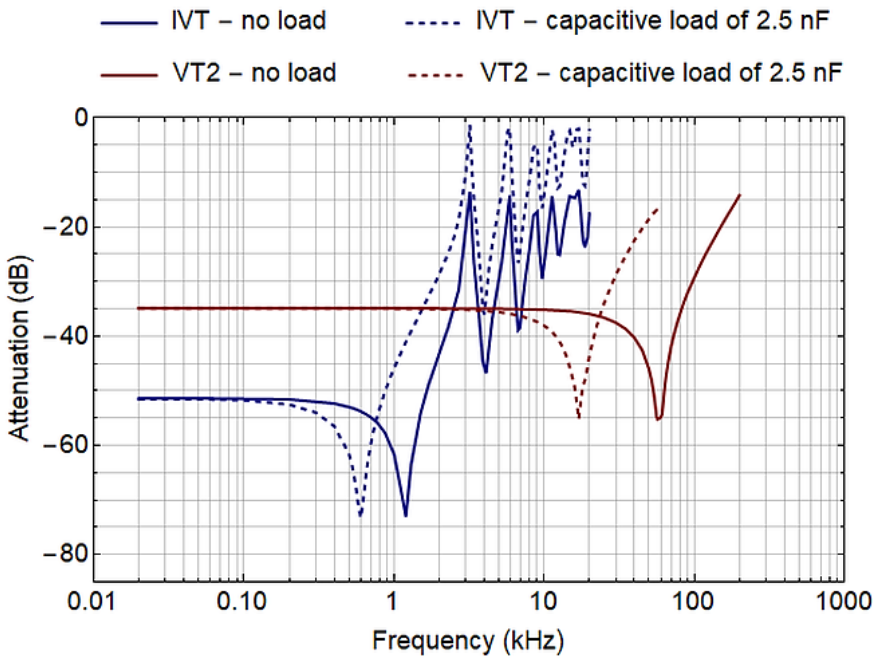

Fig. 61 Amplitude-frequency characteristic of instrument voltage transformer TUR 100 V/35 kV (IVT) and high-frequency medium voltage transformer 120 V/10 kV with the nanocrystalline core (VT2)

As can be seen from the results, the frequency limit of IVT is several kilohertz and decreases for a capacitive load. It demonstrates the impossibility of using conventional power transformers to generate the required high-frequency distortions effectively. The frequency limit of VT2 is over 100 kHz and several tens of kilohertz for non-load and capacitive load, respectively. This frequency range is sufficient for investigations of high-frequency distortions in power systems, which were described and analyzed in chapter 2 of this thesis.

4.2.3. Resulting Shapes of Possible Voltage Stresses

Waveforms of voltage stresses may be composed of power frequency voltage and high-frequency voltage with a variable frequency range between 3 to 100 kHz. The maximum effective value of output voltage is 50 kV for the power frequency component, and 10 kV for the high-frequency component. To provide an example, the output voltage was recorded for

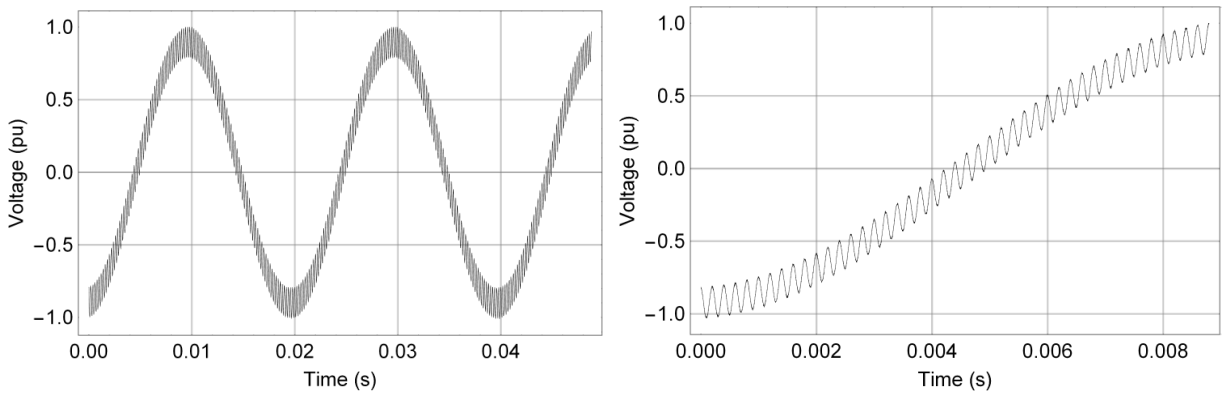

a) Power frequency voltage and superimposed sinusoidal voltage 5 kHz

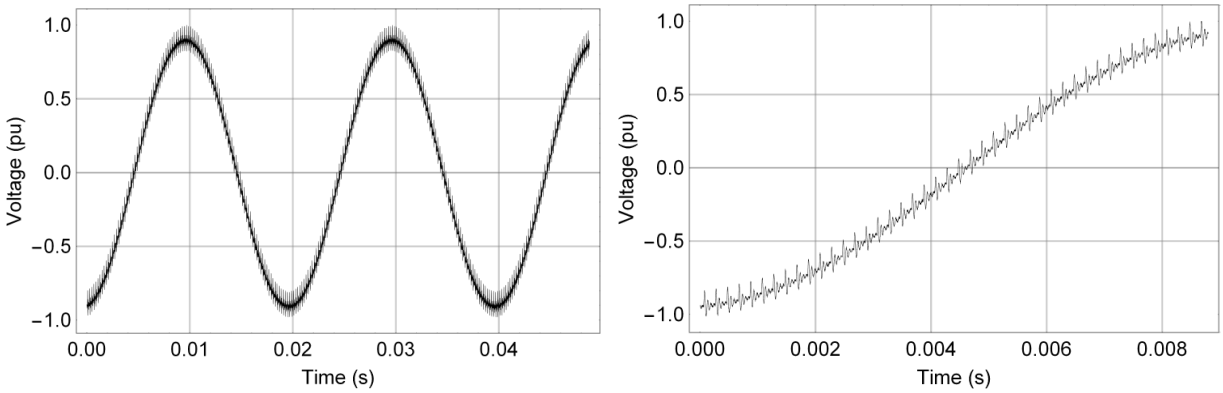

b) Power frequency voltage and superimposed damped sinusoidal voltage 16 kHz with a repetition frequency of 5 kHz

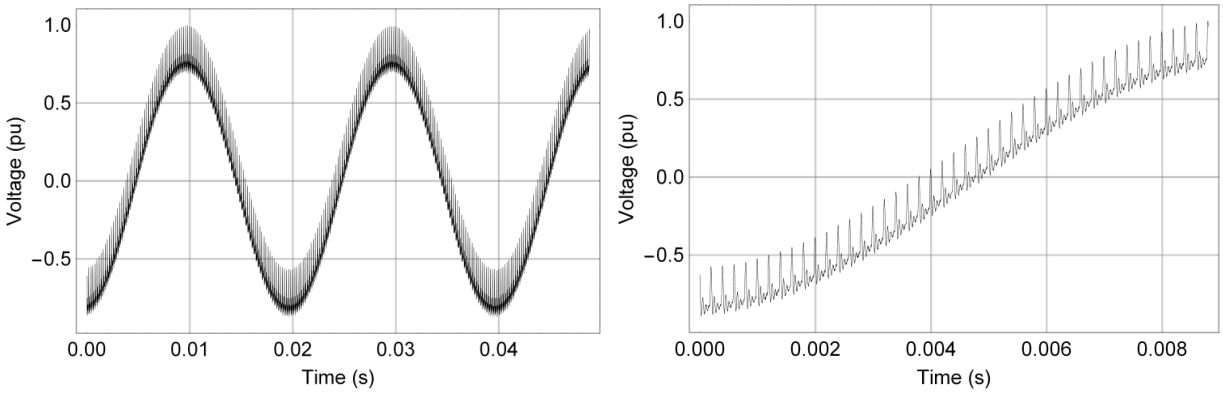

c) Power frequency voltage and superimposed voltage impulses with straight rise and exponential fall and repetition frequency of 5 kHz

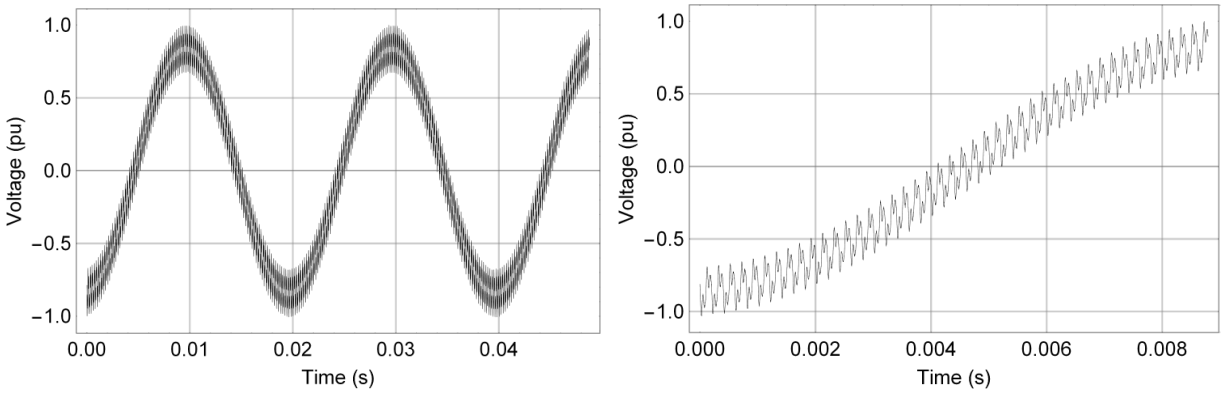

d) Power frequency voltage and superimposed rectangular voltage 5 kHz

Fig. 62 The example of some possible waveform shapes of distorted voltages that can be generated by the test system (Reproduced from [A7])

four different shapes of voltage distortions – sinusoidal high-frequency voltage, repetitive damped sinusoidal voltage impulses, repetitive voltage impulses with straight rise and exponential fall, and rectangular voltage with a spatial width of 50 %. The obtained waveforms are shown in Fig. 62.

The records from verification measurements of different voltage shapes show the variability of the test site in generating voltage stresses. It is beneficial for many other purposes that go beyond the scope of this doctoral research.

4.3. Measurement and Monitoring Equipment in Test Circuit

Voltage stresses are measured during the operation by capacitive voltage divider HIGHVOLT 0.3 nF, 100 kV that was originally designed for partial discharge measurements. The nominal voltage and wide frequency range of the divider are sufficient for reliable measurement of voltages with high-frequency distortions.

The current flow is measured by passive current clamp sensor Chauvin Arnoux C173 with a measurement range of 1 to 1000 A. The sensor is supposed to be placed in the insulated part of the current loop. In this experimental study, that part was represented by the body of the tested cable samples.

Leakage currents of the tested objects, which are identical to the currents generated by the voltage sources, are measured by shunts with the following nominal parameters: resistance of 19.7 Ω and maximal current of 0.5 A. Each shunt consists of five parallel-connected resistors and a voltage output (BNC connector) that includes overload protection. The picture of the realized shunts is shown in Fig. 63, and the detailed circuit diagram is shown at the end of this thesis in Appendix C.

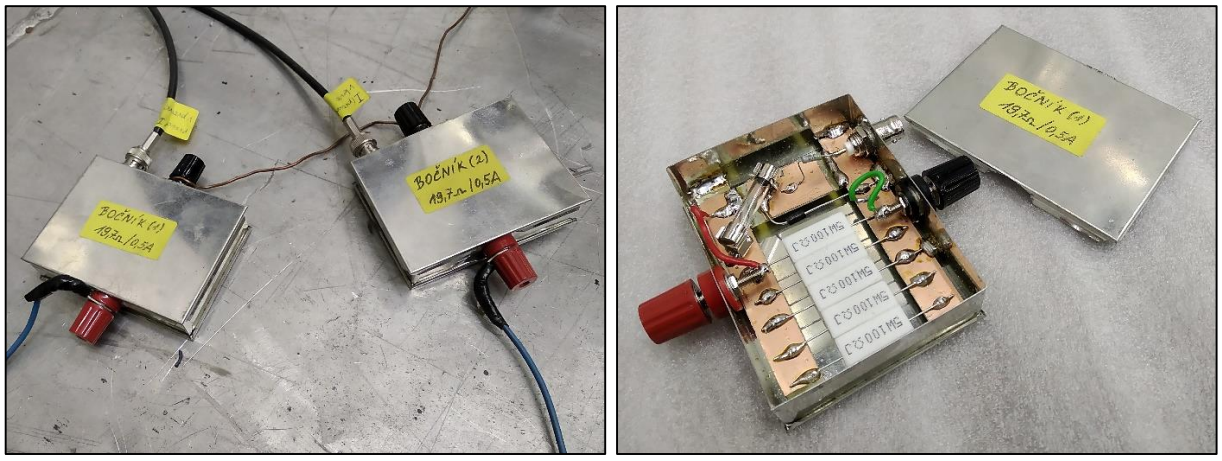

Fig. 63 Realized shunts for measurement of leakage current

Surface temperatures of tested objects are monitored by specialized temperature sensors that are based on the sensor component SMT172. This sensor produces a PWM signal with a variable pulse width that depends on the sensed temperature. The output signal from the sensor is measured by a monitoring system and subsequently processed by a microprocessor. The operating range of the sensor is - 45 to + 130 °C.

The sensor equipment consists of two sensor units and a communication unit. The sensor units can be supplied by voltage induction into the supply coil, causing a high current flow or directly via an adapter from the power grid. The sensor units are connected to the communication unit by optical fibers. This nonconductive connection with the former option of sensor power supply allows measurements of temperature directly on high voltage conductive parts. The communication unit only transforms input optical signals into output voltage signals (BNC connectors). Pictures of the constructed temperature measurement equipment are shown in Fig. 64 and detailed circuit diagrams of both sensor and communication units are shown at the end of this thesis in Appendix C.

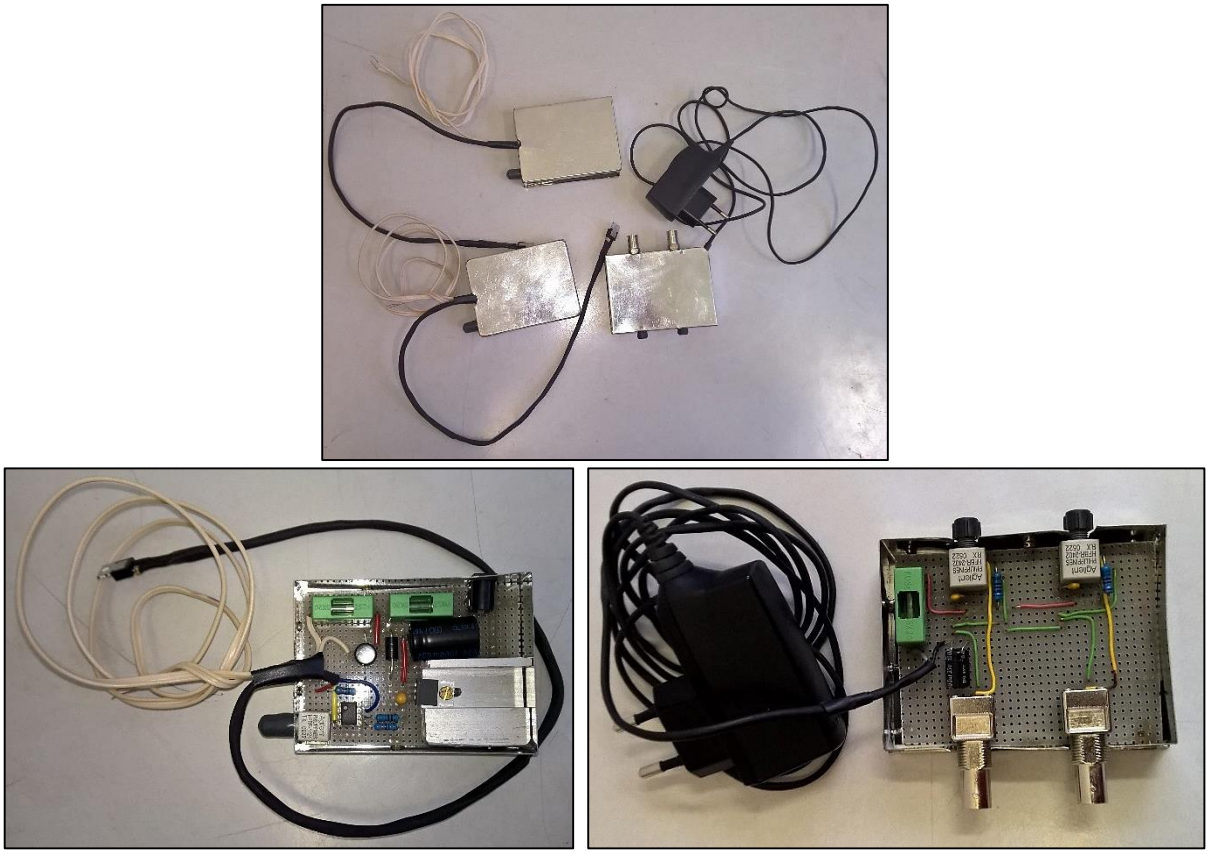

Fig. 64 Realized temperature sensors for surface temperature monitoring of tested objects; ***On the left:*** *Sensor unit;* ***On the right:*** *Communication unit*

All the above-mentioned measured parameters are continuously monitored and recorded during the test operations. The specialized monitoring device has been designed and assembled specifically for this purpose. Its block diagram and realization are shown in Fig. 65 and Fig. 66, respectively. The monitoring is controlled by Raspberry Pi microprocessor that is connected to a small BitScope USB oscilloscope. The microprocessor subsequently switches measurement outputs (BNC connectors) to the oscilloscope inputs in pre-defined time intervals and reads measured data. Afterward, the data are automatically processed and recorded into datalogger for online verification of the test conditions.

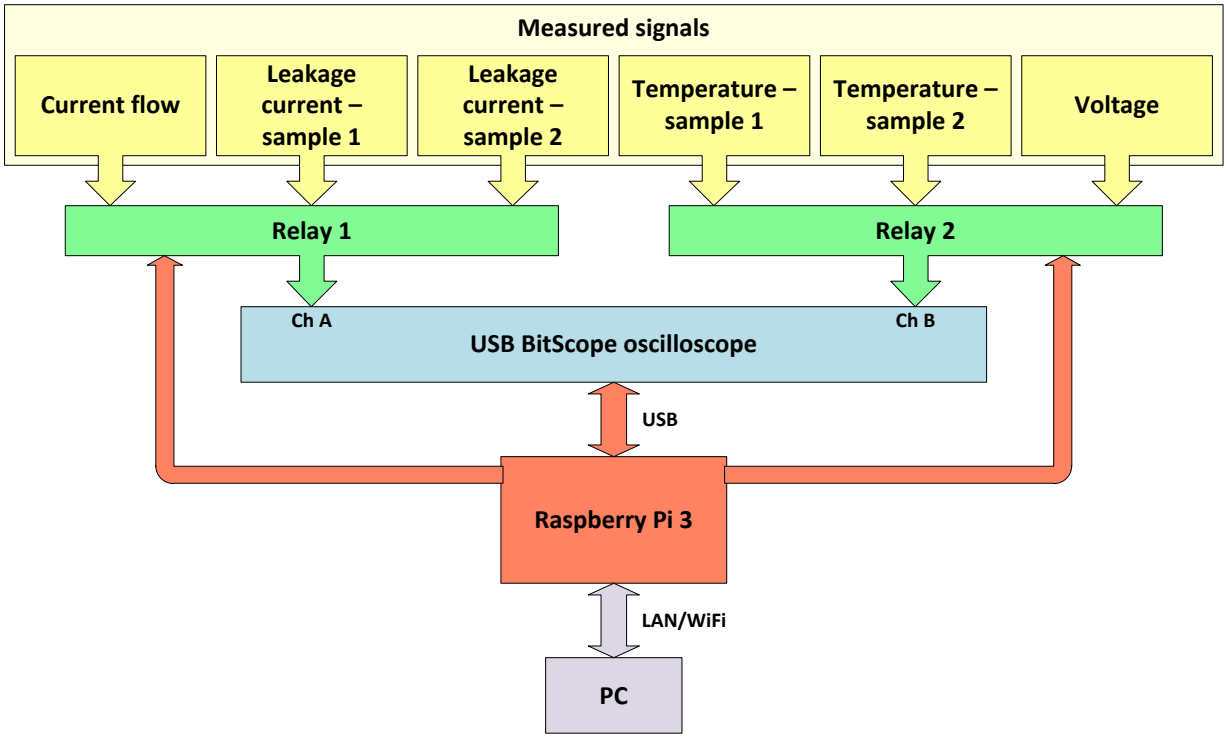

Fig. 65 Block diagram of the monitoring system

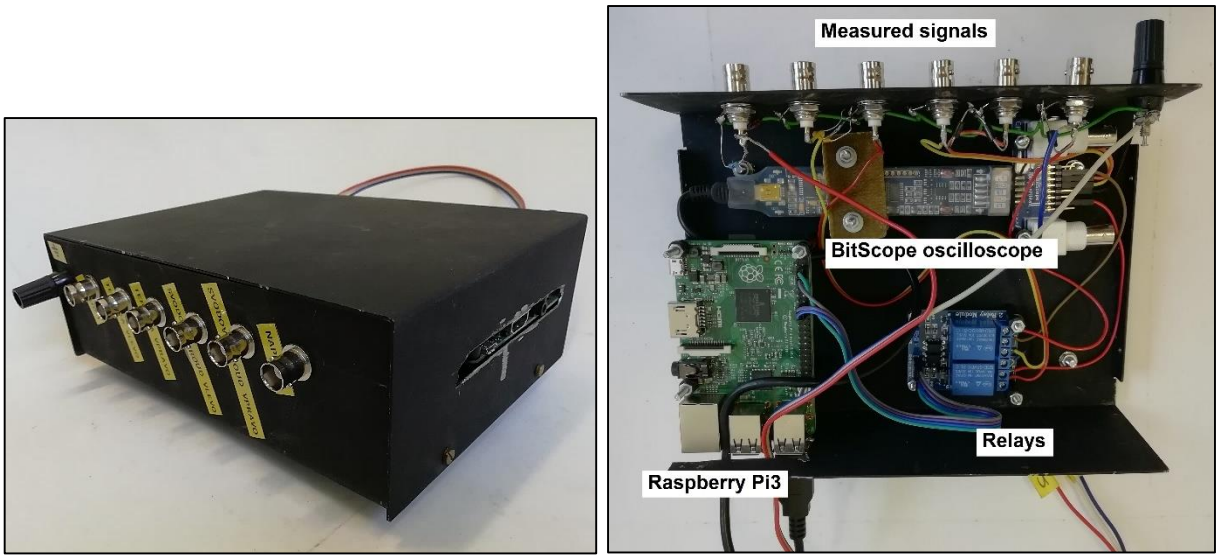

Fig. 66 Realized specialized monitoring device

5. EXPERIMENTAL PROCEDURES FOR ACCELERATED AGING TESTS OF MEDIUM VOLTAGE CABLE SYSTEMS

5.1. Samples of Medium Voltage Cable System

All tested samples were prepared from identical common medium voltage shielded single-core cables with XLPE insulation and core cross-section of 150 mm^2 (referred to as type NA2XS2Y 1x150RE/16 12/20 or 22-AXEKCE 1x150RE/16). The rated voltage of the tested cable system was 22 kV (in the Czech Republic, most cable systems in the electrical distribution network are used at a voltage level of 22 kV or 35 kV). Each cable sample was 3 m

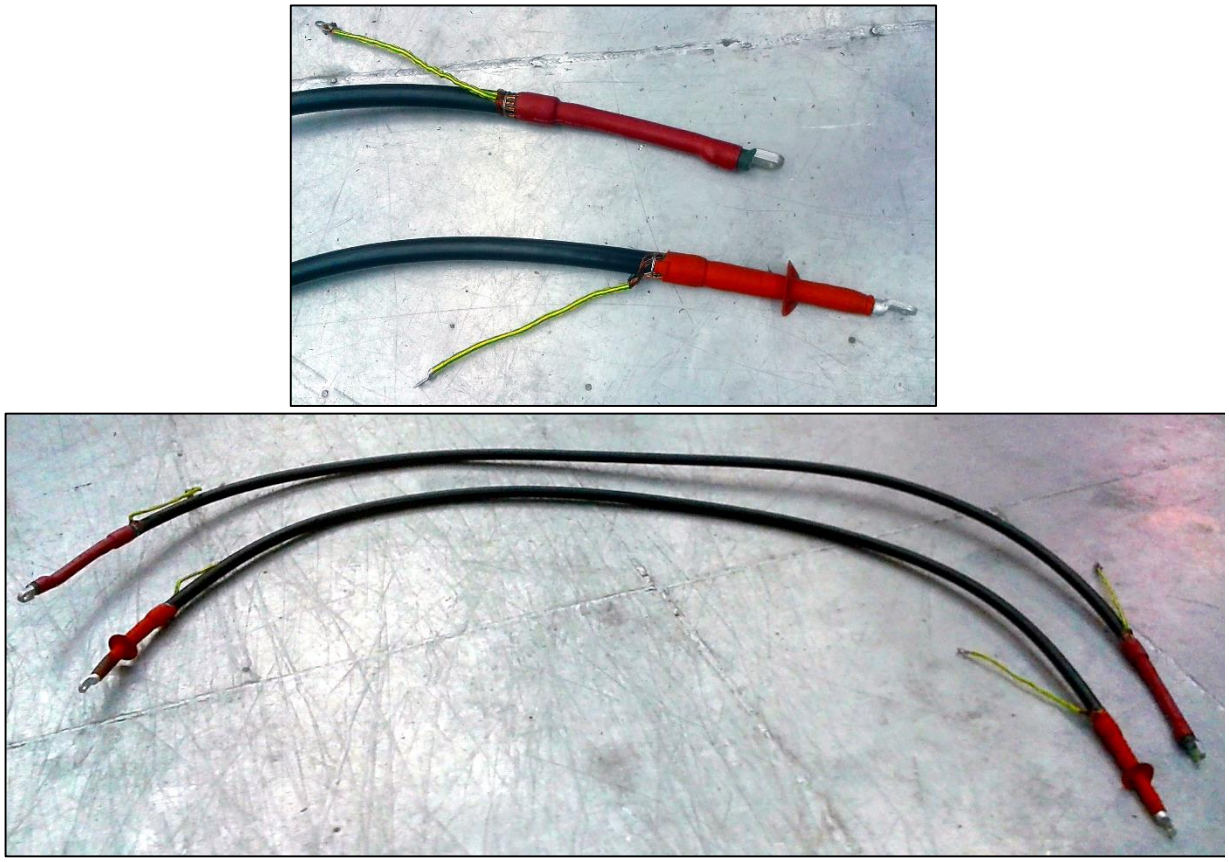

Fig. 67 Prepared cable samples for accelerated aging tests

long and was equipped with the same type of cable terminations on both sides. The two most common types of cable termination were used: heat-shrink cable termination with non-linear stress grading and elastomeric (slip-over applied) cable termination with non-linear stress grading. The employed types of cable terminations were chosen in the variant for indoor use with the same nominal voltage as the one of the cables. All terminations were mounted in laboratory conditions by an experienced specialist. An example of cable system samples with both types of cable terminations is shown in Fig. 67.

5.2. Voltage Stresses

The cable samples were exposed to increased voltage stresses, as is common in accelerated aging tests [105]-[108]. The power frequency test voltage between the cable core and the shielding was three times higher than the nominal voltage (12.7 kV), i.e., test voltage of 38.1 kV. The high-frequency voltage distortion was based on the results of the numerical model presented in Chapter 3 and the findings summarized in subchapter 2.1. Damped sine wave impulses with a natural frequency of 7.2 kHz and a repetition frequency of 800 Hz were superimposed to the power frequency voltage. The peak-to-peak voltage of the impulses was set to 15 % of the power frequency peak-to-peak voltage. The resulting test voltage waveform is shown in Fig. 68.

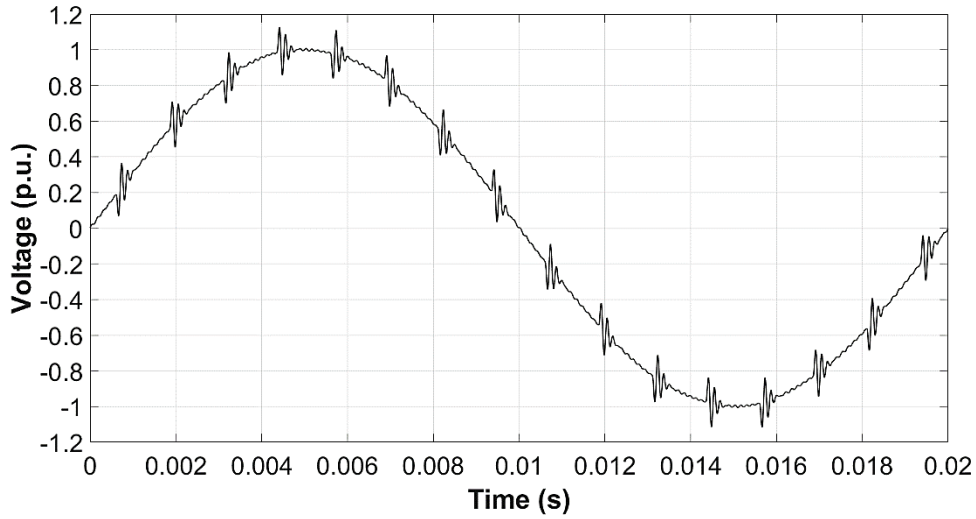

Fig. 68 Test voltage waveform for accelerated aging tests (Reproduced from [A1])

5.3. Thermal Stress

Continuous thermal stress was applied to accelerate the aging processes in the insulation of the tested cable samples, as is also common in accelerated aging tests [105]-[108]. The heat was generated by a high current flow through the cable core. The temperature of the cable core was maintained at 90 °C, which is the maximum allowed temperature given by the technical

specifications of the cable. Since the temperature would be the highest in the cable core, and since the temperature sensors could only be placed externally, a calibration of the measurement was required. This calibration process, described in IEC 61442 standard [109], was performed on one cable sample by placing temperature sensors on its jacket surface and core surface via holes drilled through the insulation system. In this manner, the ratio between core and jacket surface temperature at steady state was obtained. Calibration results are shown in Fig. 69.

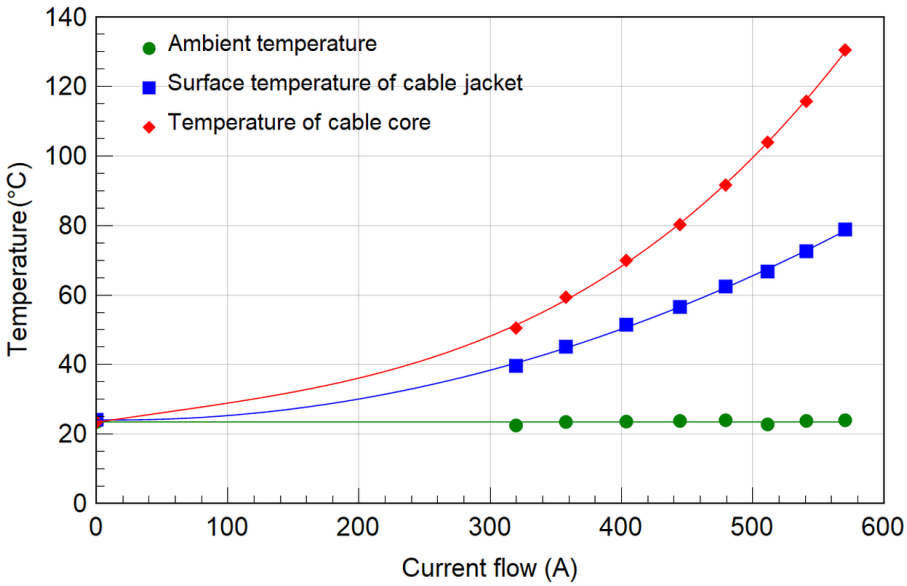

Fig. 69 Results of calibration measurement for a core temperature of tested cable samples

The gathered dependences from the calibration measurement show temperature ratios for different current flows. For the following experiments, it was found that the cable core temperature of 90 °C corresponds to a current flow of 480 A and a cable jacket temperature of 62 °C.

5.4. Summary of Test Setup for Individual Cable Samples

Cable samples were divided into three groups to determine the influence of high-frequency distortions on the cable insulation system. Cables in the first group were stressed by power frequency voltage only, the ones in the second group were stressed by power frequency voltage with superposed high-frequency distortions, whereas the cables in the third group were not stressed at all. All cable samples from the first and second groups were stressed for 24 weeks. All the parameters and conditions of the accelerated aging process of the cable samples are summarized in Tab. 7.

Some diagnostic methods and condition monitoring were applied during and after the tests to determine the effect of high-frequency distortions on the cable insulation system. Every three weeks of the aging test, the tested samples were removed from the test site to perform

Tab. 7 Parameters and conditions of accelerated aging tests for individual cable samples (Adapted from [A1])

Cable sample	Aging test	Temperature of core	Voltage 50 Hz	High-frequency voltage distortion
T1	Yes	90 °C	3x U_0	Yes
T2	Yes	90 °C	3x U_0	Yes
T3	Yes	90 °C	3x U_0	Yes
T4	Yes	90 °C	3x U_0	No
T5	Yes	90 °C	3x U_0	No
T6	Yes	90 °C	3x U_0	No
T7	No	x	x	x
T8	No	x	x	x
T9	No	x	x	x
C1	Yes	90 °C	3x U_0	Yes
C2	Yes	90 °C	3x U_0	No
C3	No	x	x	x
C4	No	x	x	x
Note: T samples - cable samples with heat-shrink cable terminations *C samples - cable samples with elastomeric cable terminations*				

partial discharge measurements on them. Dissipation factor measurements were carried out before and after the aging process. All samples that did not fail during the aging process, as well as samples that were not aged, were subsequently subjected to voltage breakdown tests. During the aging tests, the leakage current of each tested cable sample was monitored as well. The results of diagnostic measurements and condition monitoring are the subject of the following chapter and were extensively published in [A1].

6. RESULTS OF ACCELERATED AGING TESTS OF MEDIUM VOLTAGE CABLE SYSTEMS

6.1. Breakdown Voltage

Breakdown voltage test is the basic, straightforward measurement procedure for evaluating the quality and condition of insulation systems. The voltage applied between insulation system electrodes (between cable core and wiring shield in this study) is being increased gradually until a breakdown occurs (progressive voltage breakdown test). There are two main methods: the short-time method with continuous voltage stress increasing and the step-by-step method with step voltage stress increasing. The step-by-step method was chosen to evaluate cable samples after aging tests in this study. In this method, the voltage is being increased with a prescribed voltage ramp rate with constant voltage step size (normally 10 % of

Fig. 70 Setup of the breakdown voltage test

the initial voltage). Subsequently, the achieved voltage level is sustained for a certain period called dwelling time. The process is then repeated until a breakdown occurs.

Two cable samples stressed by a power frequency voltage with superimposed high-frequency distortion (samples T1 and T2) broke during their accelerated aging tests. The failure of cable sample T1 occurred in the 20th week, and the failure of cable sample T2 happened in the 17th week. The rest of the aged samples (T3-T6, C1, and C2), as well as a group of the unaged samples (T7-T9, C3, and C4), were subjected to a progressive voltage breakdown test. The test parameters of used step-by-step method were voltage step of 4 kV, dwelling time of 20 s, and initial voltage of 40 kV, which roughly corresponded to the applied voltage stress during the aging tests. Both terminations of each cable sample had to be immersed in oil during the breakdown test to prevent surface discharges. The attachment of cable samples and immersion of the cable terminations in oil-filled tubes during the breakdown tests is shown in Fig. 70.

As can be seen from the gathered results summarized in Tab. 8, the breakdown voltage for unaged cable samples with heat-shrink terminations (T samples) differs in comparison with unaged cable samples with elastomeric cable terminations (C samples). The breakdown voltage is 108 kV for unaged cable samples with heat-shrink cable terminations and 92 kV for those with elastomeric cable terminations. The samples aged with power frequency stress (T4-T6) reached the same breakdown voltage as the unaged samples of the same type. Sample T3, which was aged by power frequency voltage with superimposed high-frequency distortions, reached a slightly lower breakdown voltage of 104 kV. On the other hand, sample C1, which

Tab. 8 Breakdown voltages of cable samples after aging tests (Adapted from [A1])

Cable sample	**Aging test**	**Aging time (days)**	**Breakdown tests: breakdown voltage (kV)**
T1	PF + HF	139	x
T2	PF + HF	112	x
T3	PF + HF	168	104
T4	PF	168	108
T5	PF	168	108
T6	PF	168	108
T7	No	x	108
T8	No	x	112
T9	No	x	108
C1	PF + HF	168	92
C2	PF	168	92
C3	No	x	92
C4	No	x	92

Note: T samples - cable samples with heat-shrink cable terminations
C samples - cable samples with elastomeric cable terminations
PF = power frequency voltage
HF = high frequency voltage distortion

was aged by composite voltage stress as well, reached the same breakdown voltage as other samples of the same type (C2-C4).

X-Ray scans were performed in the heat-shrink cable termination areas, where the breakdown occurred, as is shown in Fig. 71. These scans show that the breakdown discharge path for samples T1 and T2 led directly from the end of shielding wires though the XLPE insulation to the cable core. In terminations of samples T4-T9, breakdown discharges propagated from the end of shielding wires to the cable lug. The ultimate discharges led through the non-linear stress-grading material layer (ZnO), which is placed between the XLPE insulation and the polymeric jacket, as is seen in Fig. 72. The termination of the sample T3 was broken down by a combination of both previously described processes. Although the XLPE insulation material was broken down and the discharge reached the cable core, it first

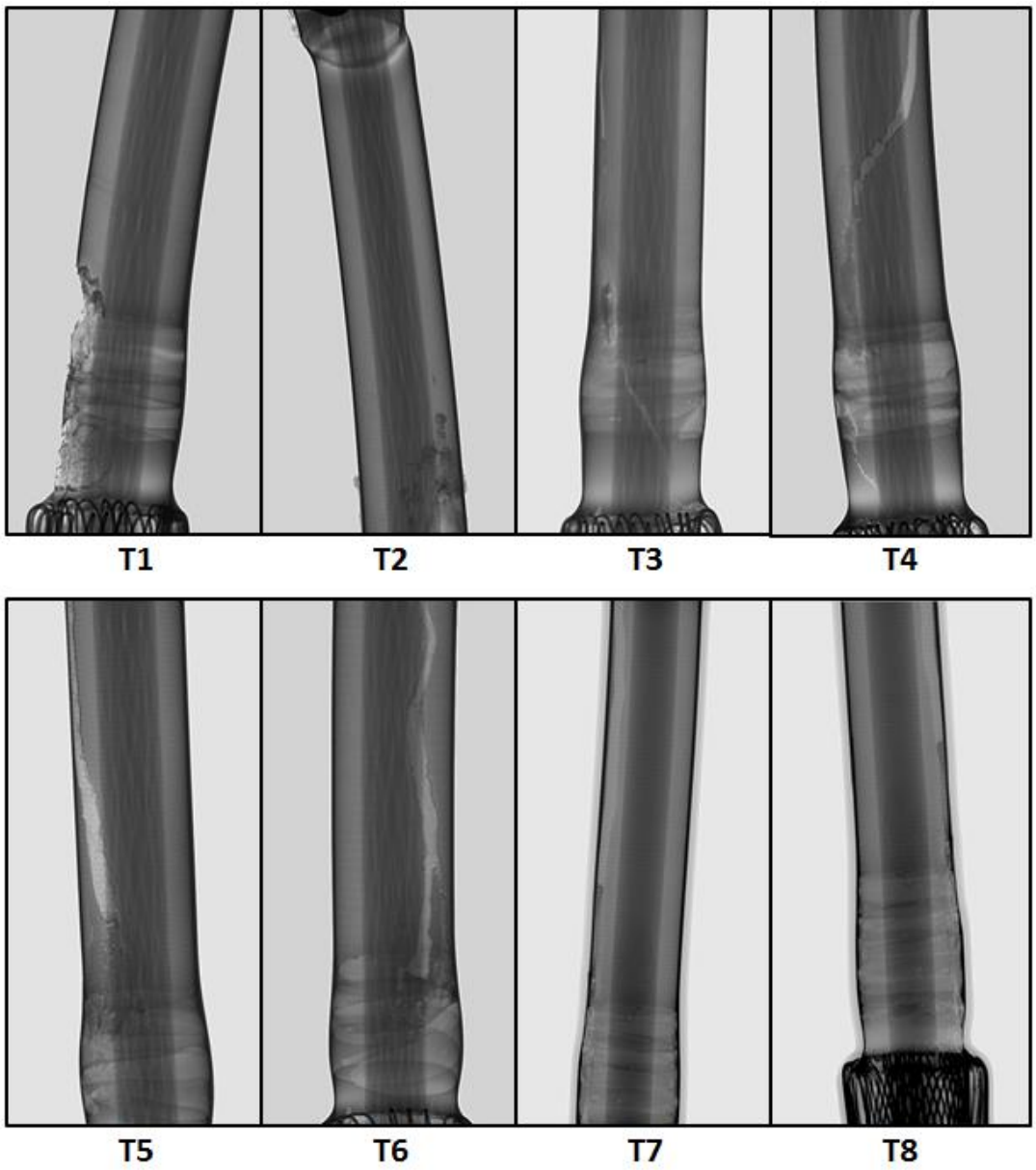

Fig. 71 Cable termination X-ray scans showing breakdown paths (created by TESTIMA X-Test equipment) (Reproduced from [A1])

Fig. 72 Breakdown path from wire screen to cable lug thought stress-grading material layer – the typical situation for samples T4-T9 (Reproduced from [A1])

propagated through the stress-grading material, and hence was not direct as in the case of T1 and T2. The reason may be that samples T1 and T2 were broken during the aging tests, but T3 was broken during the breakdown test after aging tests.

6.2. Partial Discharges

Partial discharge (PD) measurement is an essential diagnostic tool for solid insulation systems. For each cable sample, the dependence of discharge activity and apparent charge on applied voltage was measured every three weeks. The samples were removed from the accelerated aging test circuit and were connected to a special discharge-free transformer ČKD Praha 120 kV/10 kVA, as can be seen in Fig. 73. For PD measurements, an OMICRON

Fig. 73 Setup of partial discharge measurements

MPD 600 system with a coupling capacitor 100 kV/1 nF was used. Before PD measurements, the tested samples were always allowed to cool down to ambient laboratory temperature to prevent the measurement from being affected by temperature changes. At the start of a measurement, the initial value of the applied voltage was set to 40 kV in all cases. After a 1-minute PD measurement, this voltage was gradually lowered by 5 kV, and the PD measurement was carried out for each lower voltage level. The parameters of PDs were recorded three times for all voltage levels, and the average values were evaluated. The dependences of the apparent charge on applied voltage are shown in Fig. 74 and Fig. 75.

Because gradual erosion of material via PD activity can increase the size of voids, and thus the inception voltage of discharges in these individual voids is increased as well, it is beneficial to observe the development trends at the highest measured voltage, i.e., at 40 kV. As can be seen from the graph visualization of results, the apparent charge generally increased over time. However, there were some additional processes that caused decreasing of apparent charge of some samples during the first few weeks. This phenomenon was observed during the first three weeks for samples T3, T4, and T6, and during the first eighteen weeks for samples C1 and C2.

At the beginning of aging processes, the values of apparent charge of samples T3, T4, and T6 were comparatively larger than those of samples T1, T2, and T5. Therefore, it is assumed that the cable termination installations of both groups had been of different quality. Over the next few weeks, these cable terminations underwent settling processes due to the applied thermal stresses (T samples have installed heat-shrink type of cable terminations). As a result, the apparent charge decreased for samples T3, T4, and T6. Subsequently, the apparent charge began to rise again, as in the case of the other T samples. The measurement shows a possible error in the 3rd week of sample T4 aging, whose values seem excessively high when compared to the other weeks. This error was most likely caused by external interference; the independence of the apparent charge on the applied voltage further confirms this claim. Since this sample was aged at the beginning of the experimental aging, this interference was removed in further measurements and later weeks as reference values became available.

Since the terminations of C samples have different technology, different behavior of PDs was observed during aging tests. The measured apparent charge was generally about one order of magnitude lower than for T samples. The apparent charge decreased over the first eighteen weeks in a similar manner for both samples C1 and C2. This effect was caused by the settling processes of cable terminations as well. During the installation of elastomeric cable terminations (C samples), a special lubricant is applied to fill all micro-voids and to ensure good adhesion of all technological layers. This lubricant is gradually absorbed into the surrounding materials as a consequence of electrical and thermal stresses during aging.

To better clarify of PDs behaviors, the dependence of apparent charge and number of PDs per second on aging time was plotted for one sample of each type of degradation, as is shown in Fig. 76. Sample T1 was selected due to the occurrence of the breakdown in a later week. On the other hand, T6 was chosen as its apparent charge and the number of PDs per second reached the highest values during the tests. Samples C1 and C2 were selected as the only representatives of this type of cable samples that were subjected to accelerated aging tests.

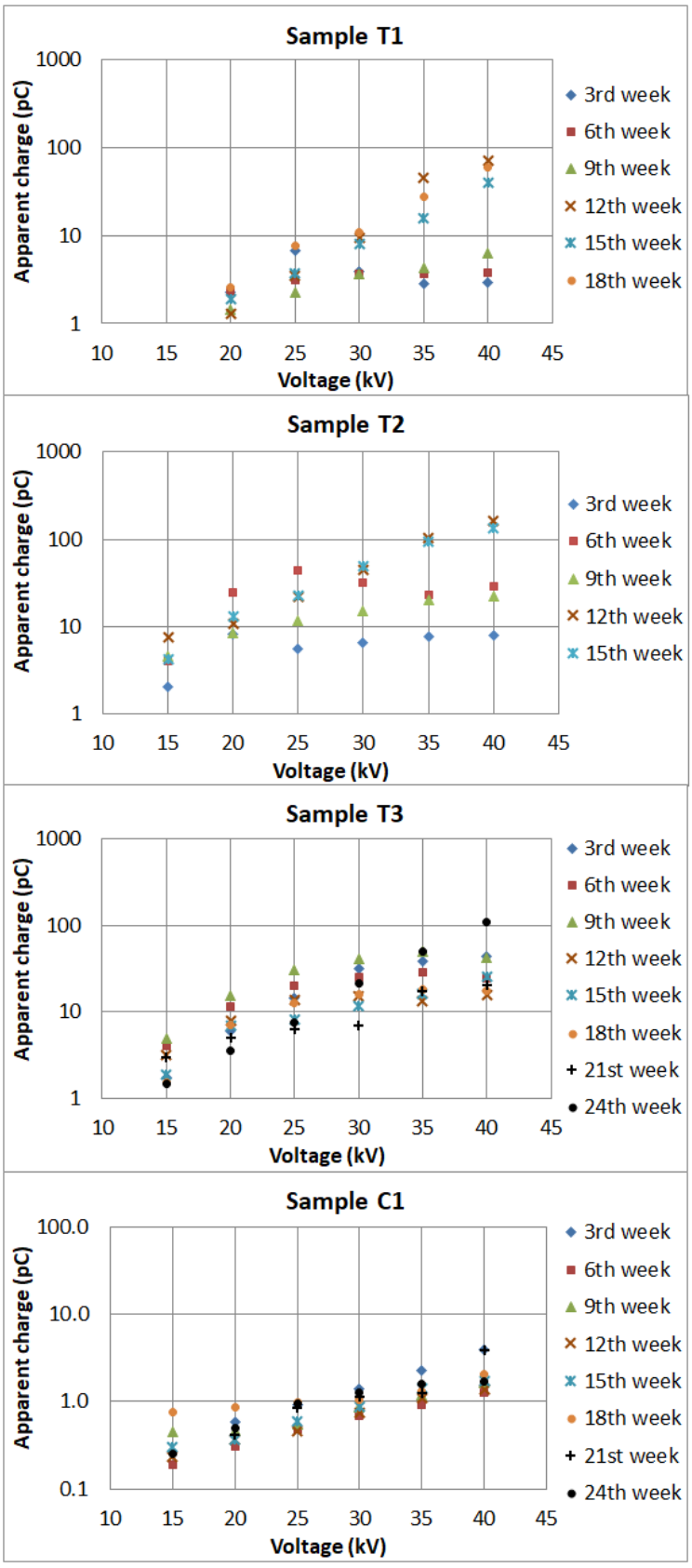

Fig. 74 Partial discharge (apparent charge) measurement during accelerated aging tests – samples under voltage stresses with high-frequency components (Partially reproduced from [A1])

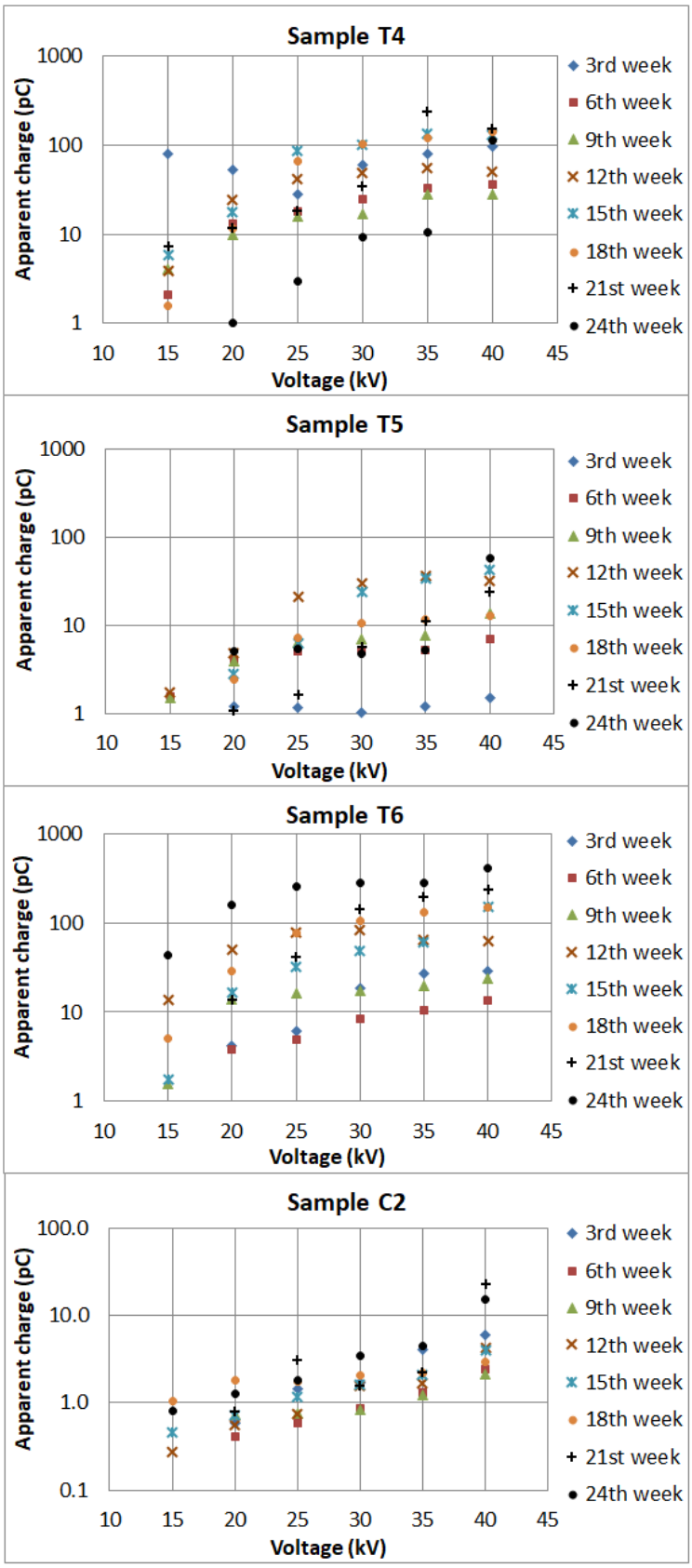

Fig. 75 Partial discharge (apparent charge) measurement during accelerated aging tests – samples under sinusoidal voltage stresses (Partially reproduced from [A1])

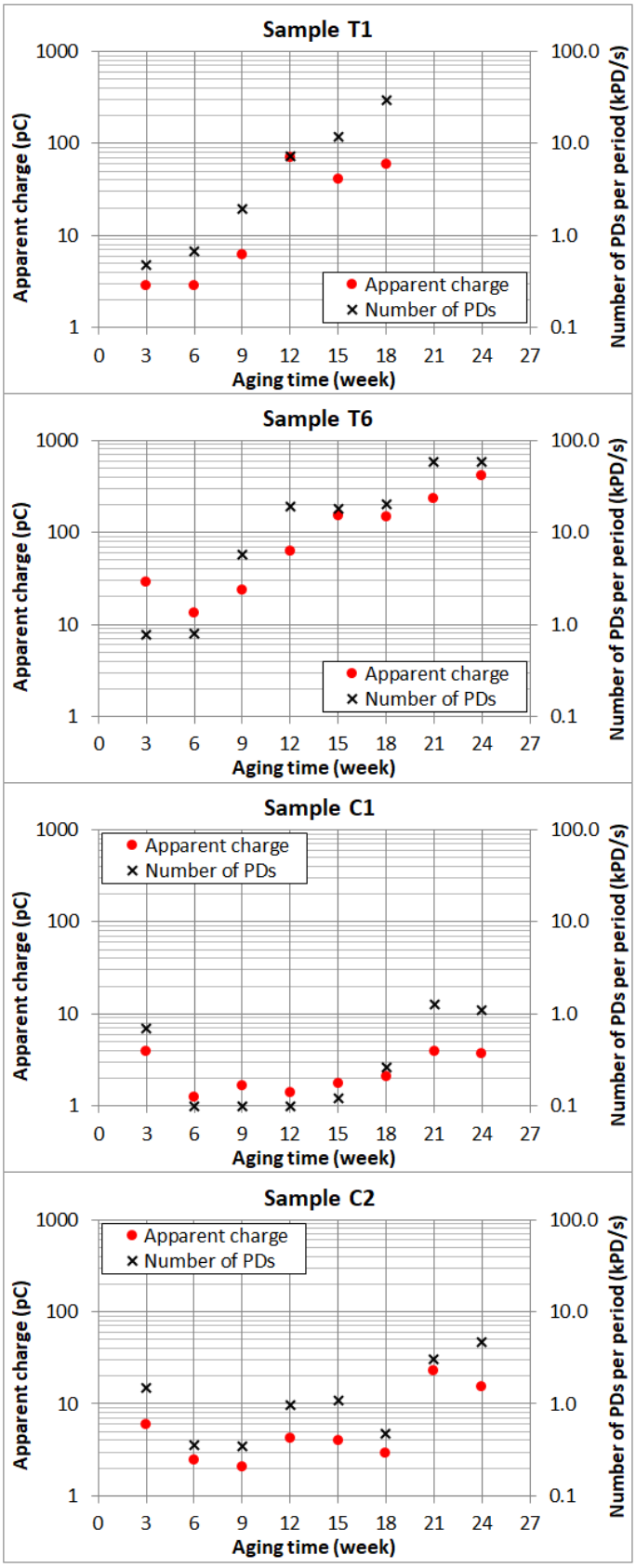

Fig. 76 Partial discharge (apparent charge and number of PDs per period) measurement at a voltage of 40 kV of samples T1, T6, C1, and C2 during accelerated aging tests (Partially reproduced from [A1])

Both trends for T samples show that the observed parameters are steadily increasing over time. Only apparent charge of T6 initially decreased, which is attributed to settling processes. These trends indicate that accelerated aging took place. On the other hand, trends for C samples show that observed parameters have increased over time in the last six weeks only. Values of apparent charge, as well as the number of PDs per second, are significantly lower than for T samples. As can be seen, the trends indicate that samples C1 and C2 have just finished settling, and that no significant aging of the samples has occurred.

Although both apparent charge and number of PDs per second were significantly higher for sample T6 than T1, the breakdown did not occur during the accelerated aging test. This result proves that PD measurements are not always objective, as it is a diagnostic method based on the measurement of local defects (micro-voids with PDs). PDs that occur in non-critical areas of the cable (e.g., discharges near the cable lug) that can have much higher magnitude and activity may overshadow the PDs occurring in the critical, most-stressed areas of the insulation.

6.3. Dissipation Factor

Dissipation factor measurement is an important diagnostic method of insulation systems as well. The dissipation factor can be defined as a ratio between permittivity and conductivity of an insulation system, whereas its conductivity increases with gradual degradation. It represents a diagnostic method for evaluating insulation as a whole without focusing on local defects. Before and after undergoing the accelerated aging tests, the cable samples were subjected to dissipation factor measurement by the Tettex Instruments system (capacitance and dissipation factor bridge type 2809 with null-indicator type 5511 and compressed gas capacitor type 3380/100/100 100 pF/100 kV), which can be seen in Fig. 77.

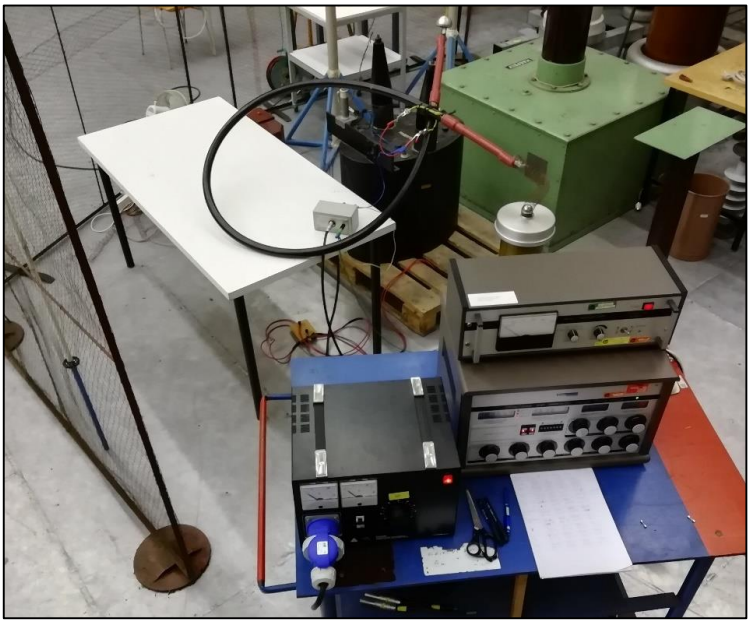

Fig. 77 Setup of the dissipation factor measurement

The relative changes of the measured values at voltage levels of 0.5, 1, 1.5, and 2 times the nominal phase voltage amplitude are shown in Fig. 78. Samples T1 and T2 had broken down during the aging tests, and therefore it was not possible to measure their dissipation factor afterward. Samples T4 to T6, which were aged by power frequency voltage only, show values similar or even lower than those obtained before the accelerated aging. This fact indicates that the cable samples had not been critically degraded. On the other hand, sample T3, which was aged by power frequency voltage with high-frequency distortion, similar to T1 and T2, showed an increase in its dissipation factor between 40 – 60 %. This result suggests that sample T3 had been degraded to a much higher degree than the others, which was expected due to breakdown of samples T1 and T2 during the aging tests.

However, a comparison of the apparent PD charge of samples T3 and T6 in the 24th week (at 40 kV) leads us to a different conclusion. Sample T6 reached an apparent charge of about 400 pC, whereas T3 reached only about 100 pC. As mentioned earlier, the difference may originate from the development of other types of PDs in non-critical areas of the insulation

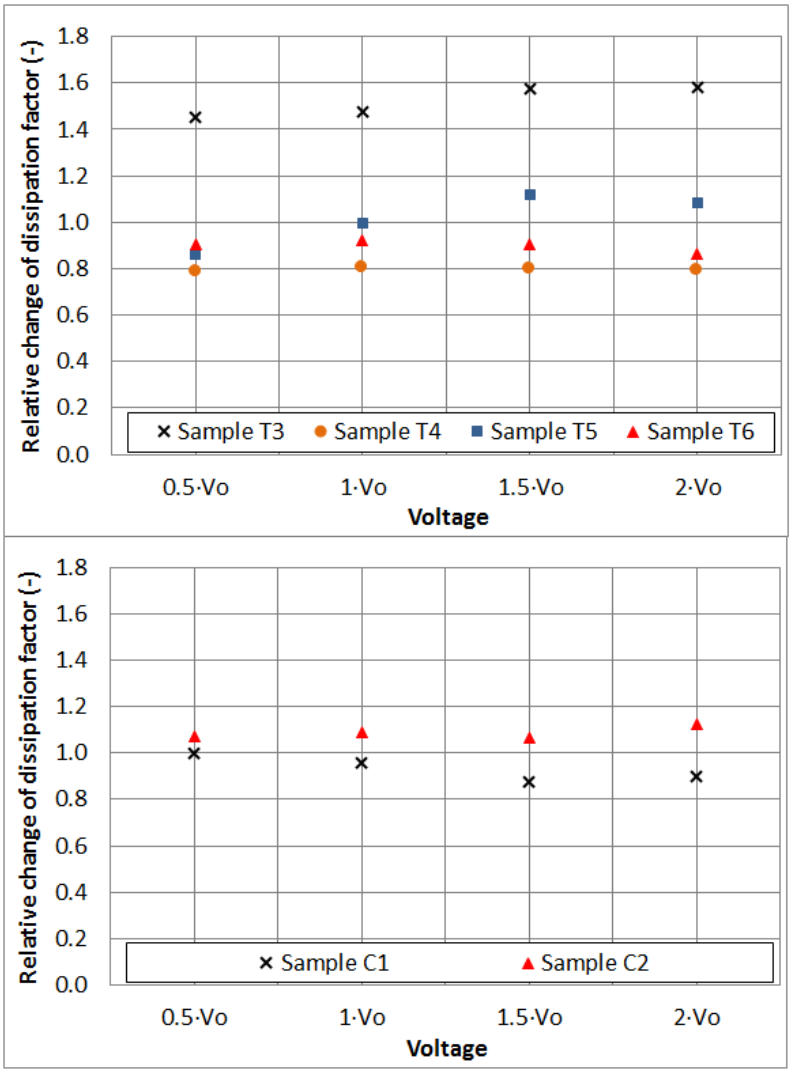

Fig. 78 Relative change of dissipation factor after accelerated aging tests (Partially reproduced from [A1])

system in sample T6. This contradiction illustrates the necessity of employing multiple diagnostic methods to evaluate the state of an insulation system objectively.

The situation is different for C samples. Although samples C1 and C2 were aged by different voltage stresses, measured values were similar or even lower than those obtained before the accelerated aging. As with PD measurements, dissipation factor measurements indicate no or only slight aging of both C samples.

7. DISCUSSION

The obtained results indicate that the voltage distortions have a negative impact on the degradation of insulation and, thus, on the lifetime of cable systems. In the case of T samples, two out of three cables, which were exposed to aging with high-frequency distortion, broke down prematurely during the aging tests. In the subsequent dielectric strength tests, the third T sample had a slightly lower breakdown voltage than the samples aged under non-distorted stresses. The X-ray scans performed on the samples revealed that the breakdown channel of all samples aged with high-frequency distortions formed directly through the cable XLPE insulation.

Furthermore, the effect of high-frequency distortion was clearly confirmed by dissipation factor measurements as well. Sample T3, which was aged with combined voltage stresses and withstood the whole tested period, showed an increase in dissipation factor of about 50 %. For T4-T6 samples, the dissipation factor was slightly lowered, which may have been caused by the initial settlings of the samples. These results show significantly faster degradation of the tested samples under voltage stresses with high-frequency components.

On the other hand, PD measurements provided ambiguous results. The recorded values may have been obtained from discharges occurring in non-critical defects of the insulation systems, which tended to have higher magnitude and activity. However, the time development of PD activity of tested T samples confirmed that they have reached sufficiently aged states. In contrast, diagnostic methods such as dissipation factor measurement provide information about the global state of insulation, while the onset of local faults might remain undetected. Therefore, these types of diagnostic methods tend to provide more convincing results if paired together.

On the base of published research on the accelerated aging of XLPE cables, e.g., a review of aging studies by Ch. Dang et al. in [106] or results of aging studies by H. Sarma et al. in [107], the effect of high-frequency voltage distortion on the lifetime of T cable samples can be roughly estimated. The results suggest a possible reduction in a lifetime by up to half.

The gathered results indicate the low degree of degradation of C cable samples (with elastomeric cable terminations). Therefore, these samples would require longer aging to provide comparative results. Breakdown voltage of C samples was identical for both aged and unaged samples. The results from PD and dissipation factor measurements suggest that all the aged C samples were in the state corresponding to the end of settling processes. This effect can be attributed to the different technology of cable terminations, in which a special lubricant is used during their assembly. Although the influence of high-frequency voltage distortion in the case of C samples cannot be reliably determined from the gathered results. The results indicate

higher resistance of elastomeric cable terminations to electro-thermal aging generally. Such observation is rather surprising and should be thoroughly investigated in future works.

8. CONCLUSION

The doctoral research was focused on investigations of the effects of high-frequency voltage distortions on medium voltage cable systems in electrical networks. On the basis of the overview of the issue, which was presented in Chapter 2, the following partial goals were achieved:

- The numerical simulation of a part of the electric network connected to a large photovoltaic power plant confirms the occurrence of high-frequency voltage distortions in power systems. The sinusoidal voltage waveform was significantly distorted by harmonics around 3, 6, and 9 kHz. Although the values of lower harmonics were acceptable according to the limits of the valid standards, the total harmonic distortion (THD) from the entire frequency spectrum reached the value of almost 18 % in a medium voltage electrical network. This distortion causes a constant repetitive fast overvoltage of up to 1.2 p.u.
- A specialized test site was constructed for accelerated electrical and thermal aging. The test site allows long-term stresses of medium voltage insulation systems with increased temperature and increased voltage. Voltage stresses can be a combination of power frequency sinusoidal voltage and superimposed variable shape of voltage distortions. The realized test site also includes an automatic monitoring system of fundamental diagnostic data.
- Experimental accelerated aging tests were performed on sets of cable samples with heat-shrink and elastomeric terminations. The test period for each tested sample was 24 weeks. The shape of the testing voltage resulted from the performed numerical simulations.
- Breakdown voltage tests, measurements of dissipation factor, partial discharge measurements, and X-ray scanning of cable terminations after breakdowns showed faster degradation of cable samples with heat-shrink cable termination under stresses with voltage distortions then under stresses with pure sinusoidal voltage only.

The partial goals results point to the high severity of the issue of high-frequency distortions in a power system. As the experiments have shown, the role of high-frequency distortion on the degradation of a real medium voltage insulation system can be significant. The proven substantial shortening of the lifetime of cable system samples shows the necessity to address this issue in practice in power systems. In the future, this phenomenon is likely to cause more and more premature failures of insulation systems in current installations of many

high-performance electronic devices into power systems. For this reason, this problem should be addressed intensively, and appropriate technical standards should be developed.

The performed investigation showed the extraordinary difficulty of experimental testing of real insulation systems. The research included many added factors of the real complex insulation systems, which had to be accounted for. This testing method is in sharp contrast to tests performed on simple small-scale samples of insulation materials. However, the added difficulties are often outweighed by the objectivity and representability of the obtained results. Therefore, such investigations on real insulation systems are required to provide a deeper understanding of degradation processes in present electrical power systems. Further research can be developed in two ways. As a first direct way, more different cable samples can be aged, and more detailed testing can be performed. It may be interesting to perform some material analyses to determine in more detail the degradation processes of insulation material under high-frequency distortion. Another way is to compare these results with testing of other important complex insulation systems, such as paper-oil insulations or foil-epoxy resin insulations that occur in power transformers.

REFERENCES

[1] *Voltage characteristics of electricity supplied by public electricity networks*, CENELEC Standard EN 50160:2010.

[2] *Electromagnetic compatibility (EMC) - Part 3-6: Limits - Assessment of emission limits for the connection of distorting installations to MV, HV and EHV power systems*, Standard IEC TR 61000-3-6:2008.

[3] *IEEE Recommended Practice and Requirements for Harmonic Control in Electric Power Systems*, IEEE Standard 519-2014 (Revision of IEEE Standard 519-1992), June 2014.

[4] S. B. Warder, E. Friedlander and A. N. Arman, "The influence of rectifier harmonics in a railway system on the dielectric stability of 33-kV cables," in *Proceedings of the IEE – Part II: Power Engineering*, vol. 98, no. 63, pp. 399-411, June 1951.

[5] K. Uchida, S. Kobayashi, T. Kawashima, H. Tanaka, S. Sakuma, K. Hirotsu and H. Inoue, "Study on detection for the defects of XLPE cable lines," in *IEEE Transactions on Power Delivery*, vol. 11, no. 2, pp. 663-668, April 1996.

[6] Bin Wu, *High Power Converters and AC Drives*, Piscataway, NJ: Wiley-IEEE Press, 333 p., 2006. ISBN 04-717-3171-4.

[7] S. K. Rönnberg, M. H. J. Bollen, H. Amaris, G. W. Chang, I. Y. H. Gu, Ł. H. Kocewiak, J. Meyer, M. Olofsson, P. F. Ribeiro and J. Desmet, "On waveform distortion in the frequency range of 2 kHz–150 kHz - Review and research challenges," in *Electric Power Systems Research*, vol. 150, pp. 1-10, September 2017.

[8] S. Rönnberg, A. Larsson, M. Bollen and J.-L. Schanen, "A simple model for interaction between equipment at a frequency of some tens of kHz," in *Proceedings of 21st International Conference on Electricity Distribution (CIRED)*, Frankfurt, Germany, p. 206, 6-9 June 2011.

[9] M. H. J. Bollen and S. K. Rönnberg, "Primary and secondary harmonics emission; harmonic interaction - a set of definitions," in *Proceedings 2016 17th International Conference on Harmonics and Quality of Power (ICHQP)*, Belo Horizonte, Brazil, pp. 703-708, 16-19 October 2016.

[10] K. Lee, D. Carnovale, D. Young, D. Ouellette and J. Zhou, "System Harmonic Interaction Between DC and AC Adjustable Speed Drives and Cost Effective Mitigation," in *IEEE Transactions on Industry Applications*, vol. 52, no. 5, pp. 3939-3948, Sept.-Oct. 2016.

[11] F. Endrejat, and P. Pillay, "Resonance overvoltages in medium-voltage multilevel drive systems," in *IEEE Transactions on Industry Applications*, vol. 45, no. 4, pp. 1199-1209, July-August 2009.

[12] J. Rodriguez, J. Pontt, C. Silva, R. Musalem, P. Newman, R. Vargas and S. Fuentes, "Resonances and overvoltages in a medium-voltage fan motor drive with long cables in an underground mine," in *IEEE Transactions on Industry Applications*, vol. 42, no. 3, pp. 856-863, May-June 2006.

[13] L. Paulsson, B. Ekehov, S. Halen, T. Larsson, L. Palmqvist, A. Edris, D. Kidd, A. J. F. Keri, and B. Mehraban, "High-frequency impacts in a converter-based back-to-back tie; the Eagle Pass installation," in *IEEE Transactions on Power Delivery*, vol. 18, no. 4, pp. 1410-1415, October 2003.

[14] T. Bengtsson, F. Dijkhuizen, Li Ming, F. Sahlén, L. Liljestrand, D. Bormann, R. Papazyan and M. Dahlgren, "Repetitive fast voltage stresses - causes and effects," in *IEEE Electrical Insulation Magazine*, vol. 25, no. 4, pp. 26-39, July-August 2009.

[15] K. Temma, F. Ishiguro, N. Toki, I. Iyoda and J. Paserba, "Clarification and measurements of high frequency harmonic resonance by a voltage sourced converter," in *IEEE Transactions on Power Delivery*, vol. 20, no. 1, pp. 450-457, January 2005.

[16] O. Galland, L. Eggenschwiler, R. Horta, W. Sattinger, P. Favre-Perrod and D. Roggo, "Application of Resonance Analysis to AC–DC Networks," in *IEEE Transactions on Power Delivery*, vol. 33, no. 3, pp. 1438-1447, June 2018.

[17] W. Wu, Z. Xie, Y. Chen, J. Liu, J. Guo, Y. Xu, H. Wang and An Luo, "Analysis and suppression of high-frequency oscillation between converter-based source and loads in an island power system," in *International Journal of Electrical Power & Energy Systems*, vol. 117, article no. 105616, May 2020.

[18] M. Brenna, A. Capasso, M. C. Falvo, F. Foiadelli, R. Lamedica and D. Zaninelli, "Investigation of resonance phenomena in high speed railway supply systems: Theoretical and experimental analysis" in *Electric Power System Research*, vol. 81, no. 10, pp. 1915-1923, October 2011.

[19] A. Dolara, M. Gualdoni and S. Leva, "Impact of High-Voltage Primary Supply Lines in the 2 x 25 kV–50 Hz Railway System on the Equivalent Impedance at Pantograph Terminals," in *IEEE Transactions on Power Delivery*, vol. 27, no. 1, pp. 164-175, January 2012.

[20] H. M. Roudsari, A. Jalilian and S. Jamali, "Resonance assessment in electrified railway systems using comprehensive model of train and overhead catenary system," in *Proceedings 2015 IEEE International Conference on Industrial Technology (ICIT)*, Seville, Spain, pp. 1142-1148, 17-19 March 2015.

[21] H. Hu, M. Zhang, C. Qian, Z. He and L. Fang, "Research on the Harmonic Transmission Characteristic and the Harmonic Amplification and Suppression in High-Speed Traction System," in *Proceedings 2011 Asia-Pacific Power and Energy Engineering Conference*, Wuhan, China, pp. 1-4, 25-28 March 2011.

[22] Z. He, H. Hu, Y. Zhang and S. Gao, "Harmonic Resonance Assessment to Traction Power-Supply System Considering Train Model in China High-Speed Railway," in *IEEE Transactions on Power Delivery*, vol. 29, no. 4, pp. 1735-1743, August 2014.

[23] H. Hu, Y. Shao, L. Tang, J. Ma, Z. He and S. Gao, "Overview of Harmonic and Resonance in Railway Electrification Systems," in *IEEE Transactions on Industry Applications*, vol. 54, no. 5, pp. 5227-5245, September-October 2018.

[24] L. Monjo, L. Sainz, J. Liang and J. Pedra, "Study of resonance in wind parks, " in *Electric Power Systems Research*, vol. 128, pp. 30-38, November 2015.

[25] Jim Guo, "Online diagnosis of power systems insulation condition in wind farms," in *Proceedings 2017 IEEE Electrical Insulation Conference (EIC)*, Baltimore, MD, USA, pp. 433-436, 11-14 June 2017.

[26] L. Jessen and F. W. Fuchs, "Investigation of renewable energy generation and load impact on the grid impedance at different points of connection in public low voltage grids to support grid integration of renewable energies," in *Proceedings 2016 18th European Conference on Power Electronics and Applications (EPE'16 ECCE Europe)*, Karlsruhe, pp. 1-10, 5-9 September 2016.

[27] O. S. Nduka and B. C. Pal, "Harmonic Domain Modeling of PV System for the Assessment of Grid Integration Impact," in *IEEE Transactions on Sustainable Energy*, vol. 8, no. 3, pp. 1154-1165, July 2017.

[28] R. Torquato, W. Freitas, G. R. T. Hax, A. R. Donadon and R. Moya, "High frequency harmonic distortions measured in a Brazilian solar farm," in *Proceedings 2016 17th International Conference on Harmonics and Quality of Power (ICHQP)*, Belo Horizonte, Brazil, pp. 623-627, 16-19 October 2016.

[29] T. Joshi, G. Heydt and R. Ayyanar, "An Analysis Approach for the Assessment of Pulse-width Modulated Carrier Frequency Spectral Components in Power Distribution Systems with Photovoltaic Resources," in *Electric Power Components and Systems*, vol. 43, no. 18, pp. 2094-2104, September 2015.

[30] Working Group JWG C4/C6.29 CIGRE, *Power Quality Aspects of Solar Power*, Technical Brochure 672, CIGRE, Paris, 109 p., December 2016.

[31] *Energetické kabely/Medium voltage cables, Product Catalogue (CZ/EN)*, NKT cables, 340 p., 2012.

[32] V. Vahedy, "Polymer insulated high voltage cables," in *IEEE Electrical Insulation Magazine*, vol. 22, no. 3, pp. 13-18, May-June 2006.

[33] R. Strobl, W. Haverkamp, G. Malin and F. Fitzgerald, "Evolution of stress control systems in medium voltage cable accessories," in *Proceedings 2001 IEEE/PES Transmission and Distribution Conference and Exposition. Developing New Perspectives*, Atlanta, GA, USA, vol. 2, pp. 843-848, 2 November 2001.

[34] R. Strobl, W. Haverkamp, G. Malin and F. Fitzgerald, "Medium voltage terminations using an advanced stress control technology," in *Proceedings 2001 IEEE/PES Transmission and Distribution Conference and Exposition. Developing New Perspectives*, Atlanta, GA, USA, vol. 2, pp. 771-775, 2 November 2001.

[35] *Assembly Instructions ESD-3824-CZ-11/09 / Montážní návod ESD-3824-CZ-11/09, Koncovka pro stíněné jednožilové jednoplášťové kabely s plastovou izolací do napětí 42 kV – Typ: POLT (in Czech)*, Tyco Electronics Czech – Energy Division, 8 p., 2011.

[36] *Assembly Instructions EPP-1153-CZ-11/06 / Montážní návod EPP-1153-CZ-11/06, Koncovka pro stíněné jednožilové kabely s plastovou izolací pro napětí 10 kV a 22 kV bez pancíře – Typ: TFTI/TFTO (in Czech)*, Tyco Electronics Czech – Energy Division, 6 p., 2011.

[37] J. P. Bellomo, P. Castelan and T. Lebey, "The effect of pulsed voltages on dielectric material properties," in *IEEE Transactions on Dielectrics and Electrical Insulation*, vol. 6, no. 1, pp. 20-26, February 1999.

[38] B. Sonerud, T. Bengtsson, J. Blennow and S. M. Gubanski, "Dielectric heating in insulating materials subjected to voltage waveforms with high harmonic content," in *IEEE Transactions on Dielectrics and Electrical Insulation*, vol. 16, no. 4, pp. 926-933, August 2009.

[39] K. Niayesh and E. Gockenbach, "On the aging mechanism of solid insulating materials exposed to repetitive high voltage pulses," in *IEEE Transactions on Dielectrics and Electrical Insulation*, vol. 21, no. 1, pp. 304-310, February 2014.

[40] M. Florkowski and B. Florkowska, "Distortion of partial-discharge images caused by high-voltage harmonics," in *IEE Proceedings - Generation, Transmission and Distribution*, vol. 153, no. 2, pp. 171-180, 16 March 2006.

[41] M. Florkowski, B. Florkowska, J. Furgal and P. Zydron, "Impact of high voltage harmonics on interpretation of partial discharge patterns," in *IEEE Transactions on Dielectrics and Electrical Insulation*, vol. 20, no. 6, pp. 2009-2016, December 2013.

[42] E. Lindell, T. Bengtsson, J. Blennow and S. M. Gubanski, "Influence of rise time on partial discharge extinction voltage at semi-square voltage waveforms," in *IEEE Transactions on Dielectrics and Electrical Insulation*, vol. 17, no. 1, pp. 141-148, February 2010.

[43] B. Florkowska, J. Roehrich, P. Zydroi and M. Florkowski, "Measurement and analysis of surface partial discharges at semi-square voltage waveforms," in *IEEE Transactions on Dielectrics and Electrical Insulation*, vol. 18, no. 4, pp. 990-996, August 2011.

[44] P. Wang, A. Cavallini, G. C. Montanari and G. Wu, "Effect of rise time on PD pulse features under repetitive square wave voltages," in *IEEE Transactions on Dielectrics and Electrical Insulation*, vol. 20, no. 1, pp. 245-254, February 2013.

[45] X. Wang, N. Taylor and H. Edin, "Enhanced distinction of surface and cavity discharges by trapezoid-based arbitrary voltage waveforms," in *IEEE Transactions on Dielectrics and Electrical Insulation*, vol. 23, no. 1, pp. 435-443, February 2016.

[46] R. J. Densley, "Partial Discharges in Electrical Insulation under Combined Alternating and Impulse Stresses," in *IEEE Transactions on Electrical Insulation*, vol. EI-5, no. 4, pp. 96-103, December 1970.

[47] J. Wu, A. Rodrigo Mor and J. J. Smit, "The effects of superimposed impulse transients on partial discharge in XLPE cable joint," in *International Journal of Electrical Power & Energy Systems*, vol. 110, pp. 497-509, September 2019.

[48] R. A. Fouracre, E. Santos, I. Timoshkin, M. J. Given and S. J. Macgregor, "Surface Discharge Propagation: The Influence Of Surface Charge," in *Conference Record of the 2006 Twenty-Seventh International Power Modulator Symposium*, Arlington, VA, USA, pp. 39-42, 14-18 May 2006.

[49] B. Florkowska, M. Florkowski, A. Rybak and P. Zydroń, "Comparison of PWM and SIN aging of insulating material subjected to surface discharges," in *2012 Annual Report Conference on Electrical Insulation and Dielectric Phenomena (CEIDP)*, Montreal, QC, Canada, pp. 44-47, 14-17 October 2012.

[50] M. Florkowski, B. Florkowska, A. Rybak and P. Zydron, "Metal migration at conductor / XLPE interface subjected to partial discharges at different electrical stresses," in *IEEE Transactions on Dielectrics and Electrical Insulation*, vol. 22, no. 1, pp. 456-462, February 2015.

[51] Li Ming, F. Sahlen, S. Halen, G. Brosig and L. Palmqvist, "Impacts of high-frequency voltage on cable-terminations with resistive stressgrading," in *Proceedings of the 2004 IEEE International Conference on Solid Dielectrics (ICSD 2004)*, Toulouse, France, pp. 300-303, Vol. 1, 5-9 July 2004.

[52] F. P. Espino-Cortes, S. Jayaram and E. A. Cherney, "Stress grading materials for cable terminations under fast-rise time pulses," in *IEEE Transactions on Dielectrics and Electrical Insulation*, vol. 13, no. 2, pp. 430-435, April 2006.

[53] U. Patel, S. H. Jayaram, A. El-Hag and R. Seetahpathy, "MV cable termination failure assessment in the context of increased use of power electronics," in *Proceedings 2011 Electrical Insulation Conference (EIC)*, Annapolis, MD, USA, pp. 418-422, 5-8 June 2011.

[54] Y. O. Shaker, A. El-Hag, U. Patel and S. H. Jayaram, "Thermal modeling of medium voltage cable terminations under square pulses," in *IEEE Transactions on Dielectrics and Electrical Insulation*, vol. 21, no. 3, pp. 932-939, June 2014.

[55] U. Patel, S. H. Jayaram and A. El-Hag, "Analysis of cable termination under power frequency and high frequency voltages," in *Proceedings 2011 Annual Report Conference on Electrical Insulation and Dielectric Phenomena (CEIDP)*, Cancun, Mexico, pp. 288-291, 16-19 October 2011.

[56] S. Banerjee and S. H. Jayaram, "Performance of medium voltage cable terminations under high frequency voltage waveforms," in *Proceedings 2010 International Conference on Industrial and Information Systems (ICIIS)*, Mangalore, India, pp. 538-543, 29 July – 1 August 2010.

[57] R. Patsch, "Electrical and water treeing: a chairman's view," in *IEEE Transactions on Electrical Insulation*, vol. 27, no. 3, pp. 532-542, June 1992.

[58] R. Ross, "Inception and propagation mechanisms of water treeing," in *IEEE Transactions on Dielectrics and Electrical Insulation*, vol. 5, no. 5, pp. 660-680, October 1998.

[59] L. A. Dissado, "Understanding electrical trees in solids: from experiment to theory," in *IEEE Transactions on Dielectrics and Electrical Insulation*, vol. 9, no. 4, pp. 483-497, August 2002.

[60] E. Gulski, H. Putter and J. J. Smit, "Investigation of water treeing — electrical treeing transition in power cables," in *Proceedings International Conference on Condition Monitoring and Diagnosis (CMD 2008)*, Beijing, China, pp. 234-237, 21-24 April 2008.

[61] F. Noto and N. Yoshimura, "Voltage and frequency dependence of tree growth in polyethylene," in *Conference on Electrical Insulation & Dielectric Phenomena - Annual Report 1974 (CEIDP)*, Downingtown, PA, USA, pp. 207-217, 21-23 October 1974.

[62] G. Chen and C. H. Tham, "Electrical treeing characteristics in XLPE power cable insulation in frequency range between 20 and 500 Hz," in *IEEE Transactions on Dielectrics and Electrical Insulation*, vol. 16, no. 1, pp. 179-188, February 2009.

[63] I. Iddrissu and S. M. Rowland, "The impact of harmonic frequencies on electrical tree growth in epoxy resin," in *Proceedings 2017 IEEE Conference on Electrical Insulation and Dielectric Phenomenon (CEIDP)*, Fort Worth, TX, USA, pp. 753-756, 22-25 November 2017.

[64] M. Bao, X. Yin and J. He, "Structure characteristics of electrical treeing in XLPE insulation under high frequencies," in *Physica B: Condensed Matter*, vol. 406, no. 14, pp. 2885-2890, July 2011.

[65] Y. Zhang, Y. Zhou, L. Zhang, Z. Zhou, and Q. Nie, "Electrical Trees and Their Growth in Silicone Rubber at Various Voltage Frequencies," in *Energies*, vol. 11, no. 2, p. 327, February 2018.

[66] R. Sarathi, A. Nandini and T. Tanaka, "Understanding electrical treeing phenomena in XLPE cable insulation under harmonic AC voltages adopting UHF technique," in *IEEE Transactions on Dielectrics and Electrical Insulation*, vol. 19, no. 3, pp. 903-909, June 2012.

[67] R. Sarathi, K. H. Oza, C. L. G. Pavan Kumar and T. Tanaka, "Electrical treeing in XLPE cable insulation under harmonic AC voltages," in *IEEE Transactions on Dielectrics and Electrical Insulation*, vol. 22, no. 6, pp. 3177-3185, December 2015.

[68] N. Yoshimura, F. Noto and K. Kikuchi, "Growth of Water Trees in Polyethylene and Silicone Rubber by Water Electrodes," in *IEEE Transactions on Electrical Insulation*, vol. EI-12, no. 6, pp. 411-416, December 1977.

[69] R. Bartnikas, H. C. Doepken, R. M. Eichhorn, G. W. Rittmann and W. D. Wilkens, "Accelerated Life Testing of Wet Cable Specimens at Frequencies Above 60 Hz," in *IEEE Transactions on Power Apparatus and Systems*, vol. PAS-99, no. 4, pp. 1575-1585, July 1980.

[70] H. Suzuki, S. Mukai, Y. Ohki, Y. Nakamichi and K. Ajiki, "Water-tree characteristics in low-density PE under simulated inverter voltages," in *IEEE Transactions on Dielectrics and Electrical Insulation*, vol. 5, no. 2, pp. 256-260, April 1998.

[71] J. P. Crine and J. Jow, "Influence of frequency on water tree growth in various test cells," in *IEEE Transactions on Dielectrics and Electrical Insulation*, vol. 8, no. 6, pp. 1082-1087, December 2001.

[72] D. Kaneko, T. Maeda, T. Ito, Y. Ohki, T. Konishi, Y. Nakamichi and M. Okashita, "Role of number of consecutive voltage zero-crossings in propagation of water trees in polyethylene," in *IEEE Transactions on Dielectrics and Electrical Insulation*, vol. 11, no. 4, pp. 708-714, August 2004.

[73] IEEE Task Force, "The Effects of Power System Harmonics on Power System Equipment and Loads," in *IEEE Transactions on Power Apparatus and Systems*, vol. PAS-104, no. 9, pp. 2555-2563, September 1985.

[74] E. F. Fuchs, D. J. Roesler and K. P. Kovacs, "Aging of Electrical Appliances Due to Harmonics of the Power System's Voltage," in *IEEE Transactions on Power Delivery*, vol. 1, no. 3, pp. 301-307, July 1986.

[75] V. E. Wagner, J. C. Balda, D. C. Griffith, A. McEachern, T. M. Barnes, D. P. Hartmann, D. J. Phileggi, A. E. Emannuel, W. F. Horton, W. E. Reid, R. J. Ferraro and W. T. Jewell, "Effects of harmonics on equipment," in *IEEE Transactions on Power Delivery*, vol. 8, no. 2, pp. 672-680, April 1993.

[76] G. Carpinelli, P. Caramia, E. Di Vito, A. Losi and P. Verde, "Probabilistic evaluation of the economical damage due to harmonic losses in industrial energy system," in *IEEE Transactions on Power Delivery*, vol. 11, no. 2, pp. 1021-1031, April 1996.

[77] A. Cavallini, G. Mazzanti and G. C. Montanari, "Probabilistic Investigation of the Life Behavior of Power Capacitors Operating Under Distorted Supply Voltage, " in *Lifetime Data Analysis*, vol. 3, no. 1, pp. 47-61, January 1997.

[78] A. Cavallini, I. Ghinello, G. Mazzanti and G. C. Montanari, "Considerations on the life performance and installation practice of shunt capacitors in the presence of harmonics generated by AC/DC converters," in *IEEE Transactions on Power Delivery*, vol. 14, no. 1, pp. 227-234, January 1999.

[79] G. C. Montanari and D. Fabiani, "Searching for the factors which affect self-healing capacitor degradation under non-sinusoidal voltage," in *IEEE Transactions on Dielectrics and Electrical Insulation*, vol. 6, no. 3, pp. 319-325, June 1999.

[80] G. C. Montanari and D. Fabiani, "The effect of nonsinusoidal voltage on intrinsic aging of cable and capacitor insulating materials," in *IEEE Transactions on Dielectrics and Electrical Insulation*, vol. 6, no. 6, pp. 798-802, December 1999.

[81] A. Cavallini, D. Fabiani, G. Mazzanti and G. C. Montanari, "Models for degradation of self-healing capacitors operating under voltage distortion and temperature," in *Proceedings of the 6th International Conference on Properties and Applications of Dielectric Materials (ICPADM)*, Xi'an, China, vol.1, pp. 108-111, 21-26 June 2000.

[82] D. Fabiani and G. C. Montanari, "The effect of voltage distortion on ageing acceleration of insulation systems under partial discharge activity," in *IEEE Electrical Insulation Magazine*, vol. 17, no. 3, pp. 24-33, May-June 2001.

[83] A. Cavallini, D. Fabiani and G. C. Montanari, "Power electronics and electrical insulation systems - Part 1: Phenomenology overview," in *IEEE Electrical Insulation Magazine*, vol. 26, no. 3, pp. 7-15, May-June 2010.

[84] A. Cavallini, D. Fabiani and G. C. Montanari, "Power electronics and electrical insulation systems - Part 2: Life modeling for insulation design," in *IEEE Electrical Insulation Magazine*, vol. 26, no. 4, pp. 33-39, July-August 2010.

[85] A. Cavallini, D. Fabiani and G. C. Montanari, "Power electronics and electrical insulation systems - Part 3: Diagnostic properties," in *IEEE Electrical Insulation Magazine*, vol. 26, no. 5, pp. 30-40, September-October 2010.

[86] S. Bahadoorsingh and S. M. Rowland, "Investigating the impact of harmonics on the breakdown of epoxy resin through electrical tree growth," in *IEEE Transactions on Dielectrics and Electrical Insulation*, vol. 17, no. 5, pp. 1576-1584, October 2010.

[87] S. Bahadoorsingh, S. Sambeharry, C. Sharma and S. M. Rowland, "The statistical analysis of harmonic influenced electrical treeing partial discharge data using the Weibull distribution," in *2011 Annual Report Conference on Electrical Insulation and Dielectric Phenomena (CEIDP)*, Cancun, Mexico, pp. 772-775, 16-19 October 2011.

[88] *IEC/IEEE Guide for the Statistical Analysis of Electrical Insulation Breakdown Data (Adoption of IEEE Standard 930-2004)*, Standard IEC 62539 First Edition 2007-07 IEEE 930, July 2007.

[89] Y. Cui, G. Wu, K. Cao and Y. Luo, "Life models of polyimide film under combined thermal and electrical stresses used in inverter-fed traction motor," in *2011 Annual Report Conference on Electrical Insulation and Dielectric Phenomena (CEIDP)*, Cancun, Mexico, pp. 80-83, 16-19 October 2011.

[90] M. Florkowski, B. Florkowska, A. Rybak and P. Zydron, "Metal migration at conductor / XLPE interface subjected to partial discharges at different electrical stresses," in *IEEE Transactions on Dielectrics and Electrical Insulation*, vol. 22, no. 1, pp. 456-462, February 2015.

[91] Z. Zuo, C. Yao, L. A. Dissado, N. M. Chalashkanov and S. J. Dodd, "Simulation of electro-thermal ageing and breakdown in polymeric insulation under high frequency trapezoidal-wave pulses," in *IEEE Transactions on Dielectrics and Electrical Insulation*, vol. 24, no. 6, pp. 3766-3775, December 2017.

[92] S. Grzybowski, P. Shrestha and L. Cao, "Electrical Aging Phenomena of XLPE and EPR Cable Insulation Energized by Switching Impulses," in *Proceedings 2008 International Conference on High Voltage Engineering and Application (ICHVE)*, Chongqing, China, pp. 422-425, 9-12 November 2008.

[93] L. Cao, S. Grzybowski and B. Pradhan, "Accelerated electrical aging of medium voltage EPR cables energized by elevated AC voltage with switching impulses superimposed," in *Proceedings 2013 IEEE Electric Ship Technologies Symposium (ESTS)*, Arlington, VA, USA, pp. 347-352, 22-24 April 2013.

[94] L. Cao and S. Grzybowski, "Accelerated aging study on 15 kV XLPE and EPR cables insulation caused by switching impulses," in *IEEE Transactions on Dielectrics and Electrical Insulation*, vol. 22, no. 5, pp. 2809-2817, October 2015.

[95] M. I. Qureshi, A. Al-Arainy and N. H. Malik, "Effect of Accelerated Laboratory Aging on Selected Electrical Properties of Medium-voltage Heat Shrink Cable Joints," in *Electric Power Components and Systems*, vol. 42, no. 5, pp. 496-506, February 2014.

[96] M. Ghassemi, "Accelerated insulation aging due to fast, repetitive voltages: A review identifying challenges and future research needs," in *IEEE Transactions on Dielectrics and Electrical Insulation*, vol. 26, no. 5, pp. 1558-1568, October 2019.

[97] R. R. A. Fortes, L. C. O. Oliveira, J. B. de Souza, R. F. Buzo and J. J. P. Álvarez, "Harmonic resonance in electrical grids with photovoltaic distributed generation," in *Proceedings 2016 17th International Conference on Harmonics and Quality of Power (ICHQP)*, Belo Horizonte, Brazil, pp. 214-219, 16-19 October 2016.

[98] A. Yazdani, A. R. Di Fazio, H. Ghoddami, M. Russo, M. Kazerani, J. Jatskevich, Kai Strunz, S. Leva and J. A. Martinez "Modeling Guidelines and a Benchmark for Power System Simulation Studies of Three-Phase Single-Stage Photovoltaic Systems," in *IEEE Transactions on Power Delivery*, vol. 26, no. 2, pp. 1247-1264, April 2011.

[99] A. S. Alfuhaid, "Frequency characteristics of single-phase two-winding transformers using distributed-parameter modeling," in *IEEE Transactions on Power Delivery*, vol. 16, no. 4, pp. 637-642, October 2001.

[100] L. Dalessandro, F. da Silveira Cavalcante and J. W. Kolar, "Self-Capacitance of High-Voltage Transformers, " in *IEEE Transactions on Power Electronics*, vol. 22, no. 5, pp. 2081-2092, September 2007.

[101] G. Herzer, "Chapter 3 Nanocrystalline soft magnetic alloys" in *Handbook of Magnetic Materials*, vol. 10, pp. 415-462, 1997.

[102] J. Petzold, "Applications of nanocrystalline softmagnetic materials for modern electronic devices" in *Scripta Materialia*, vol. 48, no. 7, pp. 895-901, 2003.

[103] R. Prochazka, J. Hlavacek and K. Draxler, "Magnetic Circuit of a High-Voltage Transformer up to 10 kHz," in *IEEE Transactions on Magnetics*, vol. 51, no. 1, pp. 1-4, January 2015.

[104] M. Kącki, M. S. Rylko, J. G. Hayes and C. R. Sullivan, "Magnetic material selection for EMI filters," in *Proceedings 2017 IEEE Energy Conversion Congress and Exposition (ECCE)*, Cincinnati, OH, USA, pp. 2350-2356, 1-5 October 2017.

[105] B. S. Bernstein, W. A. Thue, M. D. Walton and J. T. Smith, "Accelerated aging of extruded dielectric power cables. II. Life testing of 15 kV XLPE-insulated cables," in *IEEE Transactions on Power Delivery*, vol. 7, no. 2, pp. 603-608, April 1992.

[106] Ch. Dang, J. Parpal and J. Crine, "Electrical aging of extruded dielectric cables: review of existing theories and data," in *IEEE Transactions on Dielectrics and Electrical Insulation*, vol. 3, no. 2, pp. 237-247, April 1996.

[107] H. Sarma, E. Cometa and J. Densley, "Accelerated ageing tests on polymeric cables using water-filled tanks - a critical review," in *IEEE Electrical Insulation Magazine*, vol. 18, no. 2, pp. 15-26, March-April 2002.

[108] *IEEE Guide for Accelerated Aging Tests for Medium-Voltage (5 kV-35 kV) Extruded Electric Power Cables Using Water-Filled Tanks*, IEEE Standard 1407-2007 (Revision of IEEE Standard 1407-1998), February 2008.

[109] *Test methods for accessories for power cables with rated voltages from 6 kV (Um = 7,2 kV) up to 36 kV (Um = 42 kV)*, Standard IEC 61442:2005.

LIST OF AUTHOR'S PUBLICATIONS

State to September 2020. All authors hold an equal share in the joint publications.

Listed citations are drawn from Web of Science (w) and Scopus (s) databases and not include autocitations (both direct and indirect); the Scopus database also includes all citations from the Web of Science database.

Publications Related to the Thesis

Journal Publications (indexed in Web of Science)

[A1] M. Knenicky, R. Prochazka, J. Hlavacek and O. Sefl, "Impact of High-Frequency Voltage Distortion Emitted by Large Photovoltaic Power Plant on Medium Voltage Cable Systems," in *IEEE Transactions on Power Delivery*, DOI: 10.1109/TPWRD.2020.3016952. *(accepted to publish)* [IF 3.681]

Conference Publications (indexed in Web of Science)

[A2] M. Knenicky and R. Prochazka, "High Frequency Resonance Overvoltages in Distribution Network with Large Photovoltaic Power Plant," in *Proceedings 2019 10th International Scientific Symposium on Electrical Power Engineering (ELEKTROENERGETIKA)*, Stara Lesna, Slovakia, pp. 1-5, 16-18 September 2019.

[A3] M. Knenicky, R. Prochazka and J. Hlavacek, "Partial Discharge Patterns during Accelerated Aging of Medium Voltage Cable System," in *Proceedings 2018 IEEE International Conference on High Voltage Engineering and Application (ICHVE)*, Athens, Greece, pp. 1-4, 10-13 September 2018. [cited: 2]

- **w** J. Acosta, F. Amortegui, A. Escobar, L. Leon and S. Rivera, "Design and implementation of prototype for XLPE cable aging test", in *Revista Internacional de Métodos Numéricos para Cálculo y Diseño en Ingeniería (in Spanish)*, vol. 36, no. 3, pp. 1-9, July 2020.
- **s** D. A. Polyakov, I. V. Komarov, N. A. Tereschenko, K. I. Nikitin and U. V. Polyakova, "Research of Partial Discharges Intensity Voltage Dependence in XLPE-Insulated Cables," in *Proceedings 2020 International Youth Conference on Radio Electronics, Electrical and Power Engineering (REEPE)*, Moscow, Russia, pp. 1-5, 12-14 March 2020.

[A4] R. Prochazka, O. Sefl and M. Knenicky, "Partial Discharges Activity within an Internal Void at AC Voltage Disturbed by High Frequency Components," in *Proceedings 2018 IEEE International Conference on High Voltage Engineering and Application (ICHVE)*, Athens, Greece, pp. 1-4, 10-13 September 2018.

[A5] O. Sefl, M. Knenicky and R. Prochazka, "Life-Time of Oil Filled Insulation Paper under Nonstandard Voltage Stresses," in *Proceedings 2018 International Conference on Diagnostics in Electrical Engineering (Diagnostika)*, Pilsen, Czech Republic, pp. 1-4, 4-7 September 2018.

[A6] M. Knenicky, R. Prochazka and O. Sefl, "Influence of nonstandard voltage stresses on transformer insulation paper," in *Proceedings 2017 IEEE Conference on Electrical Insulation and Dielectric Phenomenon (CEIDP)*, Fort Worth, TX, USA, pp. 700-703, 22-25 November 2017. [cited: 1]

- **w** D. Feng, L. Yang, R. Liao, L. Zhou and Y. Lin, "Effect of moisture content on the production and partitioning of furfural in oil-paper insulation," in *IEEE Transactions on Dielectrics and Electrical Insulation*, vol. 25, no. 6, pp. 2389-2397, December 2018.

[A7] M. Knenicky and R. Prochazka, "Test site for nonstandard combined accelerated aging of medium voltage insulation systems," in *Proceedings 2016 IEEE International Conference on High Voltage Engineering and Application (ICHVE)*, Chengdu, China, pp. 1-4, 19-22 September 2016.

[A8] M. Knenicky and R. Prochazka, "High voltage test circuit for harmonic and impulse voltage stress," in *Proceedings 2015 16th International Scientific Conference on Electric Power Engineering (EPE),* Kouty nad Desnou, Czech Republic, pp. 377-380, 20-22 May 2015.

Other Publications

[A9] M. Knenicky and R. Prochazka, "Study of surface discharges on cable termination," in *Proceedings 2015 19th International Symposium on High Voltage Engineering (ISH)*, Plzen, Czech Republic, 5 p., 23-28 August 2015.

Publications Unrelated to the Thesis

Journal Publications (indexed in Web of Science)

Conference Publications (indexed in Web of Science)

[A10] J. Hlavacek, M. Knenicky and K. Draxler, "Calibration of Unipolar High Current Impulses for Resistance Spot Welding" in *Proceedings 2020 21st International Scientific Conference on Electric Power Engineering (EPE)*, Prague, Czech Republic, pp. 1-4, 19-21 October 2020. *(accepted to publish)*

[A11] J. Hlavacek and M. Knenicky, "Very fast high voltage impulse generator," in *Proceedings 2018 19th International Scientific Conference on Electric Power Engineering (EPE)*, Brno, Czech Republic, pp. 1-4, 16-18 May 2018. [cited: 4]

- **w** A. Merev, "Design and Implementation of Smart Impulse Voltage Calibrator" in *Journal of the Faculty of Engineering and Architecture of Gazi University*, vol. 34, no. 4, pp. 2229-2239, 2019.
- **s** S. Kurilin, V. Denisov and M. Dli, "Electromechanical Device for Braking Torque Impulses Generation," in *Proceedings 2020 International Conference on Industrial Engineering, Applications and Manufacturing (ICIEAM)*, Sochi, Russia, pp. 1-5, 18-22 May 2020.
- **s** I. Pătru, M. Nicola, C. Marinescu, L. Vlădoi and M. C. Nițu, "Applications of Voltage Pulse Generator to Achieve Current Pulses of High Amplitude," in *Proceedings 2019 International Conference on Electromechanical and Energy Systems (SIELMEN)*, Craiova, Romania, pp. 1-6, 9-11 October 2019.

- **s** S. R. Kerketta and D. Ghosh, "A Cost Effective Low Power Pulse Generator for UWB Medical Applications," in *Proceedings 2018 International Conference on Applied Electromagnetics, Signal Processing and Communication (AESPC)*, Bhubaneswar, India, pp. 1-4, 22-24 October 2018.

[A12] K. Draxler, R. Prochazka, J. Hlavacek, M. Knenicky and R. Styblikova, "Use of a nanocrystalline core for a precise non-invasive AC current measurement," in *Proceedings 2016 Conference on Precision Electromagnetic Measurements (CPEM)*, Ottawa, ON, Canada, pp. 1-2, 10-15 July 2016. [cited: 1]

- **w** S. M. Schneider, J. Sayago, M. Centner R. Plath and U. Schafer, "Measurement uncertainty of power measurement on inverter-fed drives in the medium voltage range," in *Elektrotechnik und Informationstechnik (in German)*, vol. 134, no. 2, pp. 203-211, April 2017.

[A13] K. Draxler, J. Hlavacek, R. Prochazka, M. Knenicky and R. Styblikova, "Clamp current transformers for noninvasive calibration of current transformers," in *Proceedings 2016 IEEE International Instrumentation and Measurement Technology Conference Proceedings (I2MTC)*, Taipei, Taiwan, pp. 1-6, 23-26 May 2016. [cited: 3]

- **w** C. Swieboda, J. Walak, M. Soinski, J. Rygal, J. Leszczynski and D. Grybos, "Nanocrystalline oval cut cores for current instrument transformer prototypes," in *Measurement*, vol. 136, no. 6, pp. 50-58, March 2019.
- **w** C. Swieboda, D. Grybos, J. Leszczynski and W. Pluta, "Influence of normal-compressed stresses on measurement precision of toroidal and oval nanocrystalline cut cores used for metering," in *Proceedings 2018 Innovative Materials and Technologies in Electrical Engineering (i-MITEL)*, Sulecin, Poland, pp. 1-4, 18-20 April 2018.
- **w** C. P. de Souza, J. Ferreira Moreira and Y. P. Molina Rodriguez, "A novel nanocrystalline-based current transformer working on saturated region," in *Proceedings 2017 IEEE International Instrumentation and Measurement Technology Conference (I2MTC)*, Turin, Italy, pp. 1-4, 22-25 May 2017.

[A14] R. Prochazka, J. Hlavacek, M. Knenicky and R. Mahmoud, "Determination of frequency characteristics of high voltage dividers in frequency domain," in *Proceedings 2016 17th International Scientific Conference on Electric Power Engineering (EPE)*, Prague, Czech Republic, pp. 1-4, 16-18 May 2016. [cited: 4]

- **w** Y. L. Anokhin, V. O. Brzhezytskyi, Y. O. Haran, I. M. Masliuchenko, O. P. Protsenko and Y. O. Trotsenko, "Application of high voltage dividers for power quality indices measurement," in *Electrical Engineering & Electromechanics*, no. 6, pp. 53-59, 2017.
- **s** V. Brzhezitsky, Y. Haran, A. Derzhuk, Y. Trotsenko and O. Protsenko, "Amplitude-Frequency Characteristic of Broadband Voltage Divider with Ultimate Adjustment of Its Low-Voltage Arm," in *Proceedings 2020 IEEE 7th International Conference on Energy Smart Systems (ESS)*, Kyiv, Ukraine, pp. 111-115, 12-14 May 2020.
- **s** Y. Trotsenko, V. Brzhezitsky, O. Protsenko and Y. Haran, "Experimental Laboratory Equipped with Voltage Dividers for Power Quality Monitoring," in *Proceedings 2019 IEEE International Conference on Modern Electrical and Energy Systems (MEES)*, Kremenchuk, Ukraine, pp. 270-273, 23-25 September 2019.
- **s** A. Łasica, and B. Chaber, "Examination of dynamic parameters of new impulse voltage divider designs", in *Przeglad Elektrotechniczny (in Polish)*, vol. 93, no. 10, pp. 69-72, October 2017.

[A15] J. Hlavacek, R. Prochazka, M. Knenicky, K. Draxler and R. Styblikova, "Influence of Rogowski coil shielding to measurement results," in *Proceedings 2016 17th International Scientific Conference on Electric Power Engineering (EPE)*, Prague, Czech Republic, pp. 1-5, 16-18 May 2016. [cited: 2]

- Y. Shi, Z. Xin, P. C. Loh and F. Blaabjerg, "A Review of Traditional Helical to Recent Miniaturized Printed Circuit Board Rogowski Coils for Power-Electronic Applications," in *IEEE Transactions on Power Electronics*, vol. 35, no. 11, pp. 12207-12222, November 2020.
- W. Yang, K. Song and L. Zhou, "Design and Research of the Magnetic Shielding Box of the Rogowski Coil", in *Gaoya Dianqi/High Voltage Apparatus (in Chinese)*, vol. 54, no. 12, pp. 158-164 and 173, December 2018.

Other Publications

[A16] M. Knenicky, "New method for transformer winding fault detection," in *Proceedings 2015 19th International Student Conference on Electrical Engineering (POSTER)*, Prague, Czech Republic, 6 p., 14 May 2015.

LIST OF FIGURES

LIST OF TABLES

APPENDICES

Appendix A: Results of Numerical Simulations of Distribution Network with Large Photovoltaic Power Plant

A1. Density Charts for Calculated THD_{V40} and THD_{Vall} in PV Node for Variable Cable and Overhead Line Lengths

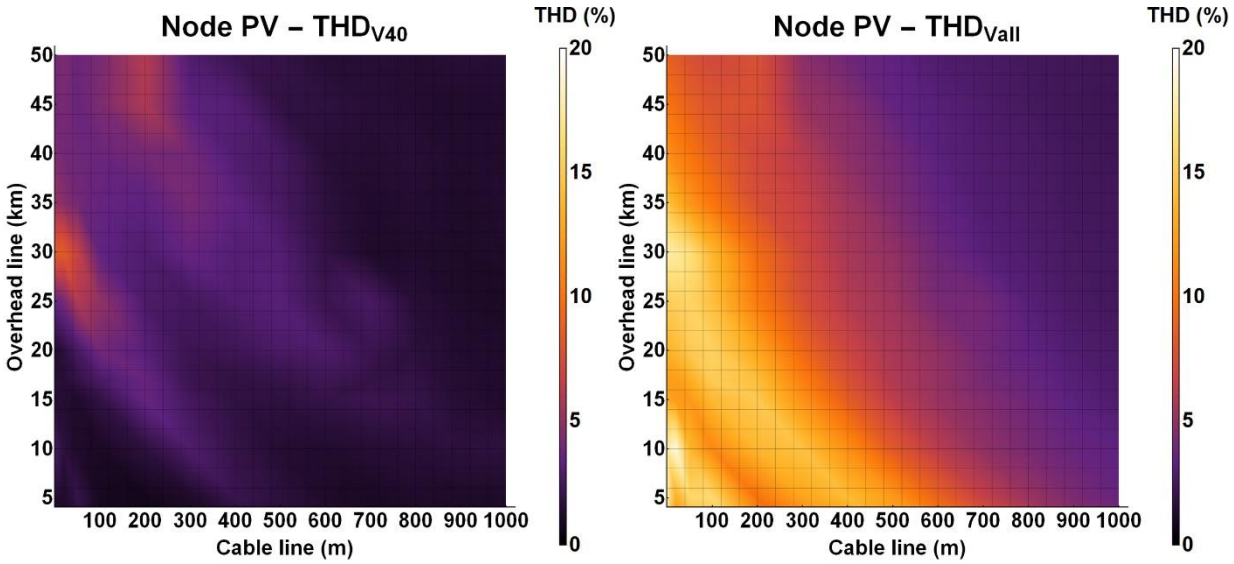

The short-circuit power of the 110-kV upstream power grid was set to 100 MVA during simulations, representing the location of the 110-kV substation at the end of a long feeder

A2. Overvoltage Dependence on Short-Circuit Power of 110-kV Upstream Power Grid for Four Different Combinations of Cable and Overhead Lines

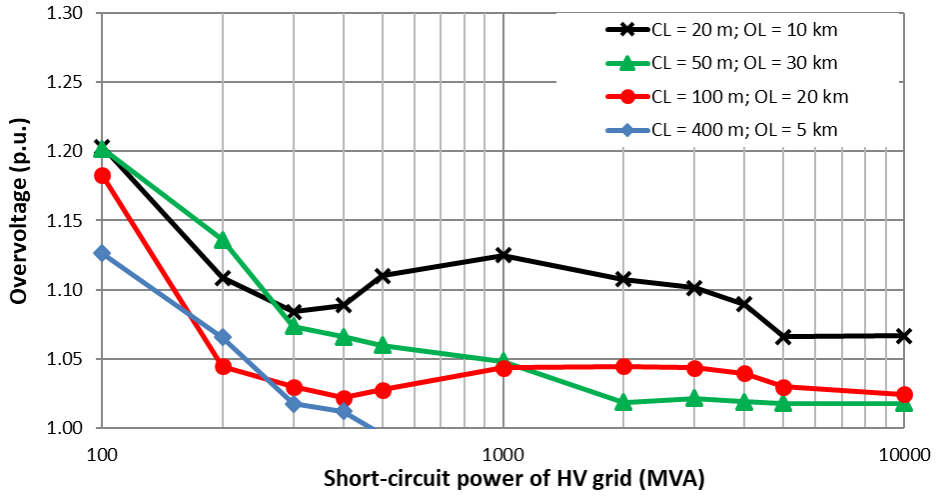

Legend: CL – cable line, OL – overhead line

A3. Voltage and Current Waveforms in LV Unit 1 Node with Frequency Spectrums of Voltage up to 40th and 350th Harmonic Order

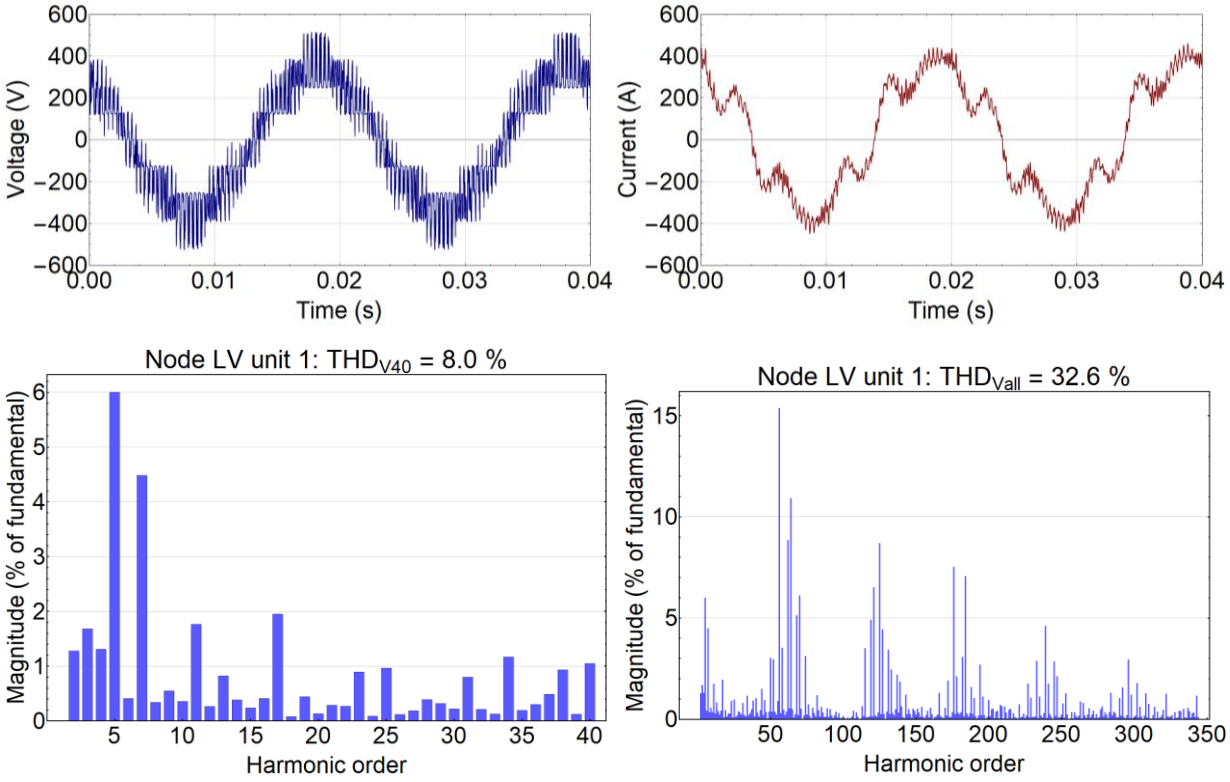

Cable line: 20 m; overhead line: 10 km; short-circuit power of 110-kV upstream power grid: 100 MVA

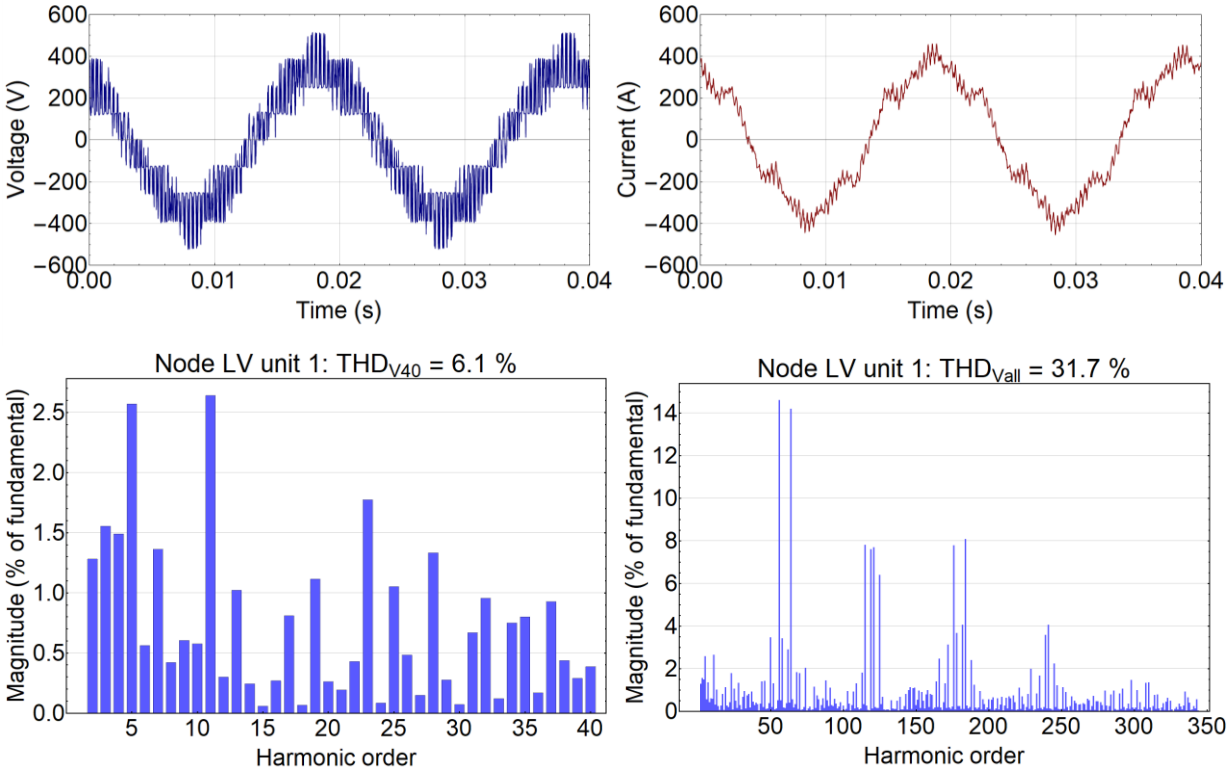

Cable line: 20 m; overhead line: 10 km; short-circuit power of 110-kV upstream power grid: 200 MVA

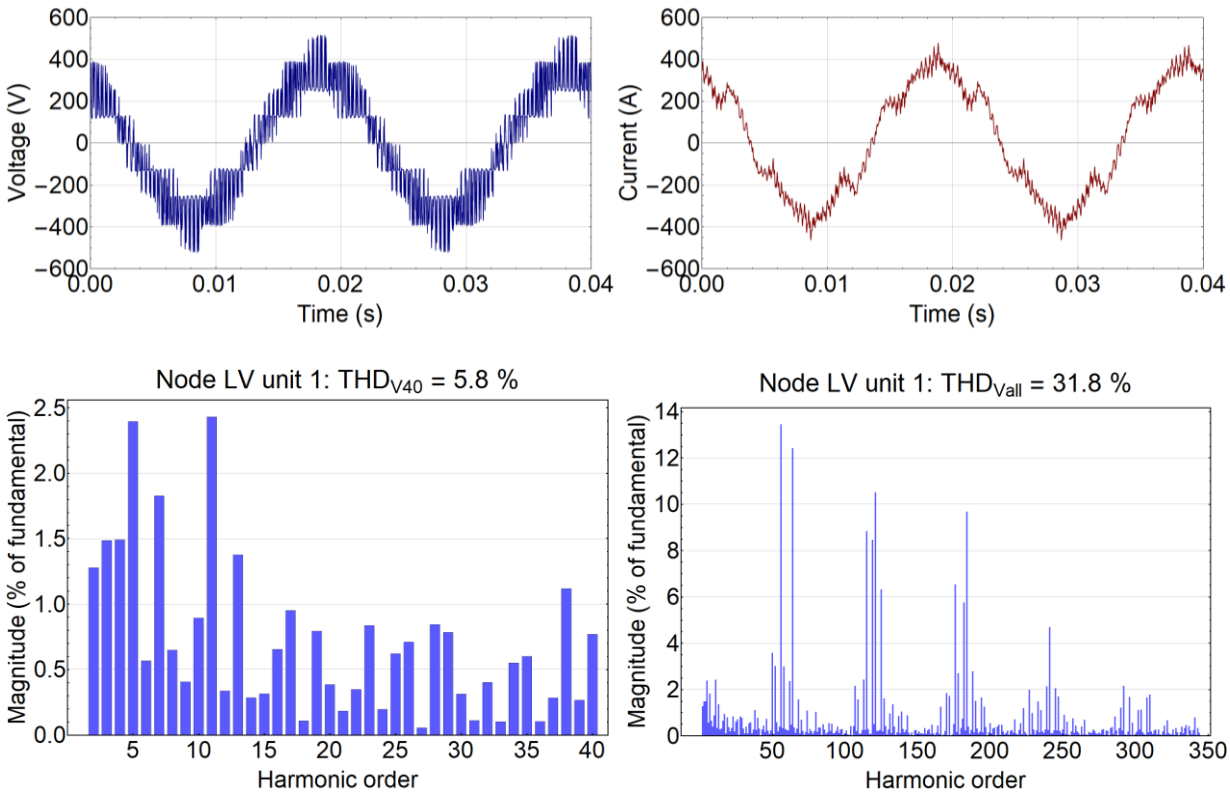

Cable line: 20 m; overhead line: 10 km; short-circuit power of 110-kV upstream power grid: 1000 MVA

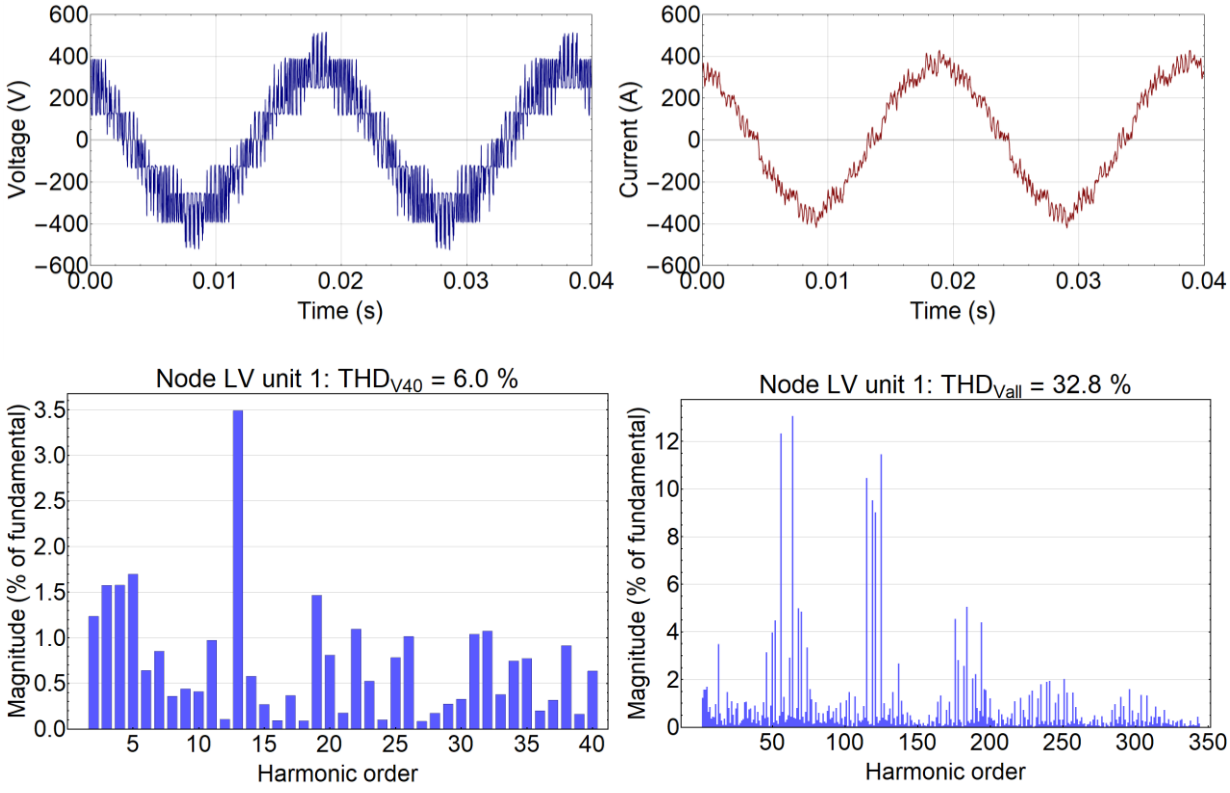

Cable line: 20 m; overhead line: 10 km; short-circuit power of 110-kV upstream power grid: 5000 MVA

A4. Voltage and Current Waveforms in PV Node with Frequency Spectrums of Voltage up to 40th and 350th Harmonic Order

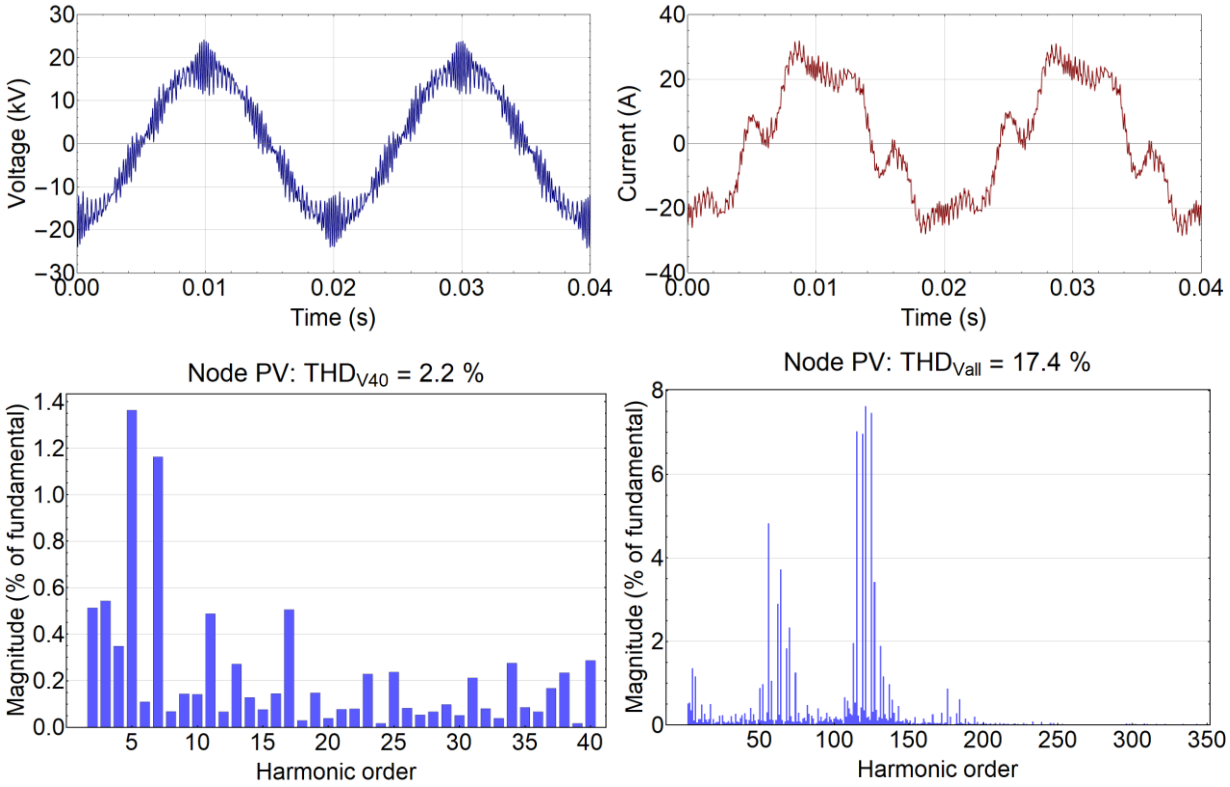

Cable line: 20 m; overhead line: 10 km; short-circuit power of 110-kV upstream power grid: 100 MVA

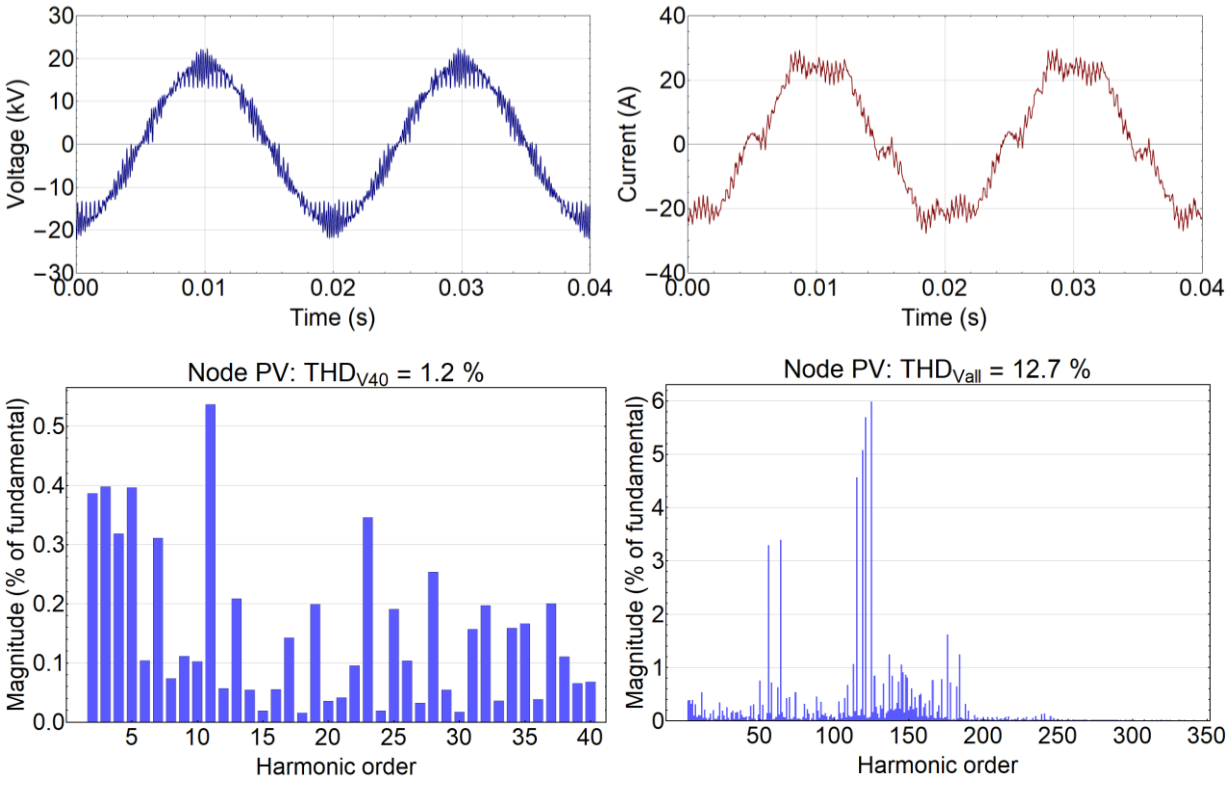

Cable line: 20 m; overhead line: 10 km; short-circuit power of 110-kV upstream power grid: 200 MVA

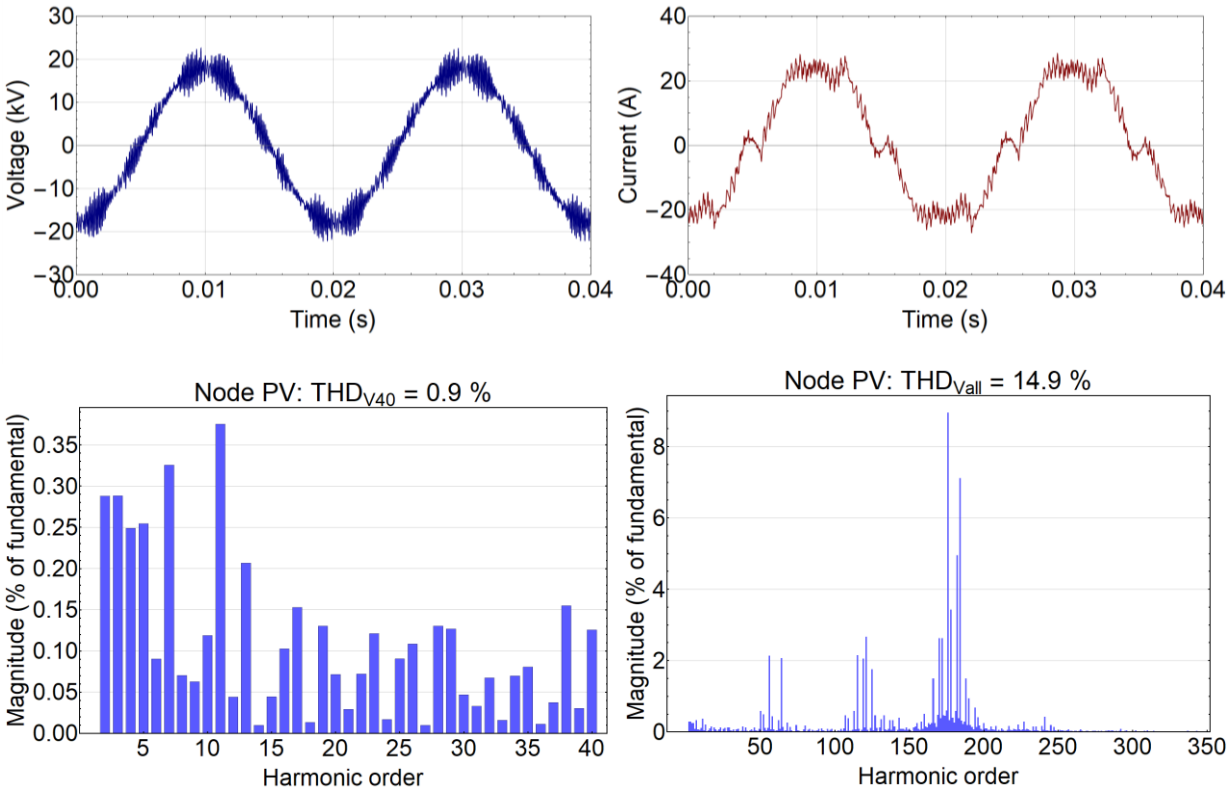

Cable line: 20 m; overhead line: 10 km; short-circuit power of 110-kV upstream power grid: 1000 MVA

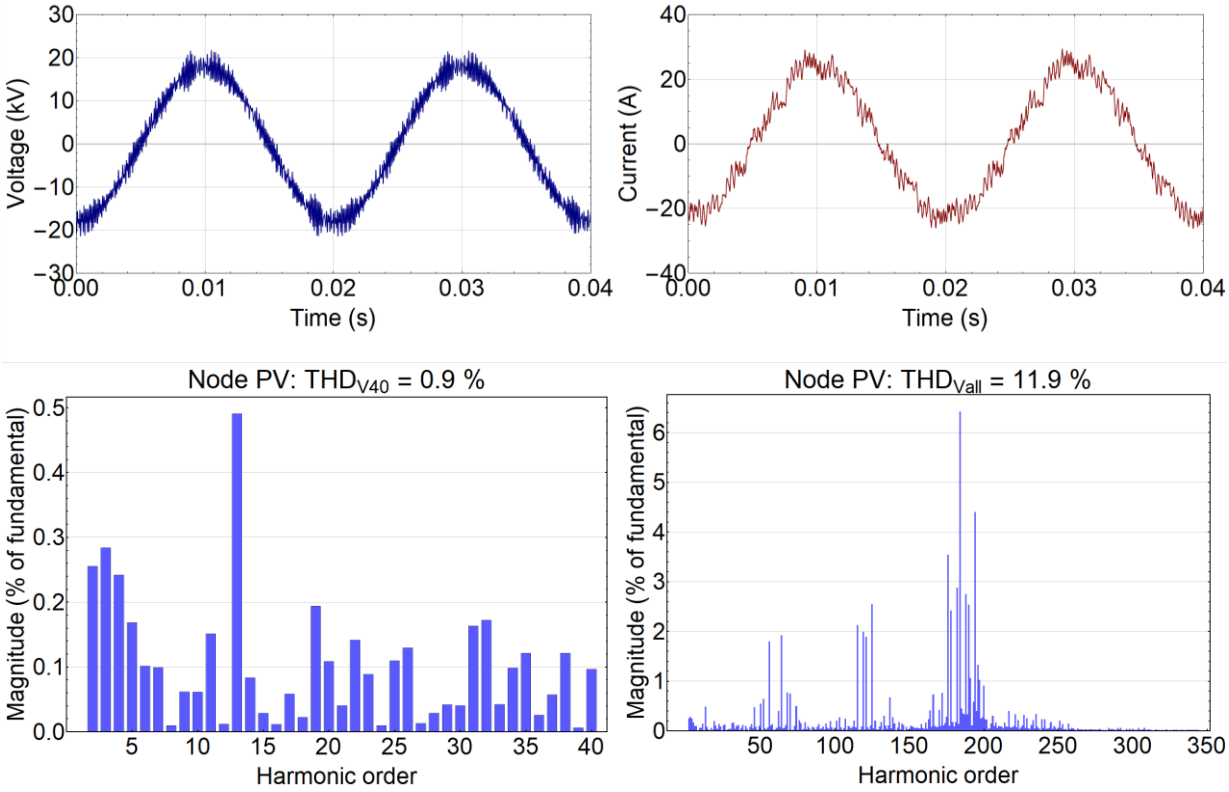

Cable line: 20 m; overhead line: 10 km; short-circuit power of 110-kV upstream power grid: 5000 MVA

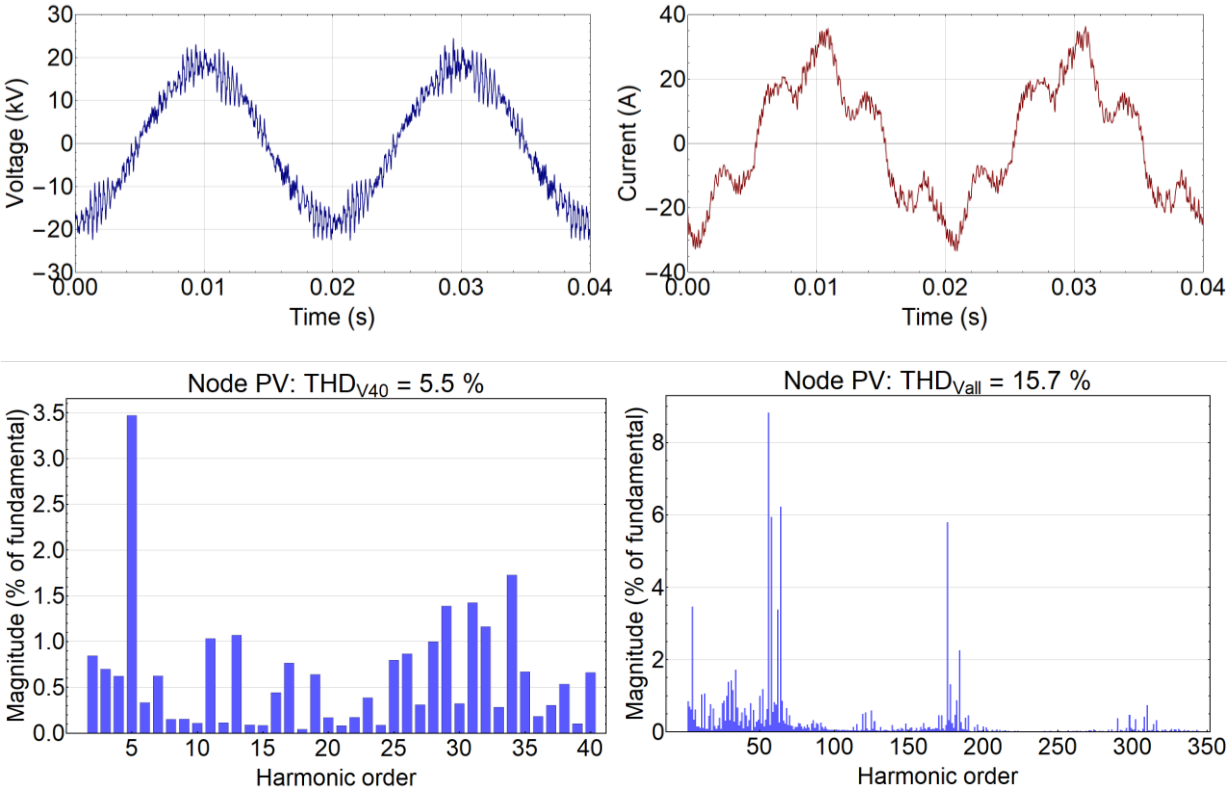

Cable line: 50 m; overhead line: 30 km; short-circuit power of 110-kV upstream power grid: 100 MVA

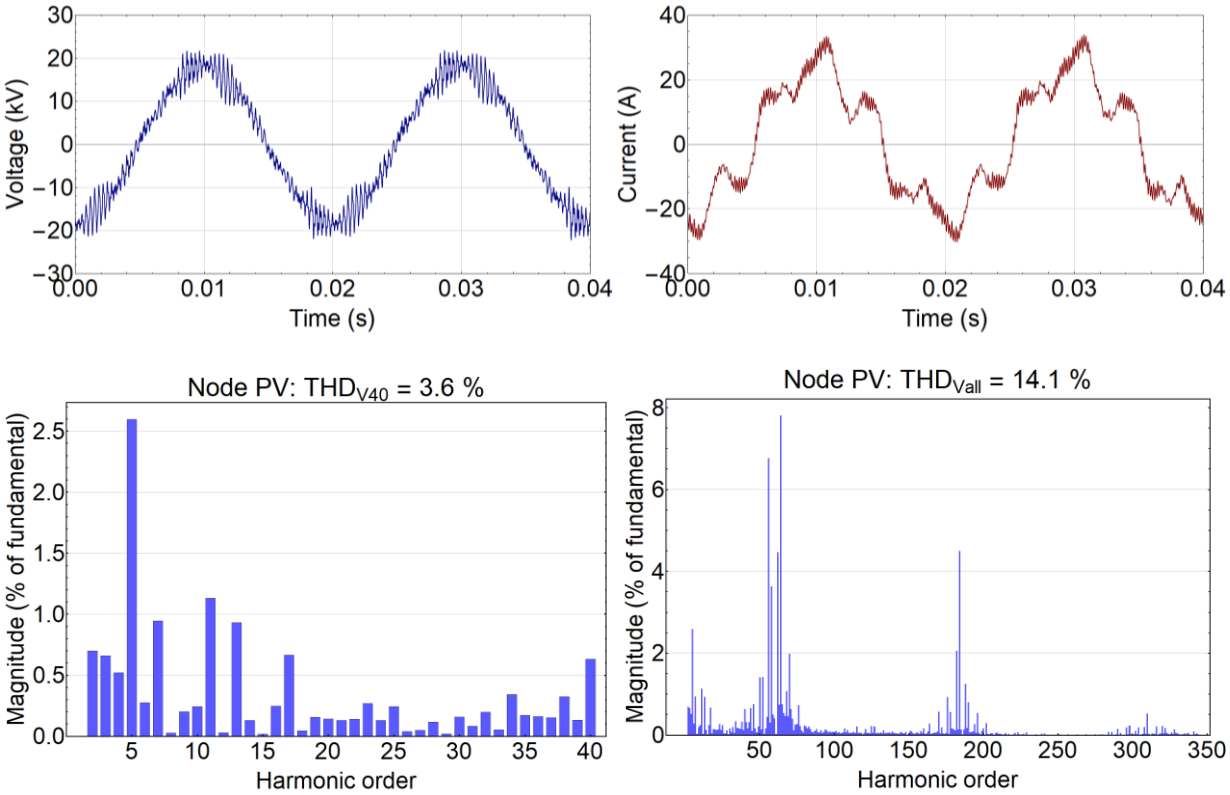

Cable line: 50 m; overhead line: 30 km; short-circuit power of 110-kV upstream power grid: 200 MVA

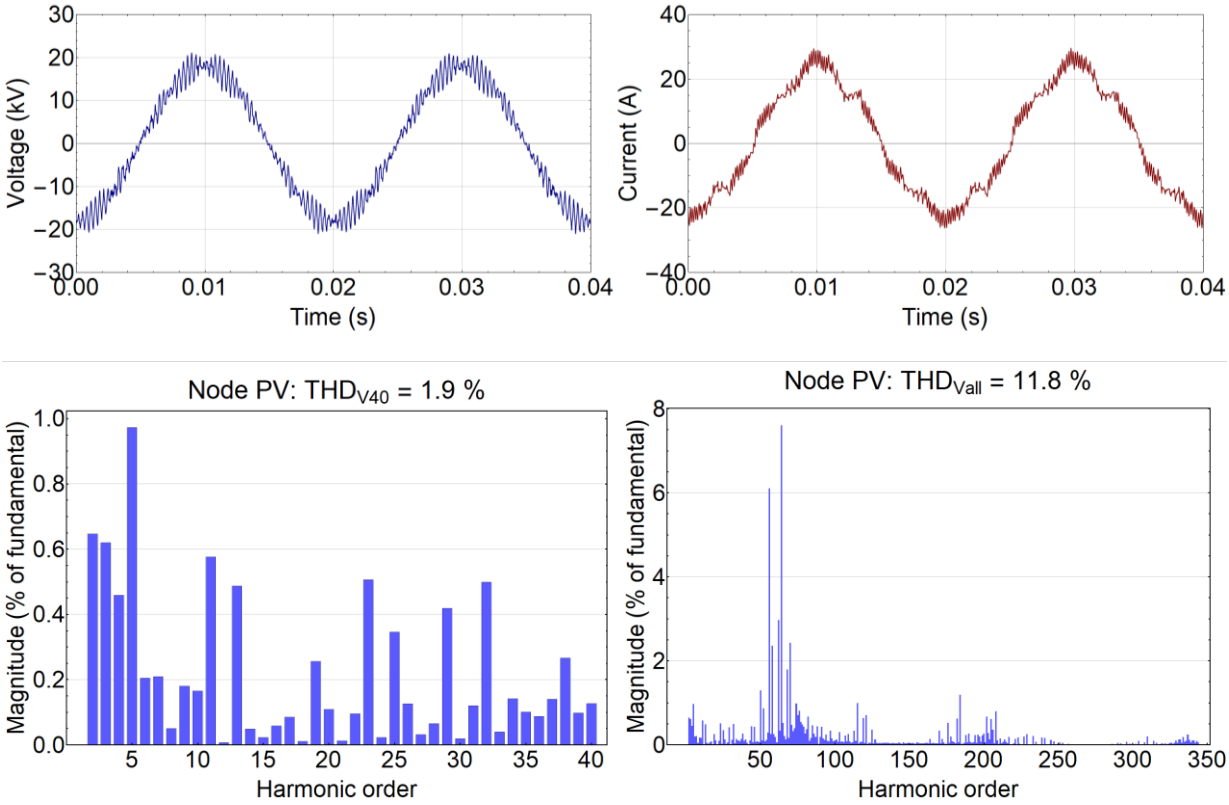

Cable line: 50 m; overhead line: 30 km; short-circuit power of 110-kV upstream power grid: 1000 MVA

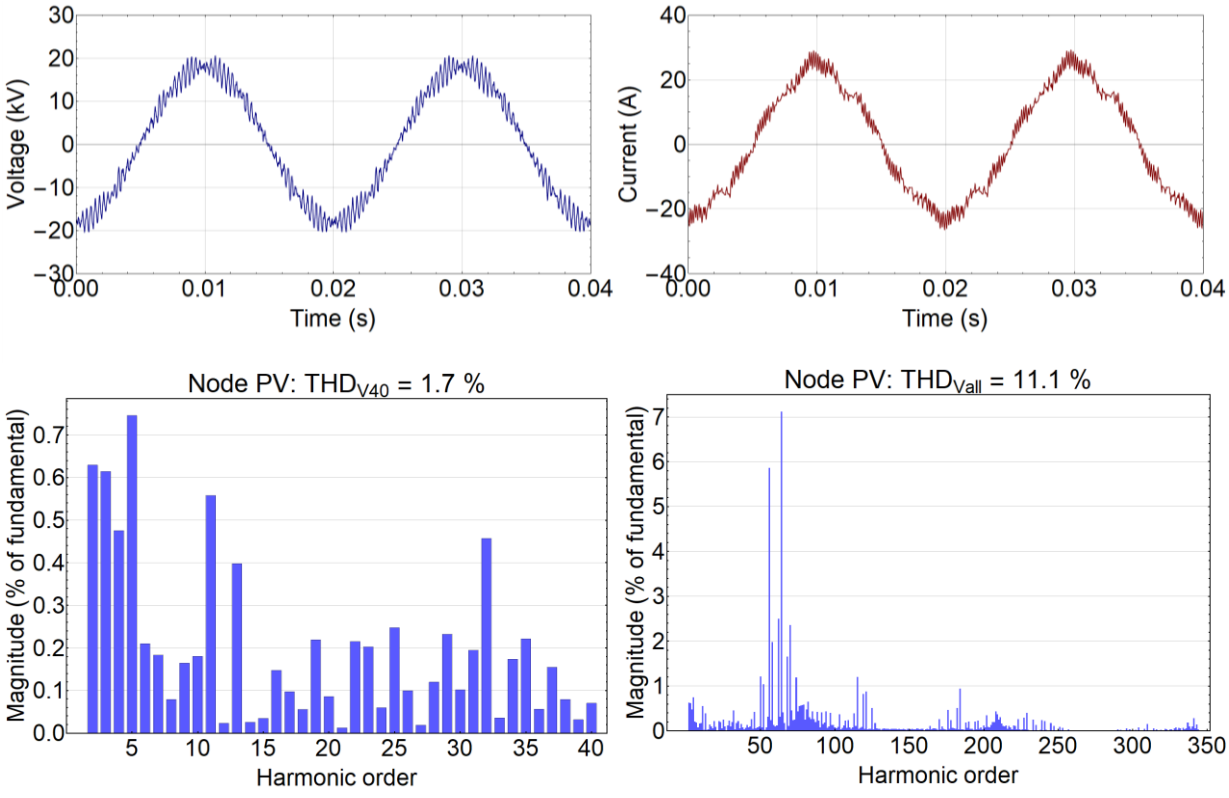

Cable line: 50 m; overhead line: 30 km; short-circuit power of 110-kV upstream power grid: 5000 MVA

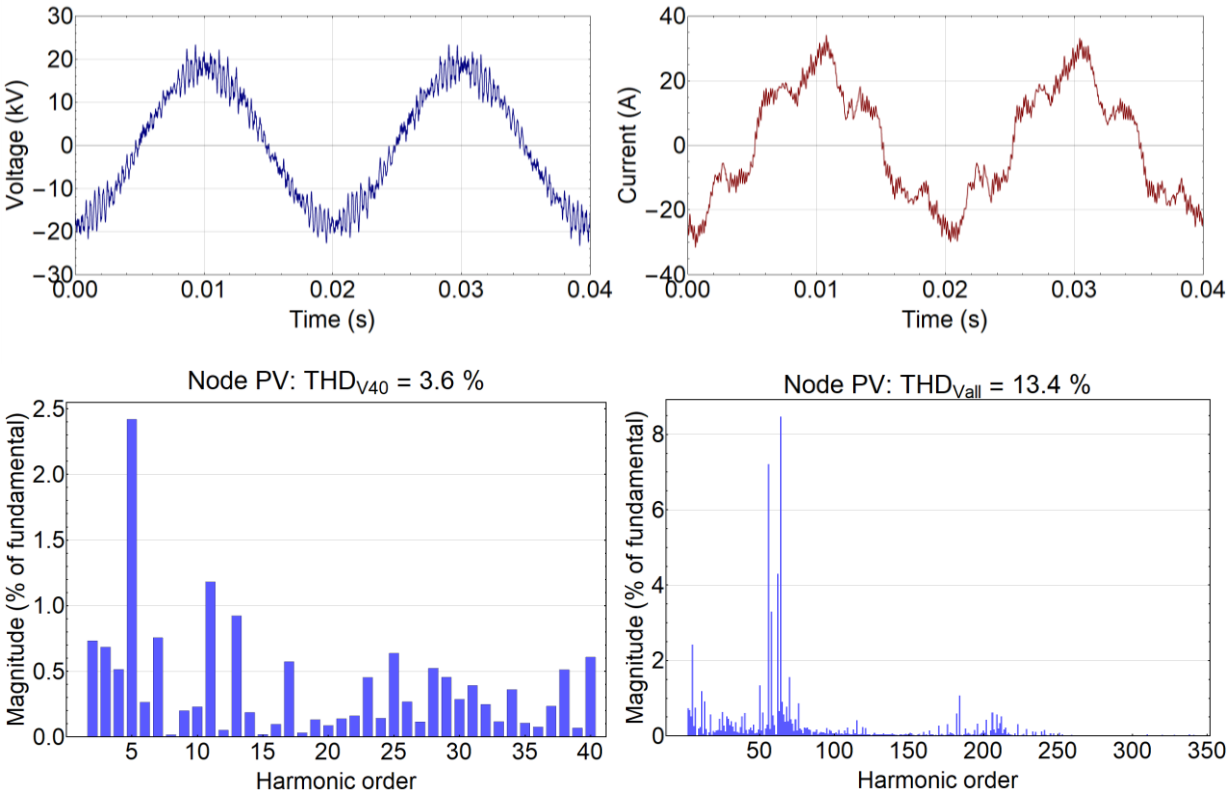

Cable line: 100 m; overhead line: 20 km; short-circuit power of 110-kV upstream power grid: 100 MVA

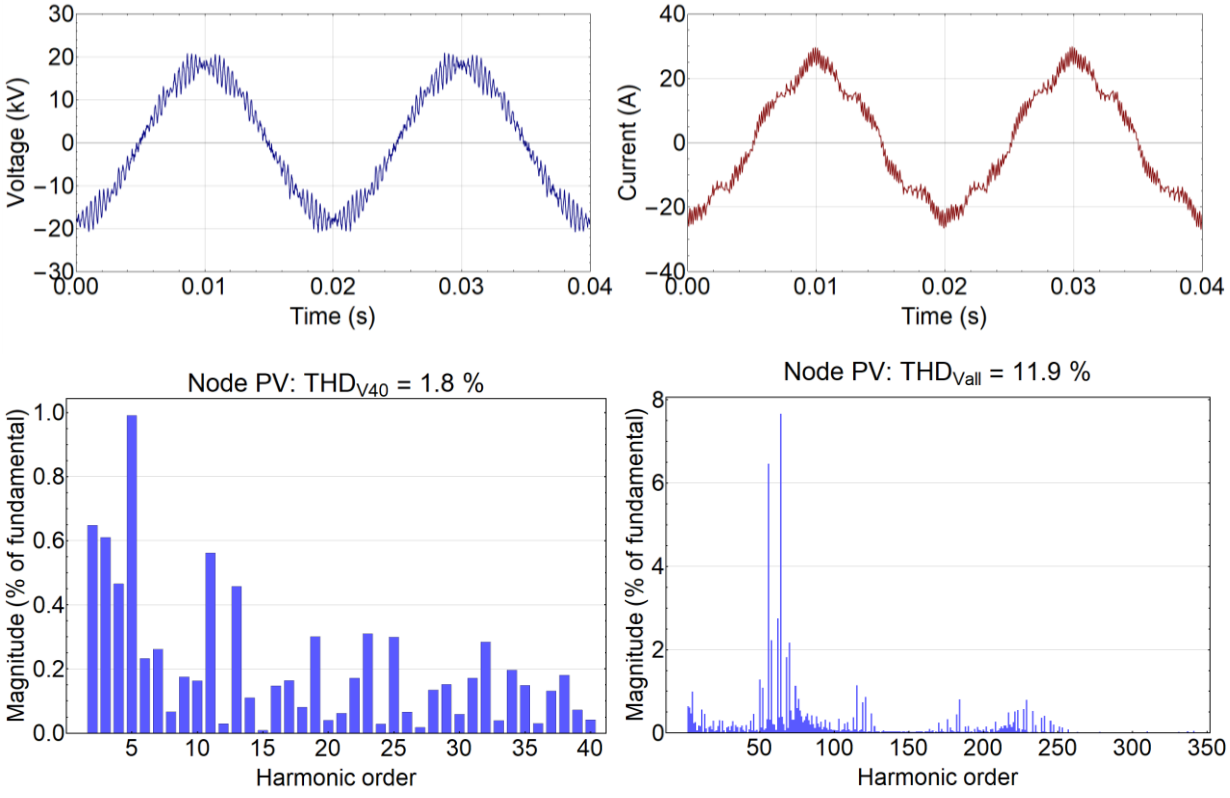

Cable line: 100 m; overhead line: 20 km; short-circuit power of 110-kV upstream power grid: 200 MVA

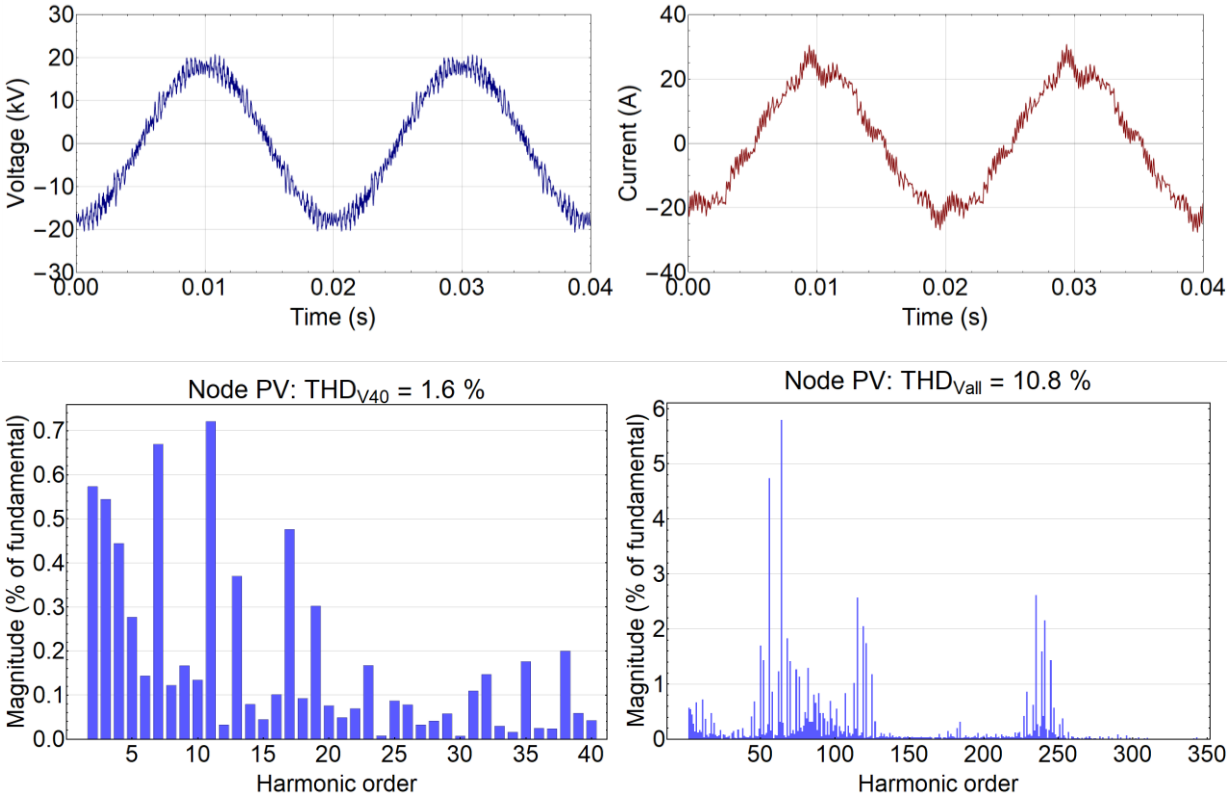

Cable line: 100 m; overhead line: 20 km; short-circuit power of 110-kV upstream power grid: 1000 MVA

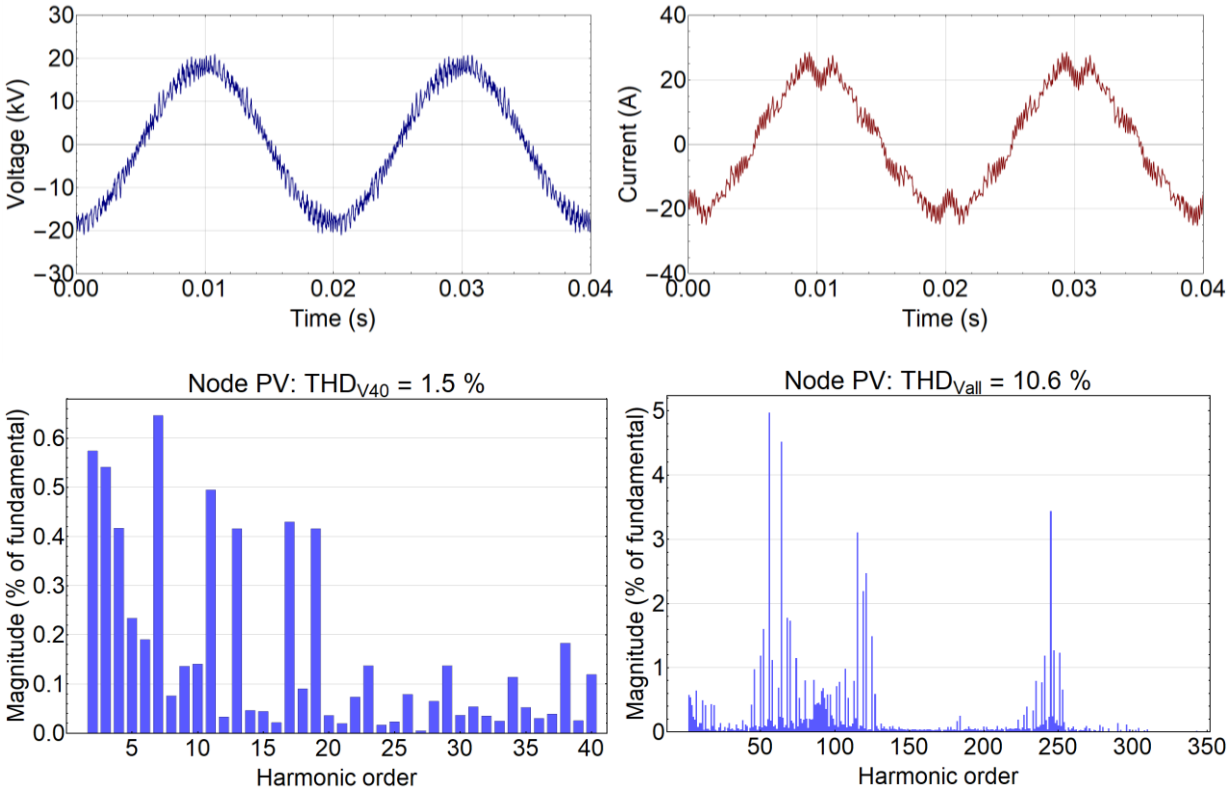

Cable line: 100 m; overhead line: 20 km; short-circuit power of 110-kV upstream power grid: 5000 MVA

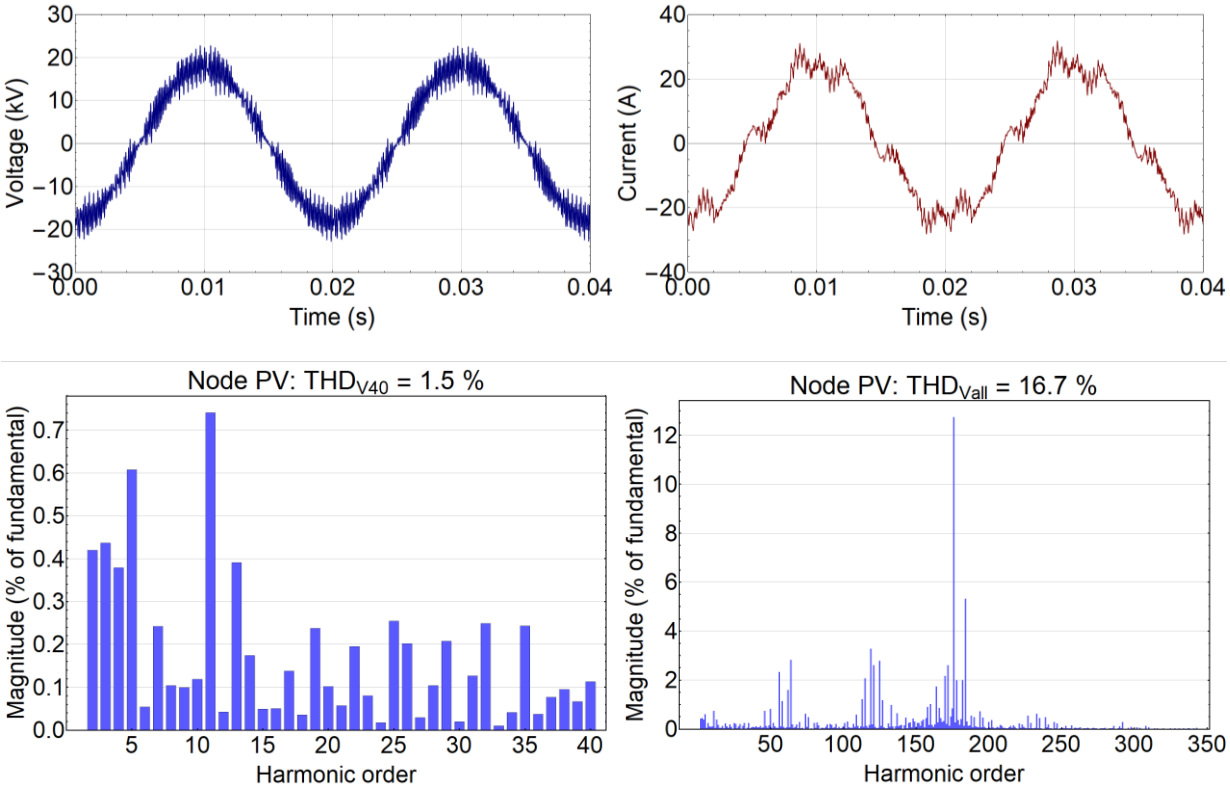

Cable line: 400 m; overhead line: 5 km; short-circuit power of 110-kV upstream power grid: 100 MVA

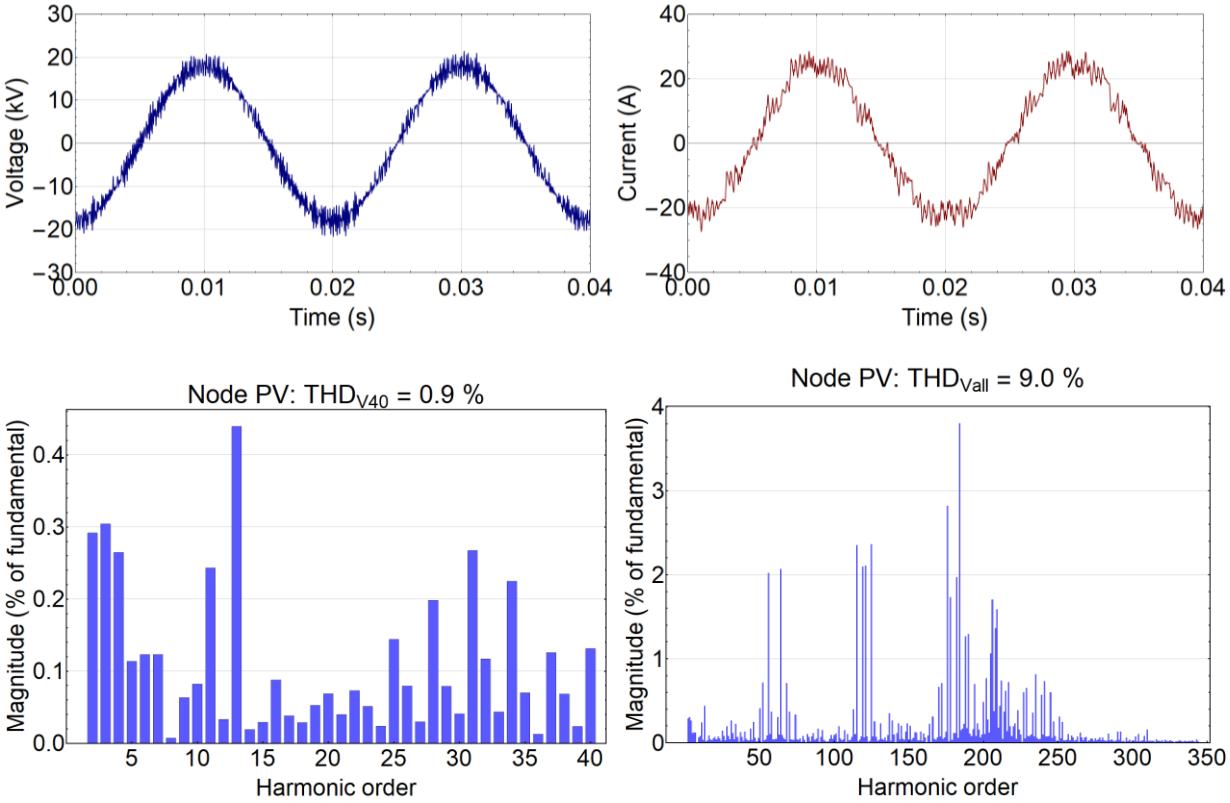

Cable line: 400 m; overhead line: 5 km; short-circuit power of 110-kV upstream power grid: 200 MVA

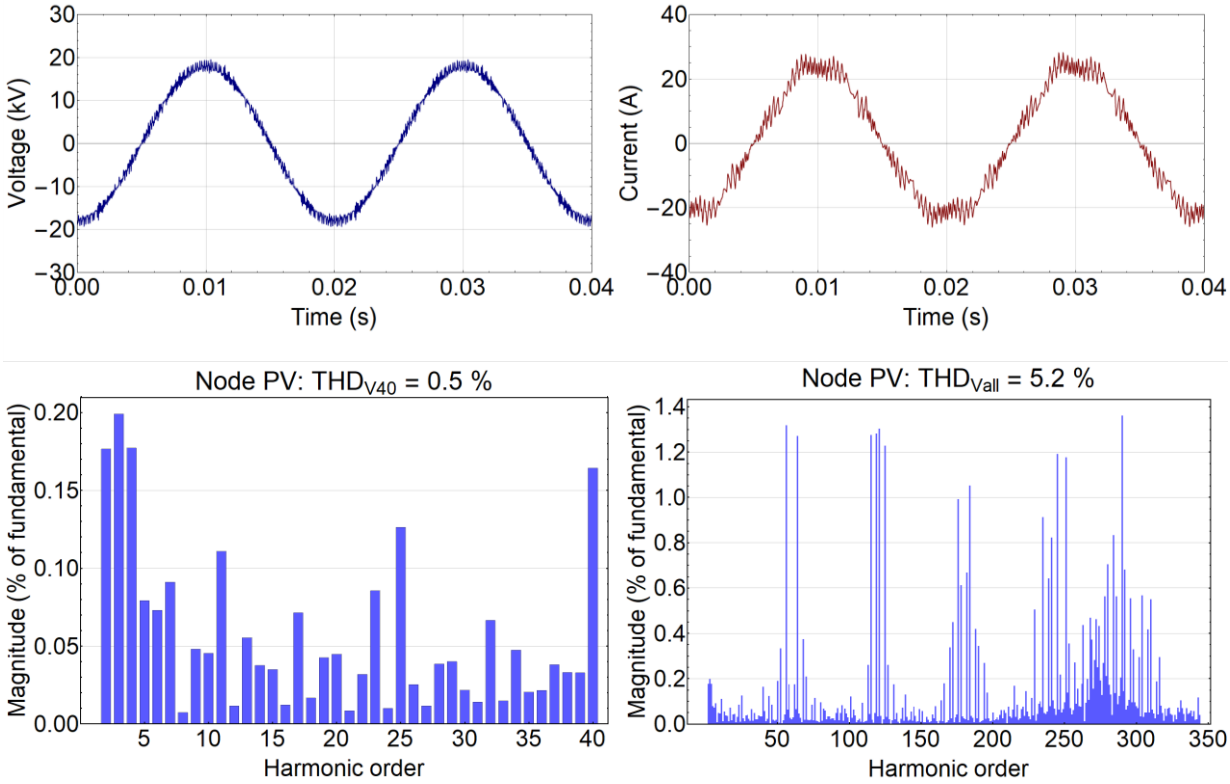

Cable line: 400 m; overhead line: 5 km; short-circuit power of 110-kV upstream power grid: 1000 MVA

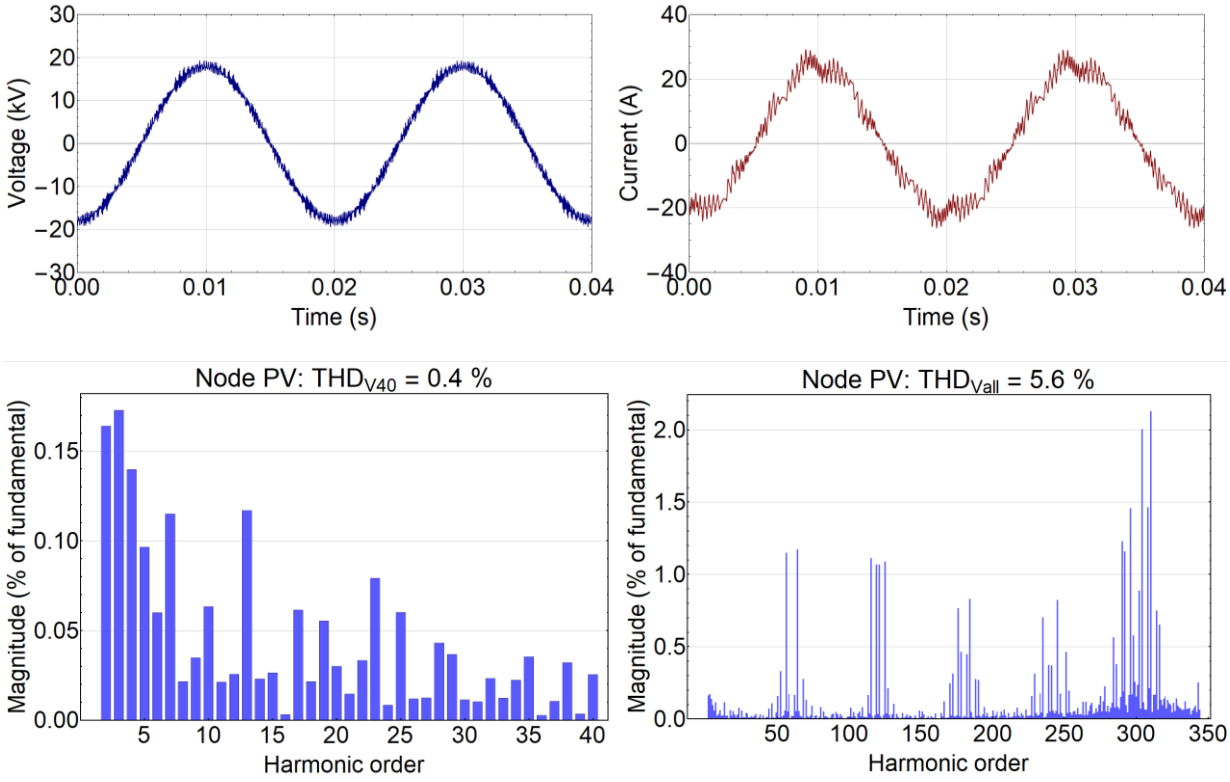

Cable line: 400 m; overhead line: 5 km; short-circuit power of 110-kV upstream power grid: 5000 MVA

Appendix B: Main Components of Test Circuit

B1. Power Frequency Transformer (VT1)

The power frequency voltage transformer was manufactured by BV ELEKTRONIK company. It is a custom-ordered medium voltage test transformer based on a common design with a relatively soft load characteristic. The nominal power is 40 kVA, and the nominal voltage is 400 V/50 kV.

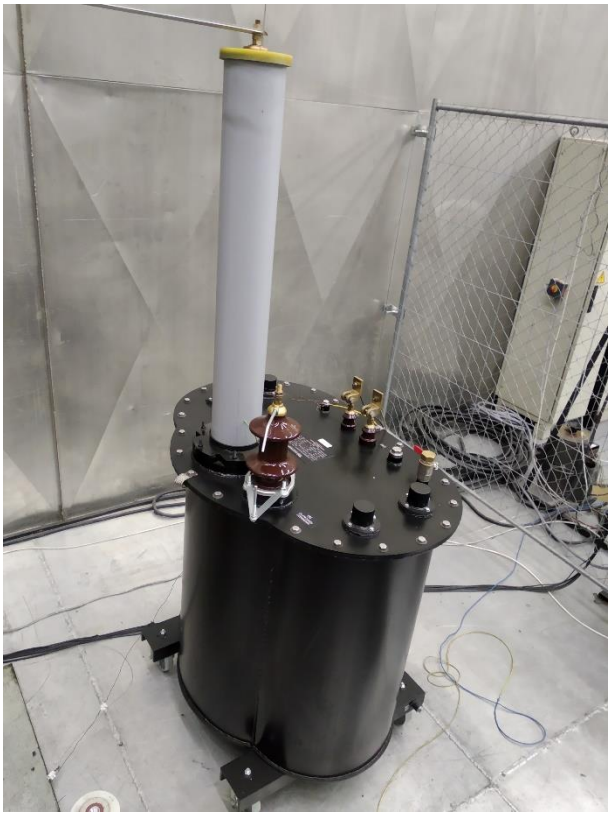

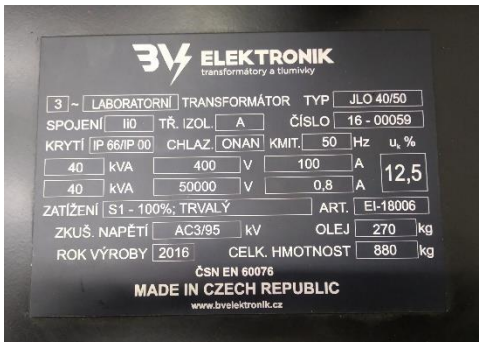

Power frequency voltage transformer BV ELEKTRONIK 50 kVA, 400 V/50 kV

B2. High-Frequency Transformer (VT2)

The high-frequency voltage transformer was manufactured by TRONIC company. The core of the transformer was made of nanocrystalline material to achieve the best possible transmission parameters. The primary winding is supplied with the yellow conductors, and the secondary medium voltage winding is led out by the red conductors. The nominal power is 6 kVA. The output voltage is up to 10 kV at a supply voltage of 120 V. The useful frequency range is from 3 to 100 kHz. The insulation system between primary and secondary windings was designed to withstand a nominal voltage of 60 kV.

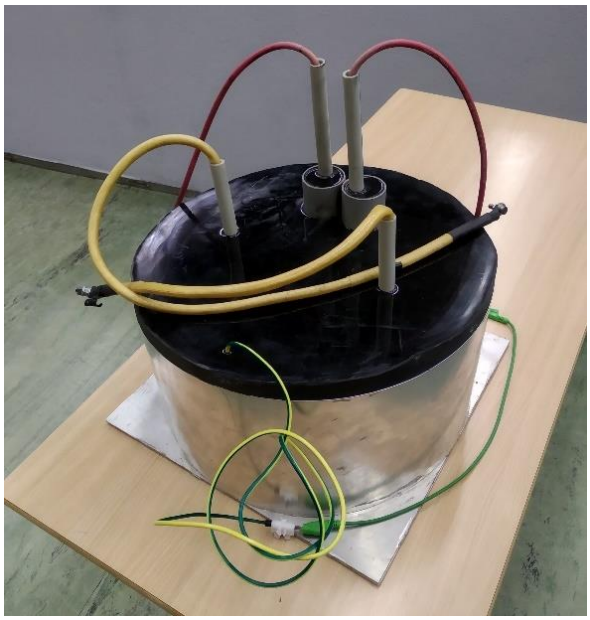

High-frequency voltage transformer TRONIC 6 kVA, 120 V/10 kV

B3. Current Transformer (CT)

The current transformer was manufactured by TRONIC company as well. Two toroidal cores in parallel connection and primary windings are completely sealed in an epoxy-filled enclosure. The secondary winding is formed by a busbar passing through the toroidal transformer. The discharge resistance has been improved by the potential net that is located below the surface of the hole for the secondary winding. The insulation system between primary and secondary windings was designed to withstand a nominal voltage of 60 kV, including superimposed high-frequency components. The nominal power is 10 kVA. Current up to 2 kA is generated to short-circuit of the secondary winding when the primary winding is supplied with a nominal line voltage of 400 V and a current of 25 A.

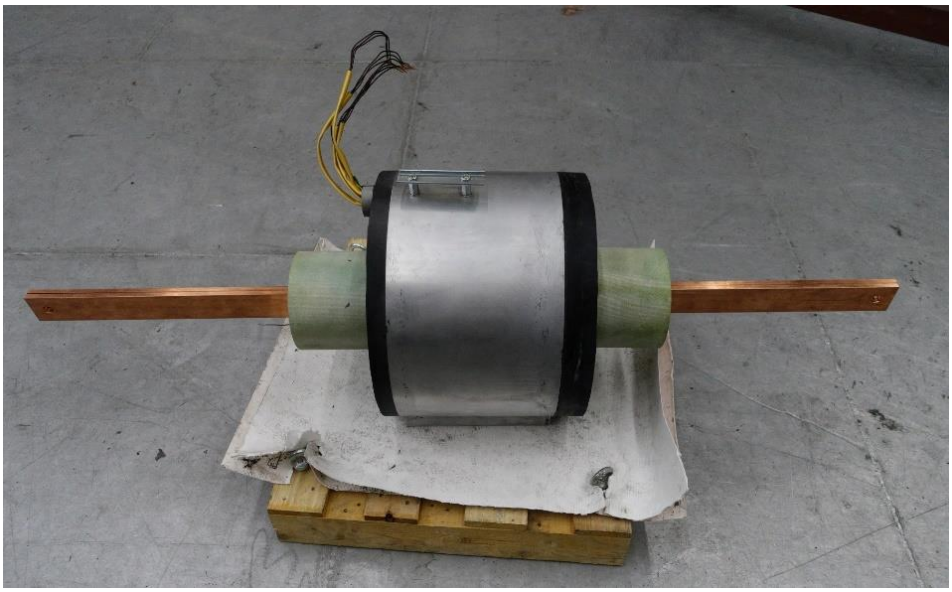

Current transformer TRONIC 10 kVA, 400V, 25 A/2 kA (in short-circuit)

B4. Air-Core Inductor (L)

The last custom-ordered device is an air-core inductor that was manufactured by TRONIC company again. The nominal parameters are a voltage of 15 kV, current of 1 A, and inductance of 11.7 H. The inductor has two additional taps at inductance of 8.6 and 10.2 H (maximal voltage is reduced proportionally).

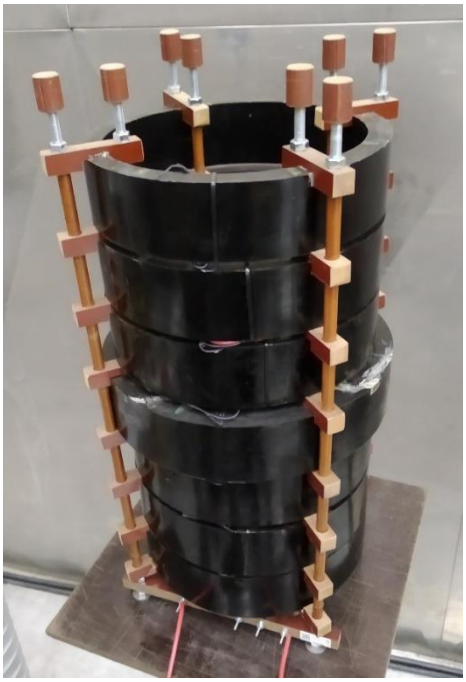

Air-core inductor TRONIC 11.7 H, 15 kV, 1 A

B5. High Voltage Capacitor (C1)

The high voltage capacitor was connected in parallel connection with the power frequency transformer. The available older type of capacitor ZEZ 10 nF, 150 kV was used.

High voltage capacitor ZEZ 10 nF, 150 kV

B6. Medium Voltage Capacitor (C2)

The medium voltage capacitor was connected in serial connection with the high-frequency transformer. The available older type of capacitor Tesla 0.05 µF, 12/25 kV was used.

Medium voltage capacitor TESLA 0.05 µF, 12/25 kV

Appendix C: Circuit Diagrams

C1. Shunts for Measurements of Leakage Currents (0.5 A/19.7 Ω)

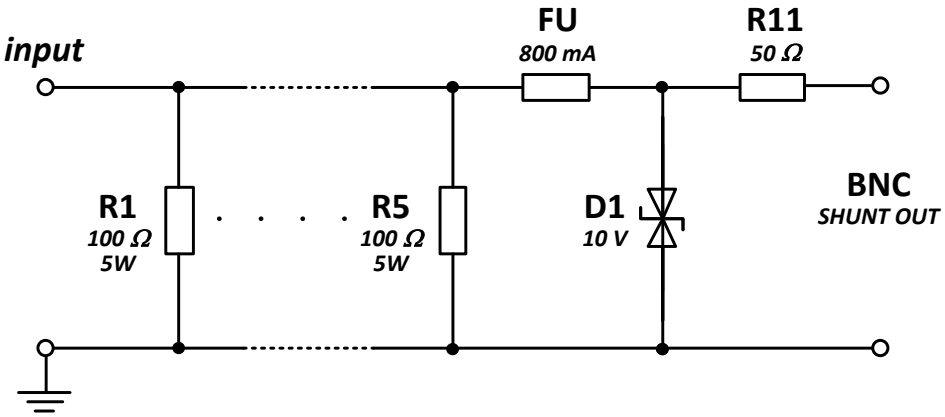

C2. Temperature sensors

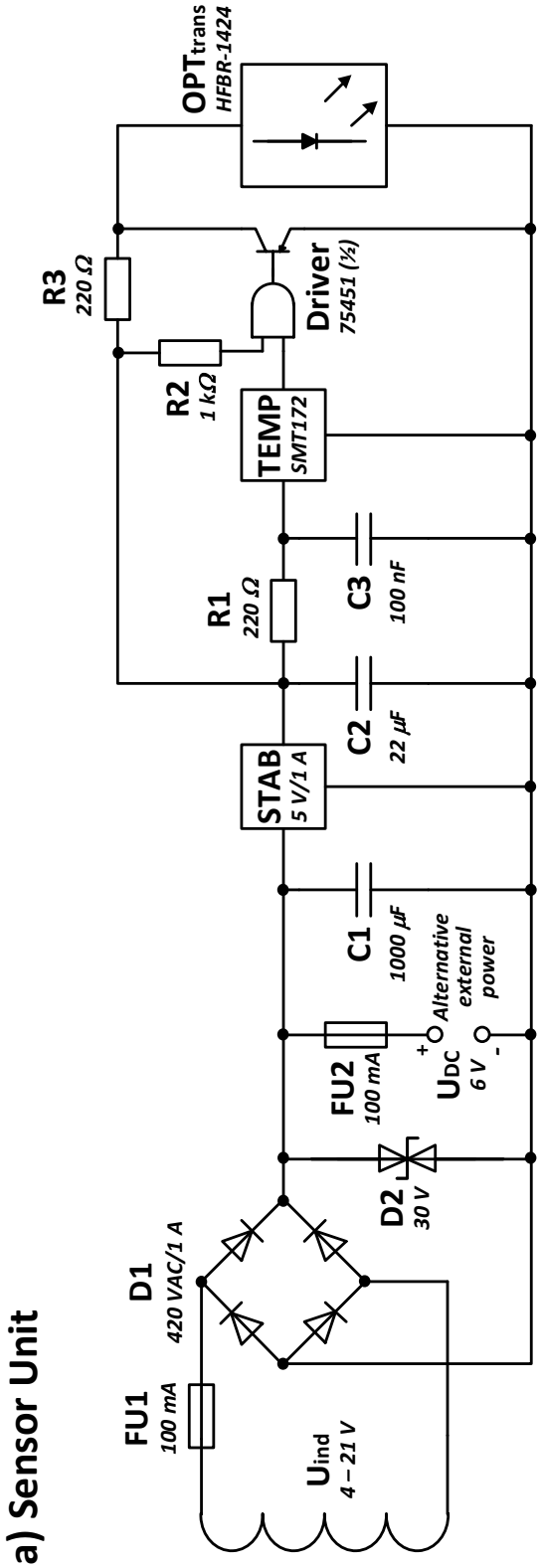

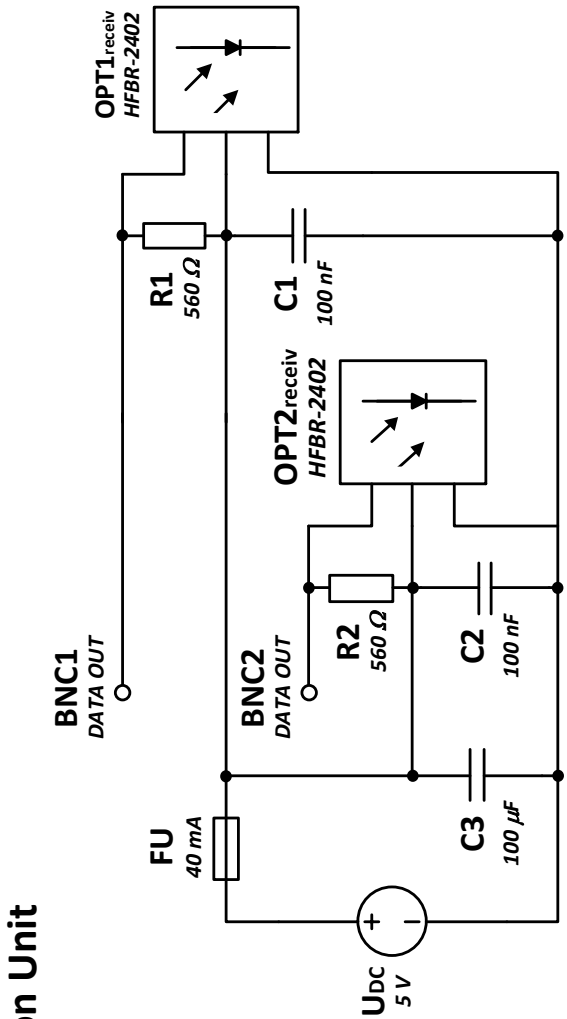

C3. Switchboard for Power Supply of Test Site for Combined Stresses of Medium Voltage Insulation Systems